UNIVERSITY OF CALIFORNIA, SAN DIEGO

Microfluidic Methods: Novel Systems for Observing Model Organisms in Spatial and Temporal Gradients of Chemical Concentration

A dissertation submitted in partial satisfaction of the
requirements for the degree
Doctor of Philosophy

in

Physics (Biophysics)

by

Michael J. Erickstad

Committee in charge:

Professor Alex Groisman, Chair
Professor William F. Loomis
Professor Oleg G. Shpyrko
Professor Douglas E. Smith
Professor Dariusz Stramski

2014

The Dissertation of Michael J. Erickstad is approved, and it is acceptable in quality and form for publication on microfilm and electronically:

_____

_____

_____

_____

_____

Chair

University of California, San Diego

2014

DEDICATION

This dissertation is dedicated to my family (by blood or otherwise). Thanks for putting up with all of the madness.

Skål!

EPIGRAPH

"One of the most moral acts is to create a space in which life can move forward."

- Robert M. Pirsig

TABLE OF CONTENTS

LIST OF FIGURES

LIST OF TABLES

ACKNOWLEDGEMENTS

It has been to my fortune to cross scientific paths with the likes of such titans as Dr. Priya Banerjee and Dr. Yann Gambin. Learning by witnessing their examples has added significantly to my perspectives on science.

Professor Bill Loomis has been very kind in offering me encouragement and advice in the graduate school process. This encouragement has had a long lasting and extremely beneficial effect.

Dr. Laura Hale has been an excellent collaborator. Her scientific insights on zebrafish were essential. As was her fortitude in the face of adversity.

It has been a true honor to collaborate with Dr. Monica Skoge. Furthermore, it is a joy to collaborate with anyone as energetic, hard working, and thoughtful as Monica. I should also note that she is one of the most (if not the very most) professional microfluidics users I have ever encountered.

Within the lab, Loic Tadrist a summer student from France first introduced me to microfluidic methods. For that, I thank him. Dr. Edgar Gutierrez, has clarified details on an astounding number of methods used in the lab. I am ashamed to think about the shear number of times the words “Hey Edgar can I bug you?” have come out of my mouth, but I am

truly grateful for they way he always has responded so kindly. I enjoyed working with Dr. Micha Adler. Our discussions and collaboration on experimental and statistical methods were illuminating and advanced my research. I initially worked closely with Dr. Mark Polinkovsky. It has been a major benefit and pleasure to learn from him. His cool confidence and "just try it" attitude really helped to break me out of the rut caused by fear of trying things.

Of course, Professor Alex Groisman has taught me a great deal about experimental science. This includes not just how experimental science is conducted, but also how it should be perceived and approached. I am only beginning to comprehend the brilliance by which he can combine physical phenomena to devise novel experimental apparatuses. Witnessing his perpetual eye on the scientific horizon has made me think very seriously about how much work it takes to be a successful PI.

I place my hopes for the future honor of the lab in Ward Ronan IV and Alex Yang. They are growing stars each with there own scientific strong suits.

I must also thank my family and friends for beings so supportive. I thank my mother and sisters for being steadfast in their encouragement over the years. I thank my father for teaching me how machines work at a young age and getting me interested in science and engineering. My classmates have also had a major positive influence on my outlook and

skills. In particular, I have learned a great deal during time spent with Dr. Alex Mendez.

Chapter 2.1, in full, has been submitted for publication as "A low-cost low-maintenance ultraviolet lithography light source based on light-emitting diodes", Erickstad, Michael; Gutierrez, Edgar; and Groisman, Alex. The dissertation author is first author and a leading contributor to this paper.

Chapter 2.2, in full, has been submitted for publication as "The supplementary information to: A low-cost low-maintenance ultraviolet lithography light source based on light-emitting diodes", Erickstad, Michael; Gutierrez, Edgar; and Groisman, Alex. The dissertation author is first author and a leading contributor to this paper.

Chapter 3, in full, is in preparation for submission for publication as "A microfluidic system for studying the behavior of zebrafish under Acute Hypoxia", Erickstad, Michael; Hale, Laura A.; Chalasani, Sreekanth H.; Groisman, Alex. The dissertation author is a co-first author and a leading contributor to this paper.

Chapter 4, in full, includes information and materials from the paper submitted for publication as "Cellular memory in eukaryotic chemotaxis", Skoge, Monica; Yue, Haicen; Erickstad, Michael; Bae, Albert;

Levine, Herbert; Groisman, Alex; Loomis, William F.; Rappel, Wouter-Jan. The dissertation author is a coauthor and a leading contributor to the microfluidics aspects of this paper.

VITA

2008	Bachelor of Science, University of Minnesota, Twin Cities, Institute of Technology
2008 - 2009	Graduate Teaching Assistant, Physics Department, University of California, San Diego
2009	Master of Science in Physics, University of California, San Diego
2009 - 2014	Graduate Research Assistant, Physics Department, University of California, San Diego
2013	Candidate of Philosophy in Physics, University of California, San Diego
2014	Doctor of Philosophy in Physics (Biophysics), University of California, San Diego

PUBLICATIONS

M. Adler, M. Erickstad, E. Gutierrez, and A. Groisman, "Studies of bacterial aerotaxis in a microfluidic device", *Lab on a Chip,* 2012, **12**, 4835-4847

ABSTRACT OF THE DISSERTATION

Microfluidic Methods: Novel Systems for Observing Model Organisms in Spatial and Temporal Gradients of Chemical Concentration

by

Michael J. Erickstad

Doctor of Philosophy in Physics (Biophysics)

University of California, San Diego, 2014

Professor Alex Groisman, Chair

The field of microfluidics has been advancing with a great pace since its initial implementation in the 1980's. It has become an immensely useful tool for practitioners across a multitude of disciplines. Here we present novel microfluidic experimental systems designed to enable new measurements in biology.

Chapter 1: Introduction

The term microfluidics refers to the set of concepts and methods for controlling and manipulating small volumes (10^{-9} – 10^{-18} L) of fluids at sub-millimeter length scales[1]. This definition makes microfluidics sound rather arcane and perhaps limited in scope. However, current and potential future applications of microfluidics show that microfluidic systems have immense utility and potential. For a few examples, microfluidic methods have enabled:

-chemists to perform reactions on tiny (fL) volumes of reagents, and thus observe fast processes;

-biologists to study and manipulate isolated cells in well defined micro environments, and thus gain quantitative insights into such phenomena as intercellular variability and various taxes;

-medical personnel to use microfluidic diagnostic assays and thus improve human wellbeing wherever they are effectively applied[2-3];

Furthermore, I must point out that nature itself incorporates a great deal of microfluidics into its structures. Consider your own circulatory system for instance.

Microfluidic methods are the very heart of my work and thus are the heart of this dissertation. To be clear the microfluidic systems discussed here are primarily experimental apparatuses intended to allow new

measurements of biological systems. These microfluidic experimental systems include control and imaging components centered around a microfluidic chip. Microfluidic chips are composed of networks of microscale fluid flow channels of varying shape and size, which connect to standard sized laboratory tubing at ports. These networks can incorporate a variety of features in order to achieve manipulation of the microenvironments within the channels of the chip.

In this chapter, I will introduce the essential physics governing microfluidic systems. Then, I will introduce the methods by which microfluidic systems are fabricated. Finally, I will discuss the operation and characterization of microfluidic systems.

1.1: Microfluidic Theory

1.1.1: Small Length Scale Effects

Henrik Bruus' book *Theoretical Microfluidics* is a wonderful introduction to the relevant physics encountered in microfluidic devices. It has had a large influence on my understanding of microfluidics, and consequently on this chapter. It was inevitable that this chapter would follow a similar line of development as that in his book[4].

We begin by explaining and typifying the types of physical forces and effects that are most relevant to microfluidics. We shall consider which forces and effects become dominant as we go to small (<1000μm) linear

length scales (l). Volume (V) is proportional to the 'cube' of the length. Meanwhile, surface area (S) is proportional to the 'square' of the length. As l goes to zero, the surface to volume ratio ($S/V = 1/l$) goes to infinity. This indicates that as we look at systems of smaller and smaller length scales, forces and effects associated with surface area will gain significance relative to those associated with volume. This is especially important when considering fluid flows and diffusion in microscale environments.

In fluid flows, forces exerted by pressure gradients and drag scale with area, meanwhile mass and consequently momentum and gravitational force scale with volume. At microfluidic scales, pressure gradients and drag often dominate the momentum in the system. For example, if an *E. coli* cell is swimming along and then stops whipping its flagella, it will stop within an atomic length[5], because it has so little momentum relative to the drag forces exerted by the surrounding fluid.

In diffusion, particles thermally bounce and wander out from their initial position at random. Consider a basic diffusion problem in which a tank is divided into two halves, left and right, by a removable wall. Let the tank be cubic with edge length l. The tank is filled with water evenly on both sides, but the right side additionally has some food coloring or dye mixed in. When we remove the divider, the dye particles begin to wander out of the right side of the tank. Eventually, the dye will distribute evenly throughout the whole tank. We want to get some idea of how the

characteristic time of diffusion scales with l, i.e. how long the diffusion process takes as a function of l.

Picture an imaginary boundary in the middle of the tank where the divider used to be. At any instant, the total number of particles diffusing across this imaginary boundary scales with the cross sectional area of the tank. It also scales with the gradient of the concentration, which is inversely proportional to the length. In the end, half of the particles will be on one side of the tank and half will be on the other, and both sides will have half of the concentration of particles that the right side of the tank initially had. Given a set initial concentration on the right side of the tank, the total number of particles that need to diffuse across the tank is proportional to the volume of the tank. We can get a simple notion of the scaling of the diffusion time by taking the ratio of the number of particles to diffuse divided by the rate at which they cross the tank. Therefore, the diffusion time is proportional to l^2. If the tank is half the size, the diffusion takes a quarter of the time.

Particles are not the only things that diffuse. Heat and momentum also diffuse. In microfluidics systems, all three diffuse much more quickly than what we observer at macroscopic length scales in daily life. Let us move on before your attention diffuses.

1.1.2: Flow in Microfluidic Channels

We wish to gain a quantitative understanding of flows in microfluidic channels. Our first objective is to get expressions describing the velocity field of the flow in channels with given boundary conditions.

The Navier-Stokes equation for fluid flow

$$\rho\,[\partial_t \vec{v} + (\vec{v}\cdot\vec{\nabla})\vec{v}] = -\vec{\nabla}p + \mu\nabla^2\vec{v} \tag{1-1}$$

where $\vec{v} = \vec{v}(x, y, z, t)$ is the fluid velocity vector field, ρ is the density of the fluid, and μ is the dynamic viscosity of the fluid; arises naturally from considerations of shear forces and conservation of particle number and momentum. We can reorganize it in a unitless form as

$$\mathrm{Re}\,[\hat{\partial}_t \hat{\vec{v}} + (\hat{\vec{v}}\cdot\hat{\vec{\nabla}})\hat{\vec{v}}] = -\hat{\vec{\nabla}}\,\hat{p} + \hat{\nabla}^2\hat{\vec{v}} \tag{1-2}$$

The Reynolds number is defined as

$$\mathrm{Re} \equiv \frac{\rho\, v_0\, L_0}{\mu} \tag{1-3}$$

where v_0 is a characteristic velocity in the flow (typically the maximum velocity) and L_0 is a characteristic length scale in the flow (typically the length over which the flow velocity varies). The Reynolds number is unitless and makes a comparison between momentum effects (which scale with volume) and viscous drag (which scales with area).

In microfluidics systems, the Reynolds number is usually quite small (Re << 1). In such cases the N-S equation reduces to the Stokes equation

$$-\vec{\nabla}p + \mu \nabla^2 \vec{v} = 0 \tag{1-4}$$

Which, unlike the N-S equation, is a linear differential equation, and, thus, more manageable.

Meanwhile, for many liquids we can consider the fluid to be incompressible as defined by $\nabla \cdot \vec{v} = 0$.

With the conditions of low Reynolds number and incompressibility, we can calculate velocity fields for flows in many basic microfluidic channel shapes computationally, or by analytic solution.

Flow between Parallel Plates

Next, we apply these basic equations to solving flow between parallel plates. The flow velocity field between two parallel plates is arguably the simplest flow field relevant to microfluidics. An understanding of the flow between two parallel plates will lend intuition to the calculation and interpretation of flow fields in more complicated channel geometries.

Consider two parallel plates, one in the x-y plane and one a distance h above the x-y plane, with liquid between them. Let the pressure field be

defined at a constant value in the plane $x = 0$ and some other constant value in the plane $x = L$. In this case, the pressure varies as a function of x only, and the velocity vector field only has components in the x direction. We can write the Stokes equation in the very manageable form

$$\mu[\partial_y^2 + \partial_z^2]v_x(y,z) = \partial_x p(x) \tag{1-5}$$

by considering the symmetry introduced by the plates lying parallel and the fluid being incompressible, we realize that the pressure varies linearly. With this, we can rewrite the Stokes equation as

$$[\partial_y^2 + \partial_z^2]v_x(y,z) = -\frac{\Delta p}{\mu L} \tag{1-6}$$

where $\Delta p \equiv p(x=0) - p(x=L)$. By considering the plates to be infinite in their expanse or at least infinite by comparison to the other relevant length scale h, we gain symmetry in the y direction. This y direction translational symmetry further simplifies the Stokes equation to

$$\partial_z^2 v_x(z) = -\frac{\Delta p}{\mu L} \tag{1-7}$$

because the fluid velocity field is no longer a function of y. This second-order differential equation can be solved by direct integration. We integrate twice and acquire the solution

$$v_x(z) = -\frac{\Delta p}{\mu L}\frac{z^2}{2} + az + b \tag{1-8}$$

where a and b are arbitrary coefficients of integration. To eliminate the arbitrary coefficients we assume "no slip boundary conditions". For flow between two parallel plates the assumption of "no slip boundary conditions" is the assumption that the infinitesimally thick layer of liquid directly in contact with each plate is not moving, i.e. $v_x(z=0)=0$ and $v_x(z=h)=0$. Finally, a little algebra yields the solution for the velocity field between two parallel plates

$$v_x(z)=\frac{\Delta p}{L}\frac{z(h-z)}{2} \tag{1-9}$$

We refer to this as parabolic flow for obvious reasons. We can take the z integral of the velocity field to get the volumetric flow per width in the y direction

$$q=\frac{\Delta p}{L}\frac{h^3}{12} \tag{1-10}$$

The volumetric flow through a given width w is

$$Q=qw=\frac{\Delta p}{L}\frac{wh^3}{12} \tag{1-11}$$

Dividing by w and h gives the mean flow velocity (v_{avg})

$$v_{avg}=\frac{Q}{wh}=\frac{\Delta p}{L}\frac{h^2}{12} \tag{1-12}$$

Despite the assumption of y translational symmetry, these results are highly applicable to many microfluidic channels, specifically those with a

high aspect ratio. We will see the validity of approximating the flow in channels with high aspect ratios by the flow between parallel plates in the next section.

Flow in a Channel with a Rectangular Cross Section

In a rectangular channel, the situation is similar to that for parallel plates, but differs in that there are two additional walls, each parallel to the z-x plane, located at distances $\frac{w}{2}$, and $-\frac{w}{2}$ from the z-x plane where $w \geq h$. These additional walls destroy the Y direction translational symmetry that we used for parallel plate flow. We can follow our previous developments up to equation 1-6. Noting that there are two additional "no slip boundary conditions" one at each of the additional walls, this partial differential equation has the Fourier series solution

$$v_x(y,z) = \frac{4h^2 \Delta p}{\mu L} \sum_{n,odd}^{\infty} \frac{1}{n^3} \left[1 - \frac{\cosh(n\pi \frac{y}{h})}{\cosh(n\pi \frac{w}{2h})} \right] \sin(n\pi \frac{z}{h}) \qquad (1\text{-}13)$$

as before we can integrate in z and y and produce an approximation for the volumetric flow rate

$$Q \approx \frac{h^3 w \Delta p}{12 \mu L} \sim \qquad (1\text{-}14)$$

where $\sim = \left[1 - 0.630\frac{h}{w}\right]$. For high aspect ratios, $\sim$ approaches 1, making the flow rate approach the that for parallel plates.

Noting that the flow rate depends linearly on the pressure difference, we can group terms into a sort of Ohm's Law analogy for hydrodynamic resistances.

$$R_f = \frac{\Delta p}{Q} = \frac{12\mu L}{h^3 w \sim} \tag{1-15}$$

where R_f is the hydrodynamic resistance of the channel. Indeed, networks of channels can be treated in the same fashion as networks of resistors. Therefore, we can utilize old familiar rules like the addition of resistors in parallel or Thevenin's Equivalent Resistance Theorem. One important thing to keep in mind however is that different flows within a chip might carry different concentrations or types of solute particles. As such, not all microfluidic currents are composed of the interchangeable identical constituent particles as is the case with electrical currents (never minding spin).

1.1.3: Diffusion

Diffusion is one of the most important processes that takes place in microfluidic and biological systems. The importance of diffusion in biological systems is like that of gravity in mechanical systems. It is gently

at work everywhere, and completely taken for granted. Diffusion is the essential process at work in the gas exchangers described in chapter 3 and the formation of the chemoattractant waves described in chapter 4.

Diffusion is the process by which particles of a given type or species tend to distribute evenly over space by random thermal motion. Diffusion processes are closely related to the simplified concept of the random walk. In a random walk a particle (or dot or person) moves repeatedly according to a set of statistical rules and its (or their) position changes in time. (An excellent source of information about random walks is *"Random Walks in Biology"* by Howard C Berg.)[5] The simplest form of random walk (sometimes called the drunkard's walk) is a random walk in which our particle moves a set distance (sometimes referred to as a step) either in the positive or negative direction, chosen at random, every round, along a one-dimensional number line (for instance the x-axis) in a series of rounds. We can simulate random walks using a random number generator such as a coin (in the case of 50/50) or a dice or the random number generator of a computer. We can also incorporate more dimensions into our model, allowing the walkers to move on multiple axes (i.e. adding the y and z axes). If we simulate a large number of random walks simultaneously, we see that the random walkers tend to become more spread out over space with each successive round of steps. This is the process of diffusion.

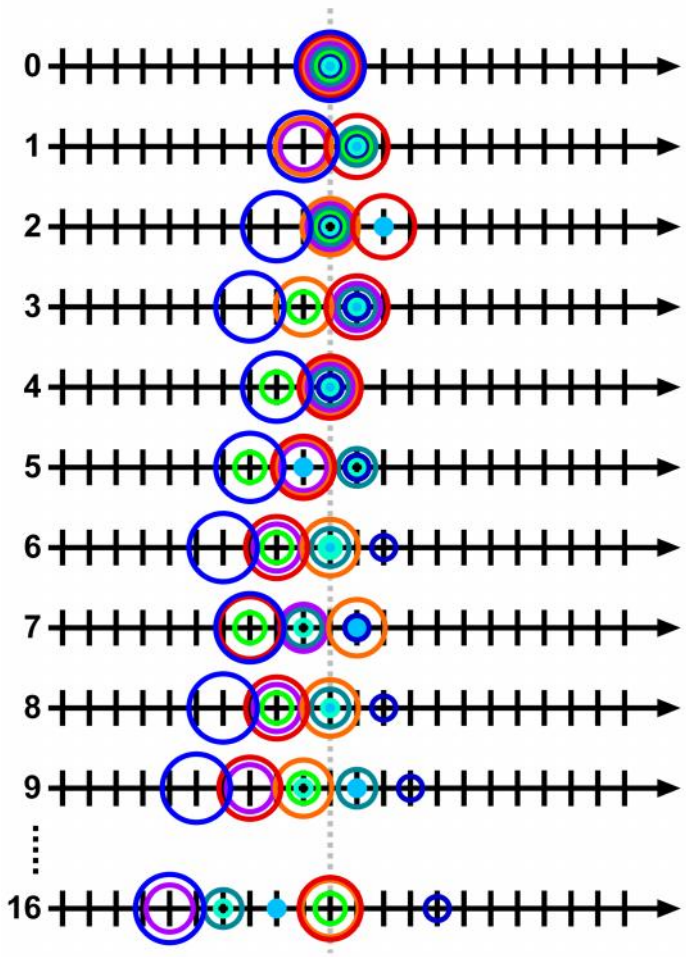

Figure 1-1: Nine random walks. Successive times are shown from top to bottom. Note that the root mean square displacement of the 9 walkers at the end of 16 steps is $((2\circ 0^2+1\circ 2^2+3\circ 4^2+2\circ 6^2)/9)^{1/2} \approx 3.7$ where theory predicts 4.

Another simple way of picturing the diffusion of dissolved species is to compartmentalize the particles into infinitesimal bins in space and assume that each of the particles move into the adjacent bins with equal probability in all directions. (This is a deterministic view of diffusion but it works well in the context of dissolved chemical species as long as the concentration of particles is large compared to the inverse of the volumes

we are observing i.e. there are many particles diffusing and thus statistical variation is negligible.)

In the case of two adjacent bins with different numbers of particles (in a one-dimensional model), the net particle flux will be into the bin with fewer particles. Indeed, freely diffusing particles will tend to have a net diffusive flux in a direction down their concentration gradient with a magnitude proportional to the strength of the gradient. Diffusive fluxes can be calculated using Fick's law

$$\vec{J} = -D\nabla C \tag{1-16}$$

where $\vec{J}$ is the flux (in units of particles per time per area), C is the concentration of particles, and D the diffusion constant has units of area per time. Combing Fick's law with the continuity equation $\frac{\partial C}{\partial t} = -\nabla \vec{J}$ (which is a statement of conservation of number of particles), gives a simple form of the diffusion equation

$$\frac{\partial C}{\partial t} = \nabla D \nabla C \tag{1-17}$$

However, this form of the diffusion equation does not account for the effects of convection (convective flux). In microfluidics, the particles of interest are often suspended in a flowing medium. By adding the terms for convective flux we arrive at the convection-diffusion equation

$$\frac{\partial C}{\partial t} = \nabla D \nabla C + \nabla(\vec{v}C) \tag{1-18}$$

where $\vec{v}$ is the velocity of the medium in which the particles are suspended. (Meanwhile, D can often be treated as constant simplifying the equation.)

Returning slightly to the random walk picture of diffusion, there is another equation which is extremely useful for estimating the amount of time required for a diffusion process. The time it takes for the diffusing particles to wander out to a root-mean-squared displacement of r is given by

$$t_{diff} = \frac{r^2}{2nD} \tag{1-19}$$

where n is the number of dimensions. Interestingly, D can be calculated by

$$D = \frac{l^2}{2\tau} \tag{1-20}$$

where l is the step length of the random walk and τ is the time taken for each step. A useful way of estimating D for particles of a known radius r is the Stoles-Einstein equation

$$D = \frac{K_B T}{6\pi\eta r} \tag{1-21}$$

where K_B is the Boltzmann constant, T is the absolute temperature, and η is the dynamic viscosity of the fluid around the particle.

1.2: Microfluidic Device Design and Fabrication

Next, we discuss the actual physical form and manufacture of typical microfluidic chips relevant to the subsequently presented works.

The Physical Form of a Microfluidic Chip

The microfluidic chips discussed here all have a common construction. A microfluidic chip is simply a chunk of polydimethylsiloxane (PDMS) sealed against a glass cover slip. However, the chips have three components. The third component of a chip is actually a pattern of empty spaces. These empty spaces exist between the PDMS body and the glass as well as within the PDMS body. These patterned empty spaces are the microfluidic channels. The majority of channels have PDMS as three of their four walls with the fourth wall provided by the glass cover slip. This construction provides a glass viewing-window into the microfluidic channels (typically from below).

PDMS is a useful material for a number of reasons. PDMS is: biocompatible, translucent (often transparent), gas permeable, minimally autofluorescent, and fast curing. The features make it an excellent choice

as a material for rapid prototyping in both biotechnology and biological sciences.

Not all channels are designed to carry liquid medium. Chips can incorporate channels with a multitude of purposes. For instance, because PDMS is gas permeable, the dissolved gasses in a liquid channel will equilibrate with the gas blend held in a neighboring gas channel via diffusion. Such gas channels can be ventilated with specified gas blends in order to control the concentration of dissolved gasses in adjacent liquid medium channels. As a second example, special channels and chambers can be designed to mechanically actuate under the application of vacuum or gas pressure. There are on-chip pinch-valve style switches that work this way[6].

The PDMS body is typically a rectangular solid with a relief pattern of microchannels on one side (hereafter called the bottom of the chip) and vertically oriented cylindrical port channels cut through its bulk. These port channels serve as vias which connect to larger medium and gas supply tubing lines at the top of the chip and conduct the fluid down to the patterned microchannels.

For a typical design, a PDMS chip body is 5-8 mm thick and 2-5 cm wide and/or long. The microchannels have depths that can range from <1μm to >1mm, but flow channel thicknesses are most commonly in the 10-100 μm range. The widths of typical microchannels vary from ~10-500

μm but can be fabricated as small as 1 μm (by use of special photomasks). The cover slip used to seal the bottom of the chip is usually a standard #1.5 glass cover slip (~ 180 μm thick).

Fabricating the Chip

The microchannels forming the relief on the bottom of the PDMS body are made by molding. We use PDMS kits which include liquid PDMS base polymer and liquid PDMS crosslinker. When mixed (usually with a 10:1 ratio, respectively) the resulting mixture solidifies via a chemical reaction in which the ends of the base polymers link in at multiple sites along the backbones of the PDMS molecules in the crosslinker. However, this change is not that fast and the mixture remains liquid and easily pourable for a time (on the order of 10's of minutes at STP). During this time, the mixture can be poured into a mold and allowed to cure (crosslink) completely (often in an oven to accelerate the process). After curing, the PDMS is an elastic solid that holds the form of the vessel or mold in which it cured. Therefore, the challenge is to produce a mold with the desired microchannels patterned on its surface. The method we use to produce the patterned reliefs used for molding is photolithography.

1.3: Photolithography

In this section, we provide a basic description of photolithography, the method used to make molds for the production of microfluidic chips.

The microfluidic chips presented in this work were molded on silicon wafers with patterned SU8 photoresist epoxy relief structures produced by means of photolithography. In general photoresists are materials which can be solidified (negative photoresists) or dissolved (positive photoresists) upon or after exposure to light. This property allows fabricators to use patterned light to produce patterns of solid material. The process works as follows.

First, the fabricator spin coats a wafer with SU8 (by MicroChem). A clean polished silicon wafer is selected and placed on the wafer holder (rotor) of a spin coater. A sufficient amount of SU8 photoresist is poured onto the center of the wafer. The wafer is rotated for a set amount of time at a set angular velocity by the spin coater causing the SU8 to spread over the surface of the wafer. The fluid dynamics of this process cause the liquid layer to converge toward a single uniform thickness over the entire surface[7]. The final thickness of the SU8 layer is primarily dependent on: the angular velocity of the wafer, the duration of time the wafer spends rotating, and the kinematic viscosity of the SU8. The final thickness is also dependent on the initial thickness of the SU8. However, in the case of spin coating with a sufficient excess of SU8, the end thickness is much more

dependent on the spin time, angular velocity, and kinematic viscosity of the SU8 than it is dependent on the volume of SU8 initially dispensed on the wafer. This is due to two reasons. One, the rate that the droplet (1-5 ml) of SU8 spreads over the surface is fast when compared with the rate of thinning of the layer. Two, the rate that the layer thins is roughly proportional to the third power of its thickness. Therefore, the layer is initially near uniform after spreading over the surface, and subsequently all of the thicker regions of the layer thin more quickly than the other regions. The third power dependence also means that if a large excess of photoresist is poured (perhaps the initial thickness as the photoresist layer coats the wafer is twice the normal amount), then the initial rate at which the layer thins will be greatly increased (a factor of ~8). SU8 product family has a spectrum of SU8 photoresist blends with a verity of viscosities. Each blend is catered toward use in the production of a particular range of thicknesses. The fabricator can produce a photoresist layer of a precise thickness by first selecting the SU8 type (viscosity) and then selecting the angular velocity and spin time.

Second, the fabricator removes the solvents from the SU8 layer by placing the SU8 coated wafer on a 65° C hotplate (for thermal ramp up ~1-5 min depending on the thickness) and then a 95° C hot plate (for 3-400 min depending on the thickness). Afterward, the wafer is cooled slowly on a thermally insulated surface.

Third, the fabricator, places the SU8 coated wafer on a suction based wafer holder and then lowers a piece of film (called a photomask) with patterned opaque and transparent regions directly into contact with the surface of the SU8. The wafer is then exposed to UV light through the transparent parts of the photomask from above. This causes the exposed regions of the SU8 layer to photoactivate.

Fourth, once again the wafer is placed on a 65° C hotplate (thermal ramp up) and then a 95° C hot plate (for 3-20 minutes depending on the thickness); and allowed to cool slowly afterword. This heating process provides activation energy for the photoactivated portions of the SU8 to solidify and become chemically resistant to 1-methoxy-2-propanol acetate (SU8 developer).

Fifth, the fabricator places the wafer in a container filled with SU8 developer. The wafer is then washed in the developer by gently shaking the container. The unexposed regions of the SU8 dissolve into the developer, revealing a solid SU8 relief in the same pattern as the transparent regions of the photomask.

The aforementioned steps can be repeated with multiple photoresist depths and photomasks in order to produce a “two-and-a-half” dimensional patterned relief having multiple depths. Multilayered patterning allows for the production of sophisticated microfluidic devices with features such as cell traps and mixers.

Before use as a mold, the wafer and SU8 relief pattern are exposed to trichloromethylsilane vapors (at STP) for 2-30 minutes to make the surface nonstick.

In entirety, this process produces a patterned SU8 relief on a wafer that can be used as a master mold for making PDMS chips as previously described.

1.4: Standard Experimental Setup

There are many ways to control flow in a microfluidic device. This section describes the essential methods used in this work. First, we will begin to get familiar with chip operation by discussing the operation of the simplest relevant chip architecture. Then we will discuss important features that can be added to the design to improve performance and usability, and to enable essential functions.

Arguably, the simplest possible microfluidic chip has only an inlet port and an outlet port with a straight rectangular channel between them. In a standard setup for this chip, a piece of tubing delivers liquid (typically an aqueous solution) from a reservoir container to the inlet port. That liquid flows down the channel to the outlet port from whence it is delivered to an outlet (effluent) reservoir container by another piece of tubing. If the

chip is functioning properly, there is one continuous liquid phase medium from the inlet reservoir to the outlet reservoir.

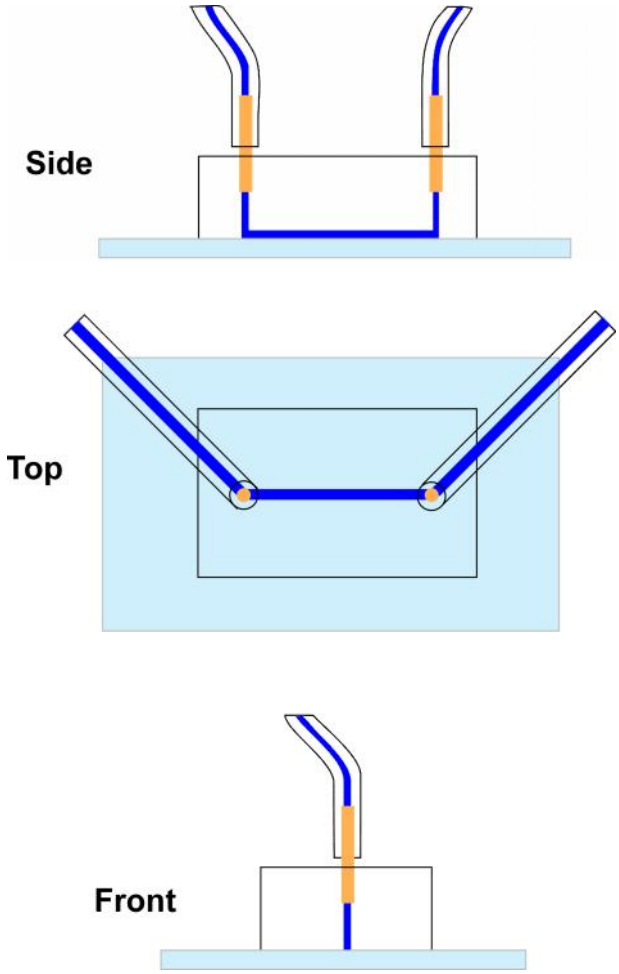

Figure 1-2: Cartoon of the simplest microfluidics chip as viewed from the side, the top and the front.

Pumps, air pressure, and electric fields can be used to drive flow through microfluidic devices; however, the simplest way to drive a flow is by gravity (hydrostatic pressure). In gravity driven flow, the pressure gradient caused by the difference in the height of the "water column" in the inlet reservoir relative to the height of the "water column" in the outlet

(hydrostatic pressure) drives the flow. As discussed in section 1.1.2, the viscosity of the medium resists the flow, resulting in a steady state flow.

For the simple design we have introduced, it is likely that the tubing used will contribute significant resistance to the flow circuit. Whether the resistance in the tubing is significant is determined by comparing the resistance of the tubing to the resistance of (the channel(s) in) the chip (in this case a single straight channel). If the resistance of the tubing is significant, great care must be taken to ensure repeatability between experiments, because using tubing of a different length with result in a different flow rate (for the same hydrostatic pressure). Furthermore, the resistance of the chip and tubing may be so low that small changes in hydrostatic pressure results in significant changes in flow rate. Therefore, most chips incorporate serpentine resistance channels that provide an amount of resistance sufficient to limit the sensitivity of the flow rate caused by unintended variations in pressure (differences between the inlets and outlets). Ideally the resistance is such that, the range of pressures available to an operator (experimentalist) map to the range of flow rates that the operator intends to use. The inclusion of a resistance channel often makes the resistance due to the other components of the chip as well as the resistance due to the tubing negligible. As a result, once a serpentine resistor channel has been incorporated into a design, the designer can select the geometry of the remainder of the chip without

having major effects on the total resistance of the chip, and the operator does not need to worry, to any great extent, about the effects introduced by variations in tubing length.

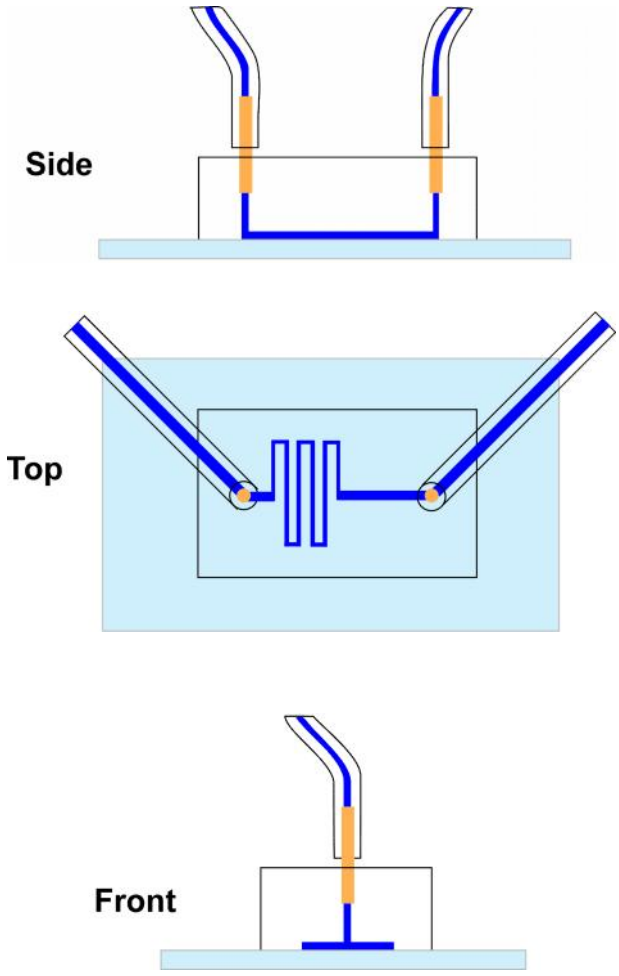

Figure 1-3: Cartoon of a microfluidic chip with a serpentine resistor as viewed from the side, the top and the front.

Our simple chip has been getting more complicated, but also a great deal more useable. Next, we consider changes that make it more useful. A chip with only one channel has limited applications. Additional inlets and outlets open up a range of additional functions. For instance two inlet

channels can have an intersection (junction) to which they bear different media. The media could carry reactants that the operator would observe reacting. Alternatively, the downstream region might hold living cells and the media could contain different amounts of dissolved chemical, enabling the operator to observe and characterize the response of the cells to different concentrations of the chemical. For instance, the mixing ratio at a junction can be controlled by setting the pressures of its respective sources. One inlet medium reservoir can be set higher than the other in order to increase its relative flow rate. If the operator is interested in making repeated changes to one or more of the flow rates, it may be more convenient to apply additional pressure pneumatically.

Pneumatic control systems are convenient because they enable the operator to change the pressure applied at one or more of the ports without moving any of the reservoirs. The essential components in a pneumatic control system are a source of compressed gas (usually air), pressure regulator(s), pressure indicator(s), stopcocks or valves, tubing, and connectors. In systems with no pneumatic control, the liquid reservoirs are open to the atmosphere and the pressure in their headspaces is that of the outside atmosphere. However, in pneumatic systems one or more of the reservoirs' headspaces is isolated from the atmosphere, and instead connected to a three-way stopcock (valve) that in one state connects that headspace to a regulated pressure source and in another state vents it to

the atmosphere. The use of electrically actuated solenoid valves in place of manual stopcocks enables the incorporation of precise computer controlled timing.

In biology research microfluidics is often used to produce well controlled microenvironments. Biologists are often interested in observing how a model system (cells or animal) responds to its surrounding environment. Therefore, microfluidic systems of this type are intentionally designed to allow for precise control of specific aspects of the environment in the chip. The environmental aspects to be controlled can include such variables as concentrations of chemoattractants, chemorepellants, or other dissolved chemicals (including hydrogen ions and dissolved gasses); temperature; shear force; etc. This also includes the variation of these properties in space and time. For instance, chemotaxis is a well-known phenomenon in which an organism will move in response to the chemical conditions (typically gradients of chemicals) in its surroundings. A microfluidic chip designed to enhance studies of chemotaxis in chemical gradients should be able to produce a chemical gradient of sufficient magnitude to invoke the organism to respond. It would also be preferable that the gradient be reproducible and adjustable.

In order to be useful for making measurements on a biological model organism a chip must host that organism in a fashion that allows for measurement. For instance, a chip (system) designed for measuring the

growth rates of single cells of *E. coli* will need to incorporate some form of trap in order to retain each cell for successive measurements.

Of course, the reason for using microfluidics in scientific applications is to enable the collection of otherwise inaccessible data. The most common means of data acquisition in our work is the inverted fluorescence microscope. In a typical setup, the microfluidic chip is placed on the stage of an inverted microscope as if its coverslip were an ordinary coverslip with a sample on it. (It is often necessary to tape the chip in place on the microscope ring, due to the rigidity of the tubing lines.)

1.5: Fluorescence Microscopy

We use fluorescence microscopy for the characterization of microfluidic devices, as well as, the collection of biological data. A fluorescence microscope works by the same principals as any optical microscope, with the added feature of being able to direct filtered excitation light at a sample and collect (and filter) the light which is fluorescently emitted by fluorophores in the sample.

An excellent source of information about fluorescence microscopy is the book "Fluorescence microscopy" by B. Herman[8]. Herman states that the main components of a fluorescence microscope are the excitation light source, wavelength selection devices, objectives, detectors, and stages/specimen chambers.

The most common excitation lights sources are high-powered lamps (mercury, xenon, or both), lasers, and light emitting diodes (LEDs). Lasers and LEDs can produce monochromatic and nearly monochromatic illumination of stable intensity. LEDs that can produce broad fields of illumination with ample intensity are not prohibitively expensive. Standard lamp housings can be easily adapted to hold a star LED mounted to a heat sink and fan system.

During my time in the Groisman Lab, I developed a new way of mounting the LED within the lamp housing that uses magnetism to provide enhanced adjustability. In short, the LED is mounted on a cooling fan as per usual. However, a thin but rigid ferrous metal bar is mounted across the back of the LED-cooling-fan unit, and a magnet is attached (using epoxy) to the desired mounting point in the lamp housing (the end of the post where the lamp mirror previously was). The LED-cooling-fan unit can be easily installed without the need for any tools by simply placing the metal bar on the back of the LED unit against the magnet in the housing. Most importantly, the position of the LED can be adjusted freely without the need for tools by simply sliding the LED unit along its interface with the magnet. (This interface has sufficient static friction to stop movement due to gravitational forces.)

For wide field light sources like lamps and LEDs, the light form the excitation light source is gathered by a set of lenses called a collector lens assembly that collimates the light and projects it onward.

Next, the excitation light is filtered by some of the components in the aforementioned wavelength selection device (cf. Fig. 1-4). The collimated excitation light to be filtered is directed at a wavelength selection device called a filter cube. The filter cube has three primary optical components an excitation filter, an emission filter and a dichroic mirror. These three filters are referred to as a "filter set". Typically, the excitation light is at a shorter wavelength than the emission light we intend to collect form the sample. The excitation light enters the filter cube through the excitation filter, which only allows photons of a certain range of frequencies to pass. The light which passes through the excitation filter then hits the dichroic mirror which is oriented at a 45° angle relative to its travel path. Typical dichroic mirrors have the property of being reflective to light of sufficiently short wavelengths but transparent to light of sufficiently long wavelengths. (Ideally, the transition between the reflected and transmitted wavelengths has a sharp cutoff in frequency space.) By the time the excitation light hits the dichroic mirror, the excitation filer should have filtered it such that it only contains wavelengths that will be reflected by the mirror. The dichroic mirror reflects the excitation light directing it upward into the objective (cf. Fig. 1-4).

The objective is a collection of lenses contained in a metal cylinder. The cylindrical body of the objective is threaded at its base such that it can be mounted to a rotating tray assembly on the microscope. The excitation light enters the “rear lens” of objective and exits the “front lens” coming to a focus a short distance away (cf. Fig. 1-4).

A sample for observation is mounted to a stage such that that the excitation light is focused on a region of interest on the sample. In the case of this work, the samples will be inside of microfluidic devices mounted on x-y stages. In a fluorescence experiment, some of the excitation light is stochastically absorbed by fluorophores in the sample; exciting electrons in the fluorophore molecules to jump from the highest occupied molecular orbital to the lowest unoccupied molecular orbital. Subsequently, the excited electrons will emit photons as they stochastically fall back into their old orbitals with a given decay lifetime (fluorescence lifetime). These fluorescently emitted photons have a spectrum in frequency space defined by the structure of the fluorophore and the conditions in its surrounding environment. By gathering these emitted photons and measuring them we can make observations that give us insight about the environment around the fluorophore. There are a multitude of fluorophores that can be used to gather information about different physical and biological processes. For instance tris(2,2 -bipyridyl)dichloro-*ruthenium*(II) hexahydrate (RTDP) is a fluorescent dye which glows less brightly (due to quenching) in the

presence of increased concentrations of oxygen and can therefore be used to measure oxygen concentration in a microenvironment. As another example there is a whole rainbow of fluorescent proteins (most famously green fluorescent protein) the DNA that codes for which can be inserted into the DNA of a model organism in conjunction with DNA that codes for other essential proteins. The fluorescence of the GFP can then be used as an indicator of the production of said protein. Furthermore, the GFP insertion can often be made contiguous with the code of the protein of interest such that when it is produced it will have a GFP attached. In this case the fluorescence of the GFP can also give the researcher insight as to the position of the protein within the cell.

The emission light from the fluorophore in the sample radiates in all directions. Some of the emission light is collected by the objective. The objective collects light only from a thin plane (the focal plane) near its front lens. (The thickness of the focal plane is called the depth of field and the distance from the front lens of the object to the focal plane is called the working distance.) The objective directs the collected emission light into the filter cube where it first hits the dichroic. Some of the emission light of shorter wavelengths is reflected back towards the light source components, while emission light with longer wavelengths passes through the dichroic mirror and into the emission filter for further refinement (cf. Fig. 1-4). The

goal is to measure emitted photons from a well defined set of wavelengths. The filter set must be chosen carefully for any given fluorophore system.

Emission light which passes through the emission filter will exit the filter cube and hit a mirror (or system of mirrors) which directs the light into the detection system. Often times there are multiple detection devices setup on the microscope at different ports. The mirror is often able to rotate in order to select which port and detection device will receive the emission light.

The earliest detection device used in microscopy was the human eye, and it is still useful to this day. Most microscopes have a devoted port with oculars for the operator to view the filtered emission light directly. However, in the work presented here quantitative data was recorded using the pixel arrays of CCD cameras. Other detection devices commonly used in fluorescence microscopy are photomultiplier tubes and avalanche photo diodes. All of these devices attempt to achieve the same goal of counting the number of photons which hit them over a given integration time (like a meteorologist totaling annual rainfall).

In the case of CCD cameras, the micrograph images from the pixel array can be saved to a computer in real time and analyzed later.

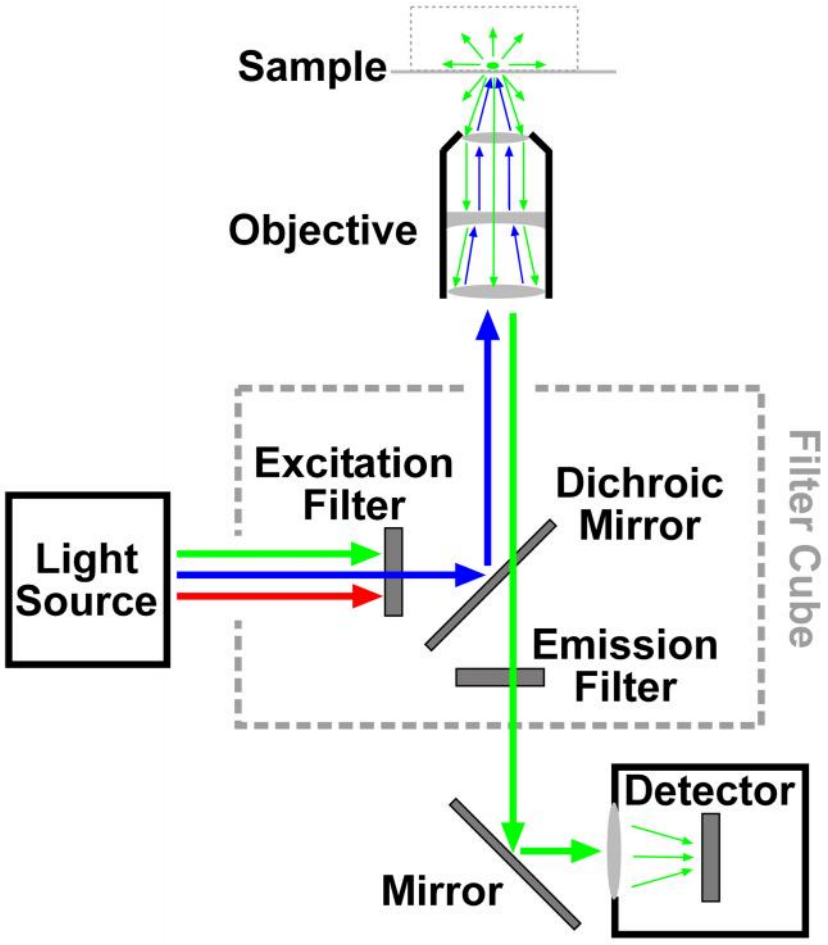

Figure 1-4: Block diagram of the optical path in a fluorescence microscope. The glowing green spot in the sample can represent a well or channel with green dye (i.e. fluorescein isothiocyanate) in it, or a cell expressing green-fluorescent-protein. For the filter set shown here, the desired excitation light is in the blue part of the spectrum and the desired emission light is in the green part of the spectrum. For the purposes of simplicity, this figure does not show the undesirable light rays caused by unintended reflections and filter leakage.

1.6: Organization of the Dissertation

The remainder of the dissertation incorporates three chapters. Each of these chapters report work which has been submitted for publication or

is in the process of being prepared for submission for publication. All of these works are interrelated. In chapter 2, I present a new UV light source designed for use in photolithography. The goal of this new technology was to produce an LED based source of collimated UV light which costs far less in parts and labor, has far less maintenance, and consumes far less electrical power than traditional high-pressure lamp based designs. The system described in chapter 2 was an essential component used in the production of the microfluidic devices presented in chapters 3 and 4.

In chapter 3, I present a microfluidic experimental system designed to control the concentration of dissolved oxygen around a zebrafish larva as a function of time while confining it so that the experimentalist can observe its behavioral responses. To our knowledge this system is the first to attempt to hydrodynamically confine unanesthetized zebrafish larvae. The system can change the concentration of dissolved oxygen in the specimen area between normoxic and hypoxic levels in seconds evoking behavioral responses on the order of 10 seconds. Previous apparatuses for this purpose have typically been based on bubbling with changes of dissolved oxygen concentration imposed over ~60 or more seconds.

In chapter 4, I present a microfluidic experimental system designed to sweep concentration waves of chemoattractant molecules over a population of amoebas. To our knowledge it is the first of its kind, exposing cells to bell shaped chemoattractant profiles much more akin to those

encountered during their natural chemotactic process with the added benefit that the experimentalist can control many of the parameters of the wave.

Chapter 2: Advances in Photolithographic Technology

2.1: A low-cost low-maintenance ultraviolet lithography light source based on light-emitting diodes

Abstract

A source of collimated ultraviolet (UV) light is a central piece of equipment needed for lithographic fabrication of microfluidic devices. Conventional UV light sources based on high-pressure mercury lamps require considerable maintenance and provide broad-band illumination with intensity that often changes with time. Here we present a source of narrow-band UV light based on an array of nine 365 nm light-emitting diodes (LEDs). Each LED has two dedicated converging lenses, reducing the divergence of light emanating from it to 5.4°. Partial overlap of the areas illuminated by individual LEDs provides UV illumination with a mean intensity of ~1.7 mW/cm^2 and coefficient of variation <3% over a 90×90 mm target area. The light source was used to lithographically fabricate micro-reliefs with thicknesses from ~25 to 311 μm with SU8 photoresists. A cumulative irradiation of 370 mJ/cm^2 (4 min exposure) produced reliefs of good quality for all SU8 thicknesses. Polydimethylsiloxane (PDMS) replicas of the SU8 reliefs had

microchannels with nearly rectangular cross-sections that were highly consistent over the entire target area, and partitions between the channels had depth to width ratios up to 5. The UV light source is built with a total cost of <$1000, consumes a minimal amount of power, and is expected to last for ~50,000 exposures, maintenance-free. The proposed light source can be used with other photoresists sensitive to 365 nm light to fabricate a broad variety of microfluidic devices, and is particularly appealing for small research-and-development microfluidic fabrication.

Introduction:

Microfluidic devices made of silicone rubber are widely used in the research community. Master molds for these devices can be rapidly fabricated by using photolithography to form various reliefs of photoresist on silicon wafers. This process of rapid prototyping is particularly appealing, because it does not require much space and equipment. A common choice of photoresist for rapid prototyping is one of the ultraviolet (UV)-curable epoxies from the SU8 family. The SU8 epoxies enable the fabrication of microchannels with a broad range of thickness, from <1 to >500 μm, with nearly rectangular profiles, and large ratios of their depths to widths (aspect ratios). Rectangular microchannels are completely defined by their width, depth and length, facilitating the calculation of flow through them and making microfluidic networks largely reproducible.

The single most expensive piece of equipment required for the rapid prototyping of microfluidic devices using UV lithography is a source of collimated UV light (UV flood source). A standard UV flood source is built around a powerful high-pressure mercury lamp and requires a matching power supply with a feedback loop for steady illumination. A UV flood source also usually has elements absorbing infrared (IR) and visible light (to reduce heating of the target), an electro-mechanical shutter to control the exposure, and UV-transparent optical elements to collimate and uniformly distribute light over a large target area. Even if the light source is only used sparsely, mercury lamps are often kept on continuously because of their long warm-up times and the adverse effect that restarting has on their longevity. As a result, in addition to the cost of replacement of the mercury lamps, the power costs alone can be as much as $1000 a year.

The light produced by mercury lamps has a broad spectrum, including bright lines in deep UV, making them versatile sources of illumination for fluorescence microscopy and UV lithography. Nevertheless, deep UV light represents a problem for fabrication of tall reliefs of SU8, which are required for deep micro-channels in PDMS. The UV absorbance of SU8 sharply increases at wavelengths below 350 nm, and to obtain straight walls for relief features taller than ~25 μm the manufacturer recommends filtering those wavelengths out. Among additional problematic features of mercury light sources are fluctuations in

the spatial distribution of illumination and continuous drift in the intensity of illumination.

High-power light-emitting diodes (LEDs) have been increasingly replacing mercury lamps in light sources used for fluorescence microscopy[1-3]. Whereas LEDs may still be inferior to high-pressure mercury lamps in terms of the maximal intensity of illumination, LEDs have multiple advantages, including narrow emission bands, stable illumination patterns with steady and reproducible light intensity, very short response times, and low power consumption. LEDs are even more appealing for light curing applications, where the light intensity is usually relatively low and a large area can be illuminated nearly uniformly by an array of evenly spaced LEDs with no additional optical elements involved. Affordable high-power LEDs are currently available with wavelengths as short as 365nm, and LED-based near-UV curing systems are now offered by multiple manufacturers. Arrays of near-UV LEDs have also recently been used by several groups for contact lithography. These arrays were assembled from large numbers of low-power individual LEDs, which had relatively large divergence of light emanating from them (large viewing angles). Large divergence angles and the resulting overlapping of light from multiple individual LEDs can improve the spatial uniformity of illumination[4], as required for UV curing and contact lithography with thin layers of photoresist. However, if applied to thick layers of SU8 to fabricate

PDMS microfluidic devices with deep micro-channels (e.g., 100 μm or more), UV illumination with large divergence is expected to result in uneven exposure through the thickness of SU8, produce features with uneven width, and complicate the fabrication of features with large aspect ratios. Reductions in the divergence of light (improvement of its collimation) have been achieved by blocking the light emerging from the sides of LEDs in a large array[5]. Nevertheless, the resulting illumination pattern was visibly uneven, bearing clear fingerprints of the locations and internal structure of individual LEDs. Nearly-uniform illumination has also been achieved with a single large-area LED[6]. However, this LED had a full width at half-maximum (FWHM) viewing angle of ~100°, making it difficult to combine uniformity of illumination with high intensity and low divergence.

Materials and Methods:

Here we present a UV lithography light source based on a square array of nine high-power LEDs (nominal radiant power of 320 mW at a current of 0.7 A) with a central wavelength of ~365 nm (Fig. 2-1). The LEDs (LZ1-10U600 by LED Engin, San Jose, CA) are mounted on a 3/16" aluminum base plate in a 3×3 square array with a pitch of 50 mm. To prevent excessive heating of the LEDs, which dissipate ~3W each at a 0.7 A current, five fans with standoffs are mounted on the base plate, with

four smaller fans on the same side as the LEDs and a larger fan on the back side. The divergence (viewing angle) of light coming from individual LEDs is reduced from ~80º to ~12º FWHM by gluing a commercial light-collecting UV lens (FCN12592_LE1-D-COP, by LEDiL, Finland) to each LED.

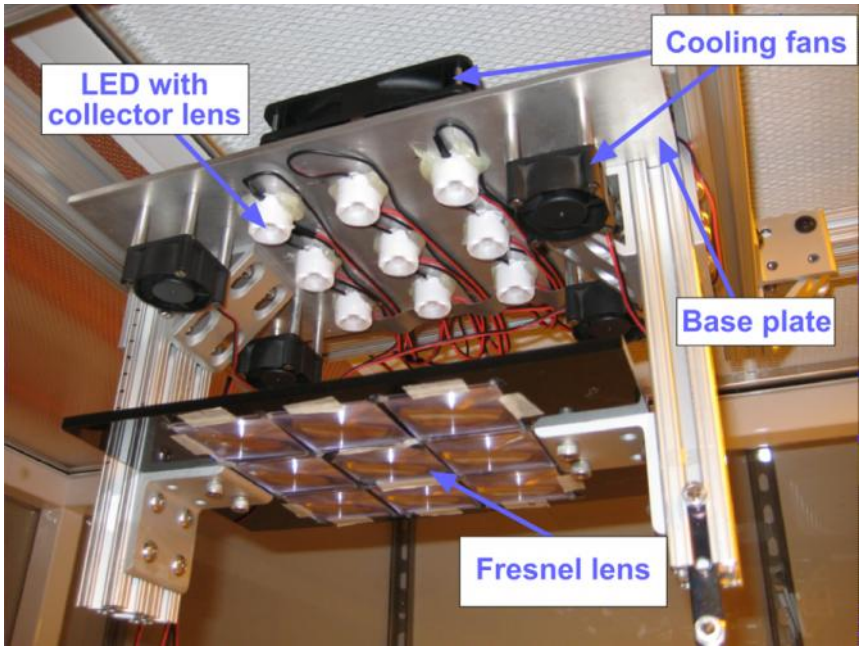

Figure 2-1: Photograph of the LED UV light source mounted to ceiling of clean room using 80/20 extrusions and brackets.

To further reduce the divergence, we use a 3×3 square array (with the same pitch of 50 mm) of nine identical converging polyvinylchloride (PVC) Fresnel lenses with a focal length $f \approx 180$ mm. The lenses are mounted on a black acrylic plate with 44 mm apertures and positioned at a distance of ~127 mm from the base plate (~124 mm and ~109 mm, respectively, from the emitting surfaces of the LEDs and the front surfaces

of the collecting lenses). The thin PVC lenses (#401B, http://www.3dlens.com) are chosen because of their low cost and high transparency at 365 nm. Placing a converging lens at a distance L < f from a point source of light reduces the divergence of the beam from the source by a factor of $f/(f-L)$. With the front surface of a collecting lens taken as the new source of light, corresponding to L=109 mm, this equation predicts the divergence to decrease from ~12° to ~4.7°. However, because of the large thickness of the collecting lenses (~15 mm) and complex light paths in them, the value of ~4.7° can only be used as an estimate.

For the light source to illuminate the target evenly, the beams from adjacent LEDs must partially overlap[7]. Given the relatively large distance between the individual LEDs and the low beam divergence, the light source in the proposed setup must be placed a sufficient distance from the target to achieve sufficient beam overlap. To this end, we use the simple practical solution of mounting the light source on the ceiling of our modular clean room. The distance from the base plate to the target (photomask holder) is 0.96 m. The mounting setup includes aluminum extrusions (rails), connecting plates, brackets, and corner gussets from 80/20 Inc. (Columbia City, IN), which are used to align the light source with the target area (photomask holder) and to adjust the distance between the Fresnel lens array and the LED array for optimal illumination.

The LED array is powered by a 40V, 2A digital power supply (by Lambda). Because the radiant power of an LED is primarily the function of the current, the power supply operates in current regulating mode and the LEDs are connected in series. To adjust the illumination, the currents through the four LEDs in the corners, four LEDs at the edges, and the LED in the center are tuned separately (Fig. 2-5). To this end, a potentiometer is connected in parallel with the five LEDs that are not in the corner positions, and another potentiometer is connected in parallel with the central LED. The exposure time is controlled with a multi-function time delay relay with mechanically adjustable intervals from 0.1 sec to 60 hrs (H3CR-A8 by Omron).

Results:

The distance, L, and the currents through different groups of LEDs were adjusted to achieve high uniformity of illumination without substantially compromising its intensity or collimation (and it is as a result of this adjustment that L was set to 109 mm). The currents through the corner, edge, and central LEDs were set at 0.6, 0.3, and 0.15 A, respectively. Photographs of the UV illumination fields produced by individual LEDs and all LEDs together (Fig. 2-7) did not show appreciable variations of intensity at scales smaller than ~25 mm (half of the pitch of the LED array). Therefore, we measured the UV intensity distributions

directly using a UV power meter (#0306-001-4 by OAI) with a 6.5 mm diameter optical window and a peak response at 365 nm. Illumination spots produced by individual LEDs had diameters (FWHM) of ~42 mm at the target and ~30 mm at 250 mm above it, corresponding to a divergence angle of 5.4°, in reasonable agreement with the theoretical estimate of 4.7°.

To obtain a detailed map of the illumination field, we divided a 120×120 mm area around the center into a 12×12 array of 10 mm squares and measured the UV intensity in the middle of each square with the power meter. The results (Fig. 2-2) indicated that in the central 90×90 mm target area (square photomask used with a 5 in. wafer), the intensity had a mean value of 1.75 mW/cm^2 with an SD of 0.05 mW/cm^2, corresponding to a coefficient of variation (CV) of 2.9%. The peak-to-peak variation of the intensity was 0.26 mW/cm^2, corresponding to 15% of the mean. With the four squares at the corners of the 90×90 mm target area excluded, the peak-to-peak variation dropped to 11% of the mean.

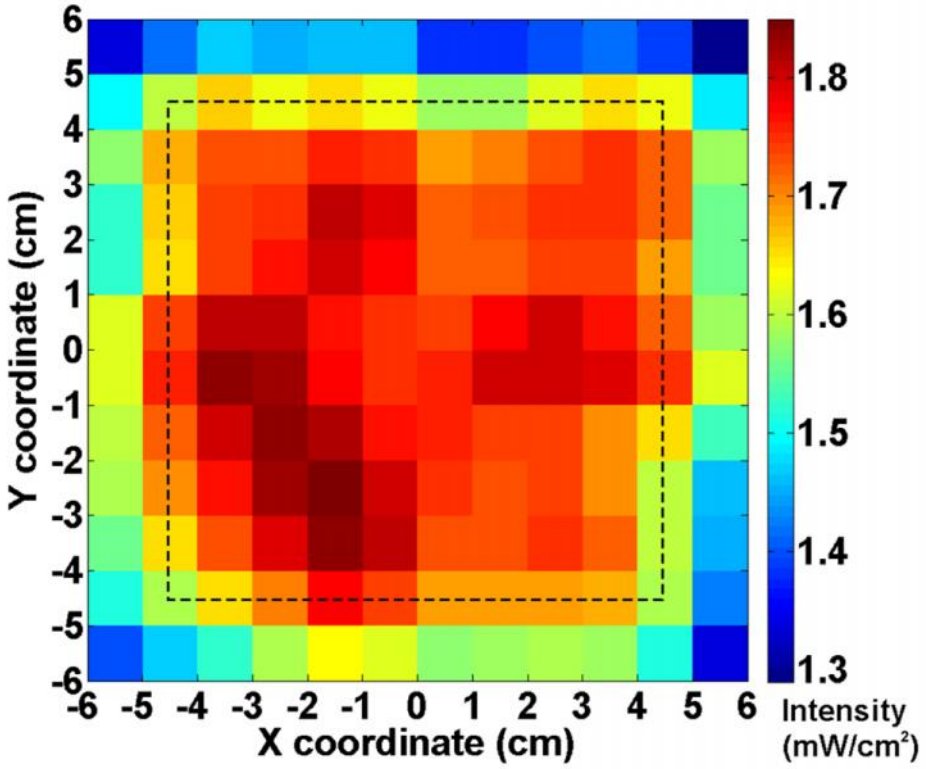

Figure 2-2: Color-coded plot of the UV intensity in a 12×12 cm region centered at the 9×9 cm target area (delineated by the dashed black square), as measured in the centers of 1×1 cm squares with a UV power meter with peak sensitivity at 365 nm. (Note that the lowest intensity is 1.3 mW/cm^2 rather than 0.)

To test the utility of the UV light source for fabrication of microfluidic devices in PDMS, we used a photomask with a 5×5 array of 18 mm squares with identical test patterns, each having 4 identical clusters (for testing 4 different exposure times) of transparent strips with widths from ~23 to ~160 µm and separations from ~17 to ~78 µm. (After passing through a transparent area of the photomask mounted on a 0.080" glass support, the UV light intensity decreased by ~22%.) The photomask was

used with three 5 in. wafers, which were spin-coated with 25±1 μm, 160±28 μm, and 311±11 μm (mean±SD) thick layers of the SU8 photoresist. After the wafers were exposed to UV through the photomask, post-baked, and developed (Fig. 2-3a and 2-8), a PDMS (Sylgard 184 by Dow Corning) replicas were made and cut into 25 square chips, corresponding to the 25 copies of the test pattern on the photomask (Fig. 2-3b). Each chip was then sliced in the vertical plane perpendicularly to the microchannels, which were the replicas of the SU8 ridges produced by the transparent strips on the photomask. The cross-sections of the microchannels were photographed under a darkfield microscope (Fig. 2-3c).

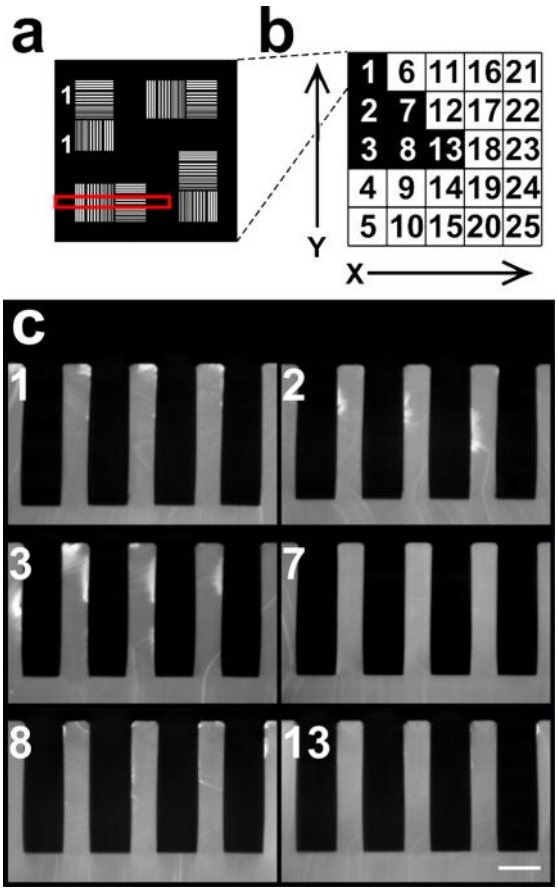

Figure 2-3: PDMS chips with 311 µm deep microchannels fabricated using a test photomask. (a) Fragment of the photomask showing one 18×18 mm test pattern from the 5×5 array of identical test patterns. Each test pattern has four identical clusters of transparent strips, which include four strips each: 23 µm wide with 17 µm separations, 41 µm wide with 39 µm separations, 82 µm wide with 78 µm separations, 160 µm wide strips 80 µm separations, four 163 µm wide with 157 µm separations. The red rectangle marks an area of the PDMS chip made with the photomask that is cut and examined under a darkfield microscope. (b) A map with continuous enumeration of the test patterns in the 5×5 array. (c) Micrographs of cross-sections of microchannels in PDMS chips cast from 6 representative regions of the wafer with different locations within the 5×5 test pattern array, as indicated by numbers, corresponding to the highlighted squares in panel b. The microchannels are replicas from relief features produced by a 6 min exposure of a 311 µm thick (on average) SU8 layer through 82 µm wide transparent strips with 78 µm separations. The micrographs are taken with a 10x objective under darkfield illumination. Scale bar 100 µm.

For the 311 μm SU8 layer, exposure times of 4, 6, 8, and 10 min were tested. Best results were obtained with the 6 min exposure (Fig. 2-9), corresponding to a cumulative irradiation of ~490 mJ/cm^2. Specifically, in all 25 test areas, arrays of 82 μm wide transparent strips with 78 μm separations produced arrays of well-separated channels (Fig. 2-3c). The cross-sections of individual channels in different test areas were analyzed by digitally processing their micrographs using a code in MatLab to obtain the channel widths at different distances from the surface of the PDMS chips (excluding most proximal and most distal 10 μm) (Fig. 2-4). (The digital processing procedure is described in chapter 2.2.) The peak-to-peak variations of widths of individual channels in different test areas ranged from 4.46 μm to 14.0 μm, with the SD ranging from 1.2 μm to 4.3 μm (Fig. 2-4). When normalized to the average channel depth of 311 μm, these numbers corresponded to a peak-to-peak variability of 1.4% to 4.5% and CV of 0.4% to 1.4%. Importantly, channel width at the positions most proximal and most distal to the surface of PDMS, corresponding to "bottoms" and "tops" of the SU8 ridges on the wafer, differed by <4.2 μm on average (CV<1.3%), suggesting that the channel cross-sections were near-rectangular, as expected for uniform and collimated UV irradiation of the SU8 photoresist. The average widths of the channels in the 25 test regions varied from 92 μm to 102 μm with a mean of 96 μm and an SD of 2.4 μm,

corresponding to SV of 0.75% (when normalized to the channel depth again).

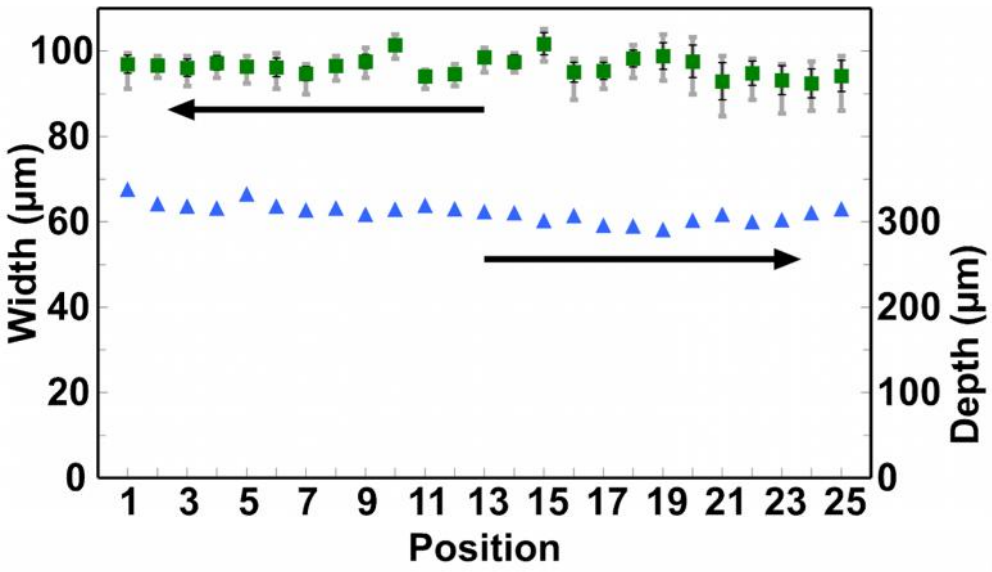

Figure 2-4: The width of a microchannel averaged over its depth (green squares) and microchannel depth (blue triangles) for each position within the 5×5 test pattern array. All microchannels are replicas of ridges produced by a 6 min UV exposure of a 311 μm thick (on average) layer of SU8 through 82 μm transparent strips. Black error bars show standard deviations of the widths; grey error bars show ranges of widths measured.

We note that, whereas there is an appreciable difference between the mean width of the channels and the width of the transparent strips on the photomask, this difference can be accounted for in the design of the photomasks. The differences between the cross-sections of nearby channels in the arrays of four (cf. Fig. 2-3c) were smaller than but comparable to the differences between channels from different test areas (Fig. 2-9). The mean widths of the channels and partitions (~64 μm) correspond to aspect ratios

(depth/width) of ~3 and ~5, respectively, which are both relatively high for microchannels cast in PDMS. The 4 min exposure resulted in a closer matching between the mean width of the microchannels and the width of the transparent strips on the photomask (89 vs. 82 μm) at expense of reduced uniformity of the channel widths (Fig. 2-10).

For the 160 and 25 μm SU8 layers, the optimal exposure times were 4 and 3 min, respectively (Fig. 2-11 and 2-12). The widths of the microchannels matched the widths of the transparent strips more closely, 92 vs. 82 μm for the 160 μm layer and 26 vs. 23 μm for the 25 μm layer. The average values of CV of the channel width were 0.9 and 2.9% for the 160 and 25 μm layers, respectively, and partitions between channels had mean aspect ratios of ~2.4 and ~1.8, respectively. The UV light source was also successfully used to produce SU8 reliefs as thick as 1 mm (Fig. 2-13).

Discussion and Conclusions:

The proposed LED-based UV light source is an effective tool for SU8 photolithography aimed at the fabrication of rectangular microchannels in PDMS with a variety of depths. The UV light source provides collimated uniform illumination over a large area, making it possible to fabricate microchannels with consistent widths and high aspect ratios. Unlike a mercury lamp UV light source, neither the spatial pattern nor light intensity of the LED light source changes with time, eliminating the need

to periodically calibrate the illumination and modify the fabrication protocols.

The narrow spectrum of the LEDs, which is centered at 365 nm, corresponding to a characteristic SU8 absorption length of ~370 μm[8], leads to a relatively weak dependence of the optimal exposure time on the thickness of SU8 layer, making the fabrication more forgiving. So, in our tests, good quality reliefs of SU8 with thicknesses from 25 to 311 μm (and good-quality PDMS microchannels with the corresponding depths) were produced using a single exposure time of 4 min, corresponding to 330 mJ/cm^2 cumulative irradiation. Furthermore, we noticed that thick (>200 μm) SU8 patterns were more robust and strongly adherent to the wafers when made with the LED source rather than a 350 W mercury lamp UV flood source equipped with a colored-glass long-pass filter (Schott WG-360, with 50% absorption at 360 nm). We explain this increased robustness and adhesion by the narrower spectrum of the LEDs with no deep UV light in it, leading to greater uniformity of the exposure over the SU8 depth. As of now, our lab has completely switched to using the LED-based UV source for SU8 photolithography and stopped using the mercury lamp source (made by OAI and priced at ~$15,000 in 2002) that we have been using during the last 11 years.

The LED-based UV light source costs <$1000 in parts, materials, and machining to build, and because the LEDs are only powered during

the UV exposures and are expected to last ~5000 hrs (50,000 exposures of 6 min), its maintenance costs are close to zero. The intensity of the illumination can be substantially increased and the exposure times can be proportionally reduced using recently introduced 365 nm LEDs (LZ1-00UV00 by LED Engin), which are ~2.5 times more luminous than the LEDs used in our source. In addition, the collimation and uniformity of illumination can likely be further improved by customizing the geometry of the LED array (e.g., using a triangular array with a different pitch)[7]. Whereas the LED light source has only been tested with the SU8 photoresists, it is likely to be effective for all photoresists sensitive to 365 nm UV. The low costs of manufacture and maintenance of the light source make it particularly appealing for microfluidic research applications and for small academic and industrial fabrication facilities in general.

Acknowledgements: We thank Philibert Tsai for illuminating discussions. The work was partially funded by NSF PHY 1205921 and NSF PHY 0750049 awards.

Table 2-1: Various statistical parameters of microchannels in PDMS chips cast from silicon wafers spin-coated with 25, 160, and 311 µm thick layers of SU8 and exposed to UV-light from the LED source through the test photomask. The statistics are for channels cast from 25 regions of a wafer, corresponding to different copies of the test pattern in the 5×5 array on the photomask. The exposure times were 3, 4, and 6 min for 25, 160, and 311 µm thick layers of SU8, respectively. The values in the last six columns are normalized to the mean channel depths. Table b is a continuation of Table a.

a

depth, µm		**channel width averaged over depth, µm**				
mean	SD	mask	min	mean	max	SD
25	1.1	23	23	26	28	1.4
160	28	82	87	92	95	1.8
311	11	82	92	96	102	2.4

b

peak-to-peak variation of width, µm			**SD of width, µm**			**peak-to-peak variation of width, %**			**CV of width, %**		
min	mean	max	min	mean	max	min	mean	max	min	mean	max
1.9	3.4	8.0	0.4	0.7	1.1	7.7	13.6	32	1.4	2.9	4.5
2.6	5.8	12.8	0.7	1.4	3.1	1.6	3.7	8.0	0.4	0.9	1.9
4.5	8.1	14.0	1.2	2.2	4.3	1.4	2.6	4.5	0.4	0.7	1.4

2.2: Analysis of data

The LED UV-light source was primarily designed for contact lithography of SU8 on silicon wafers to make master molds intended for casting microfluidic devices in PDMS. The main objectives were that the profiles of the PDMS microchannels be near-rectangular and that identical features on a photomask produce channels with identical profiles over the entire target area of 90×90 mm for a broad range of microchannel depths. Therefore, to test the performance of the LED light source, we used a photomask with a 5×5 array of 18 mm squares with identical test patterns, each having four clusters of arrays of transparent strips. Each cluster had five arrays with four strips each: 23 µm wide with 17 µm separations, 41 µm wide with 39 µm separations, 82 µm wide with 78 µm separations, 160 µm wide strips 80 µm separations, four 163 µm wide with 157 µm separations (Fig. 2-3a). The relatively broad range of the strip widths made it possible to obtain features of high aspect ratio with SU8 coatings with a broad range of thicknesses using a single photomask.

To examine the cross-sections of the microchannels, the PDMS casts were cut into 25 separate chips (18 mm squares), corresponding to the 5×5 array of test patterns on the photomask. Each 18 mm square chip was then cut into 4 small chips, one for each cluster of strips in each 18 mm square on the photomask (with a different exposure time for each small

chip). To examine cross-sections of microchannels in a given small chip, the chip was carefully sliced with a razor blade in the direction across the microchannels (red rectangle in Fig. 2-3a), and the slice was photographed under a darkfield microscope. Each dark field micrograph was preprocessed using ImageJ software (NIH). First, a micrograph was rotated to ensure that the edge of the chip was horizontal. Second, a threshold was applied to convert the micrograph into a binary image, with the PDMS walls becoming white pixels and the rest becoming black pixels.

Next, the micrograph was processed using a homemade code in MATLAB (2012a, Mathworks, Natick, MA). The code displays a micrograph with channel cross-sections, allowing the user to select a rectangular region of interest (ROI) around a microchannel. The user selects the ROI such that the channel is completely contained in the rectangle, and the top and bottom of the channel match the top and bottom edges of the rectangle. The code then measures the width of the channel at each horizontal row of pixels within the ROI by counting the number of black pixels that the row contains. The code returns a list of widths vs. positions along the depth. The code also returns the depth of the channel calculated from the height of the ROI. The corners of the PDMS microchannels in the micrographs were slightly rounded both at the top (at chip surface) and the bottom. Therefore, to obtain reliable values for the channel width, it was necessary to exclude the data from several pixel rows

at the top and bottom of each microchannel. For the 160 and 311 μm deep microchannels, 15 pixels (~9.6 μm) were excluded from the analysis on either end. For the 25 μm microchannels, 5 pixels (~1.6 μm) were excluded on either end.

The main source of variability between SU8 ridges produced by the exposure through transparent strips of the same width (and between cross-sections of microchannels, which were replicas of these ridges) was expected to be the variations of the UV illumination on length scales >25 mm. The length of 25 mm is one half of the distance between LEDs in the array. It is also the distance from the center of the light spot of a single LED, at which the intensity of light drops by ~20% (Fig. 2-6). Whereas the 18 mm distance between the identical patterns on the photomask was comparable with this length, the distance between microchannels produced by identical transparent strips in an array of four on the photomask was much smaller (<1 mm). Therefore, the quality of the UV illumination was examined by choosing a single microchannel from each 18 mm square of the 5×5 array, carefully measuring cross-section of the microchannel, and comparing cross-sections of the 25 microchannels. The darkfield micrographs of the cross-channel slices of the PDMS chips (Fig. 2-3c, 2-10, 2-11, and 2-12) typically had multiple bright spots, corresponding to light scattering centers created by the cutting of PDMS. Therefore, the main factor in the selection of a single channel from an array of four (produced

by near-even UV-illumination through identical transparent strips; Fig. 2-3b, 2-10, 2-11, and 2-12) was the smallest number of bright spots near the channel boundaries.

The cross-section of each channel was reduced to 5 numbers: channel depth, average width, SD of the width, and maximum and minimum of the width. These numbers are plotted in Fig. 2-4, 2-11, and 2-12. To quantify the variations of the average width between different channels, the minimal and the maximal average channel width amongst the 25 channels were found, and the mean and SD of the average widths of the 25 channels were calculated (Table 1-1a, columns 4 – 7). To quantify the variability of profiles between different channels, the peak-to-peak and SD of variation of widths vs. depth of individual channels were compared, and the minimal, maximal and average values of these parameters were calculated (Table 1b, columns 1 – 6). Those numbers were then normalized to the average depth of respective channels (Table 1b, columns 7 – 12).

As stated above, the UV-illumination had a high uniformity on small scales (<1 mm). Therefore, possible non-uniformity of the channel profiles within the arrays of four would be due to factors other than non-uniformity of illumination: imperfections in the SU8 resist, photomask, casting of PDMS, the cutting process, the darkfield micrography, and digital processing of the micrograph. To evaluate the contribution of these imperfections, we analyzed profiles of all channels in the clusters of four in

Fig. 2-3b. (Those microchannels were cast from the 311 μm tall SU8 relief exposed for 6 min through 82 μm wide transparent strips with 78 μm separations in the representative regions 1, 2, 3, 7, 8, and 13 of the 5×5 test pattern; cf. Fig. 2-3b) As before, the cross-section of each channel was reduced to 5 numbers: channel depth, average width, SD of the width, and maximum and minimum of the widths (Fig. 2-9). The data indicated that, as expected, the variability between channels from the same array was smaller than the variability between channels in arrays from different test areas. However, the two levels of variability were comparable and were close to the resolution of our measurement technique (which was limited by the aforementioned technical factors).

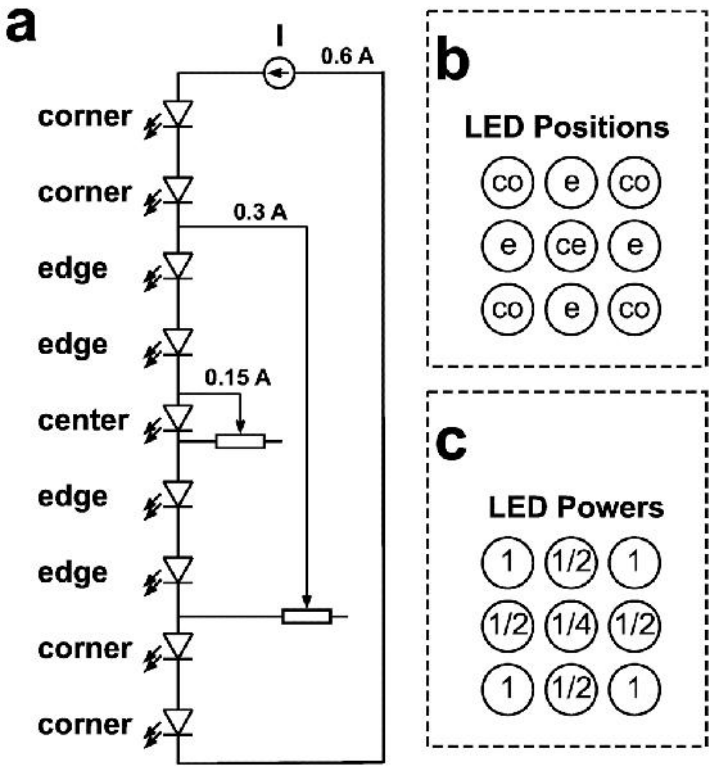

Figure 2-5: LED intensity control scheme. (a) Circuit diagram with the current source, two potentiometers, and the 9 LEDs labeled as corner, edge, or center, according to their positions in the 3×3 array. (b) Schematic diagram defining the positions of the LEDs in the array, where "co" stands for corner, "ce" stands for center, and "e" stands for edge. (c) Schematic diagram showing the approximate relative luminous powers of the LEDs in the array, with the relative power of 1 corresponding to 0.6 A of current through the LED.

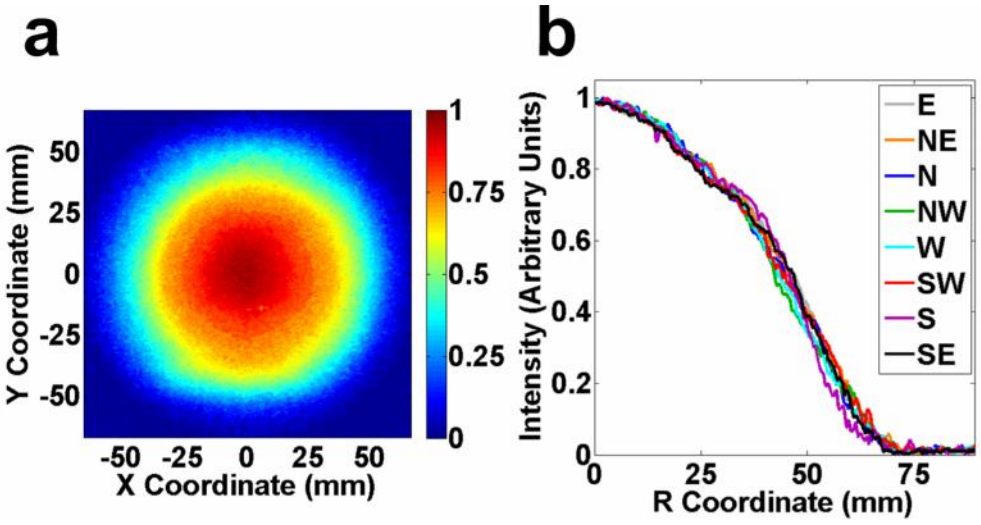

Figure 2-6: The illumination field of a single LED in the array from a photograph. (a) A color-coded map of the light intensity from a photographic image of white paper illuminated by a single LED of the array. (b) Distribution of the illumination intensity in the photograph in panel a along lines extending radially from the center along 8 different directions, with E corresponding to the direction to the left (east), N – to the direction to the top (north), etc. Each plot is an average over a width of ~3.4 mm (16 pixels).

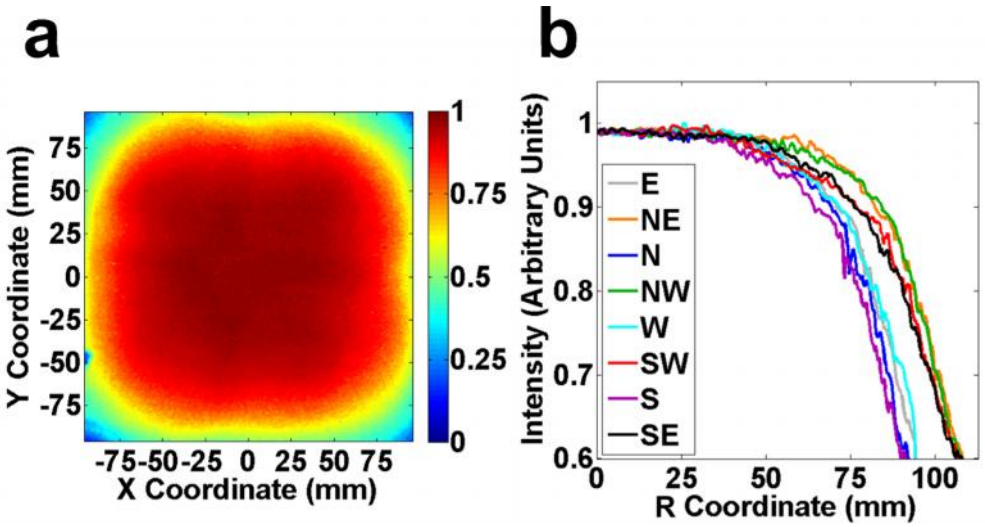

Figure 2-7: The illumination field of the 3×3 LED array from a photograph. (a) A color-coded map of the light intensity from a photographic image of white paper illuminated by the LED array. (b) Distribution of the illumination intensity in the photograph in panel a along lines extending radially from the center along 8 different directions, with E corresponding to the direction to the left (east), N – to the direction to the top (north), etc. Each plot is an average over a width of 3.6 mm (16 pixels).

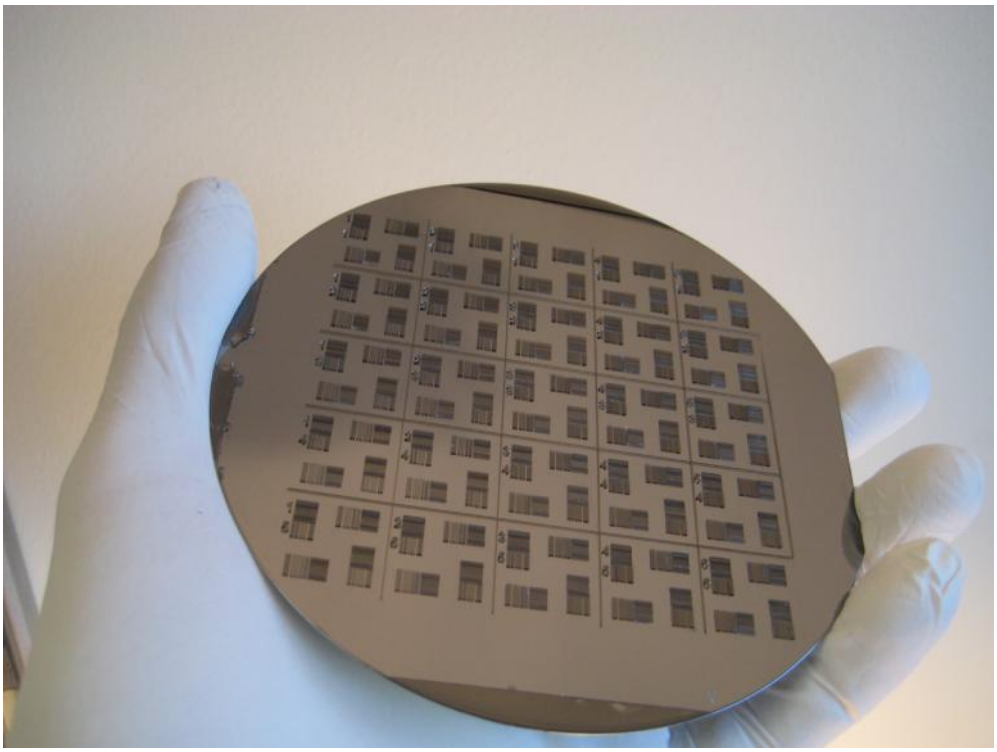

Figure 2-8: A master mold obtained by the exposure of a 5 inch silicon wafer coated with a 300 μm layer of SU8 by UV-light from the LED light source through a photomask with a 5×5 array of identical test patterns. The patterns are numbered by their columns and rows. Each test pattern has 4 clusters of SU8 ridges. The clusters in the top left, bottom left, bottom right, and top right corners of each test pattern were produced by 4, 6, 8, and 10 min of UV exposure, respectively.

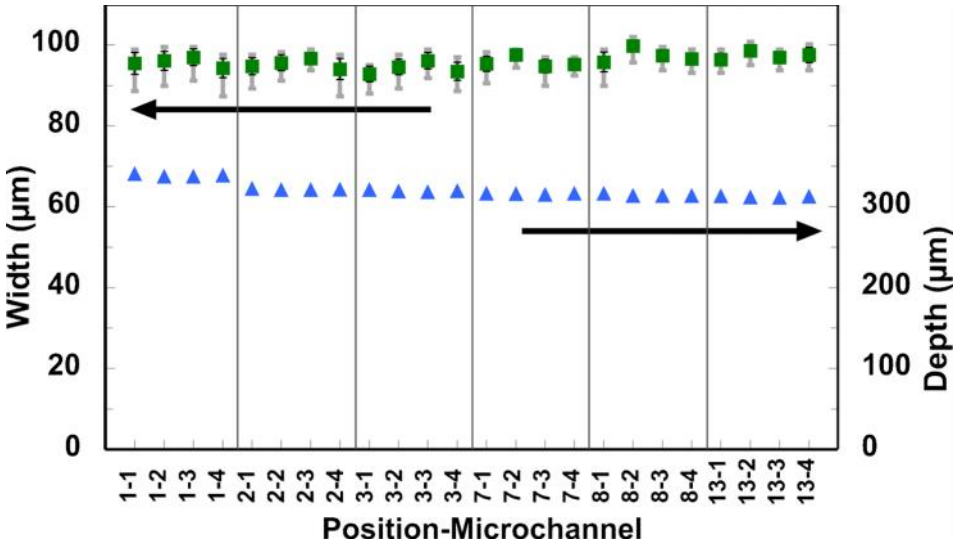

Figure 2-9: The width of a microchannel averaged over its depth (green squares) and microchannel depth (blue triangles) for each of the 4 microchannels at 6 representative positions (cf. Fig. 2-3b) within the 5×5 test pattern array (positions 1, 2, 3, 7, 8, and 13). All microchannels are replicas of ridges produced by a 6 min UV exposure of a 311 µm thick (on average) layer of SU8 through 82 µm transparent strips with 82 µm separations. Black error bars show standard deviations of the widths; grey error bars show ranges of widths measured.

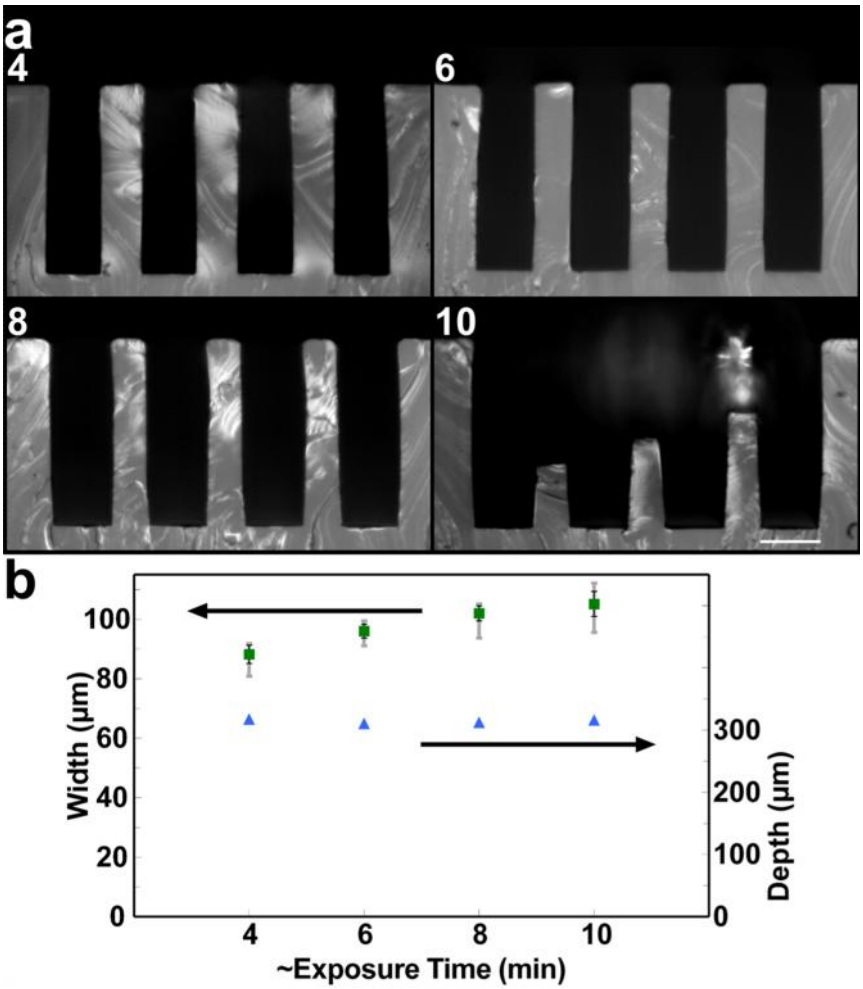

Figure 2-10: Microchannels in PDMS chips that are replicas of SU8 ridges produced with different times of exposure of a 311 μm layer (average thickness) of SU8 to UV light from the LED source. (a) Micrographs of cross-sections of microchannels that are replicas of SU8 ridges produced with 4, 6, 8, and 10 min exposures to UV through 82 μm transparent strips with 78 μm separations in the central region of the wafer (#13 in Fig. 2-3b). The micrographs are taken with a 10x objective under darkfield illumination. Scale bar 100 μm. (b) The microchannel width averaged over its depth (green squares) and the microchannel depth (blue triangles) for the microchannel cross-sections in panel a. (For the 10 min exposure only a 173 μm tall intact portion of the microchannel on the right was used for the measurements.) Black error bars show standard deviations of the widths; grey error bars show ranges of widths measured.

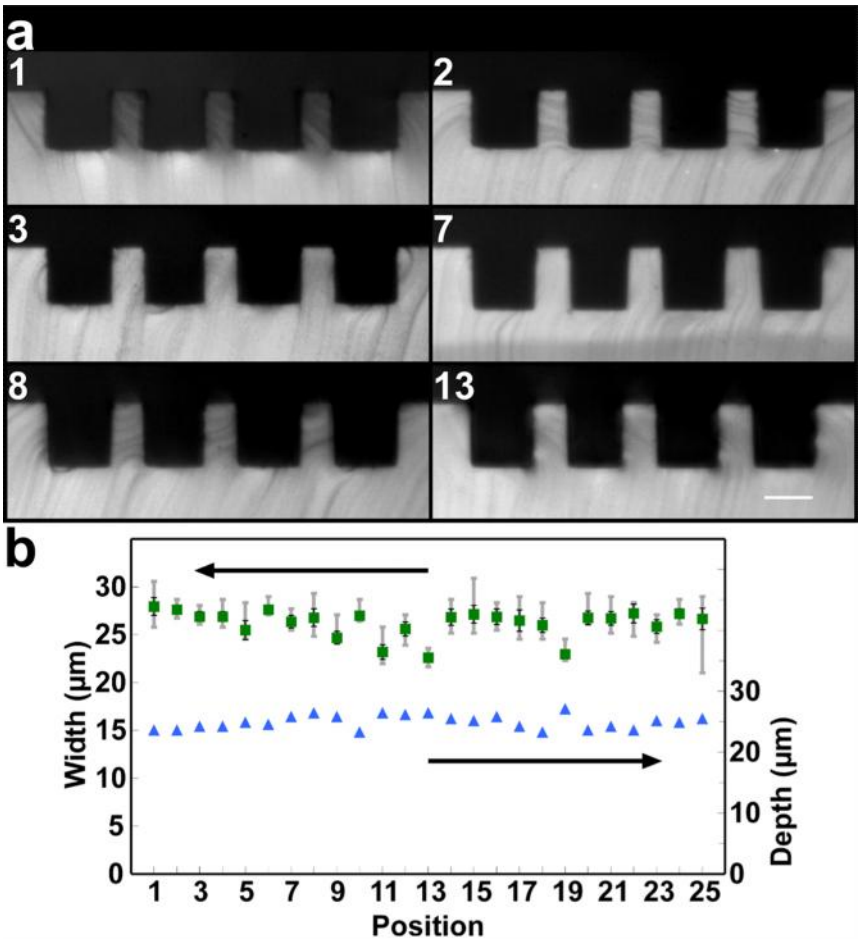

Figure 2-11: PDMS chips with microchannels that are replicas of SU8 ridges produced by a 3 min exposure of a 25 µm layer of SU8 (average thickness) to UV-light through 23 µm wide transparent strips with 17 µm separations on the test photomask. (a) Micrographs of cross-sections of microchannels in PDMS chips cast from 6 representative regions of the wafer with different locations within the 5×5 test pattern array, as indicated by numbers, corresponding to the highlighted squares in Fig. **2-3**b. The micrographs are taken with a 10x objective under darkfield illumination. Scale bar 25 µm. (b) The width of a microchannel averaged over its depth (green squares) and microchannel depth (blue triangles) for all 25 position within the 5×5 test pattern array (cf. Fig. **2-3**b). Black error bars show standard deviations of the widths; grey error bars show ranges of widths measured.

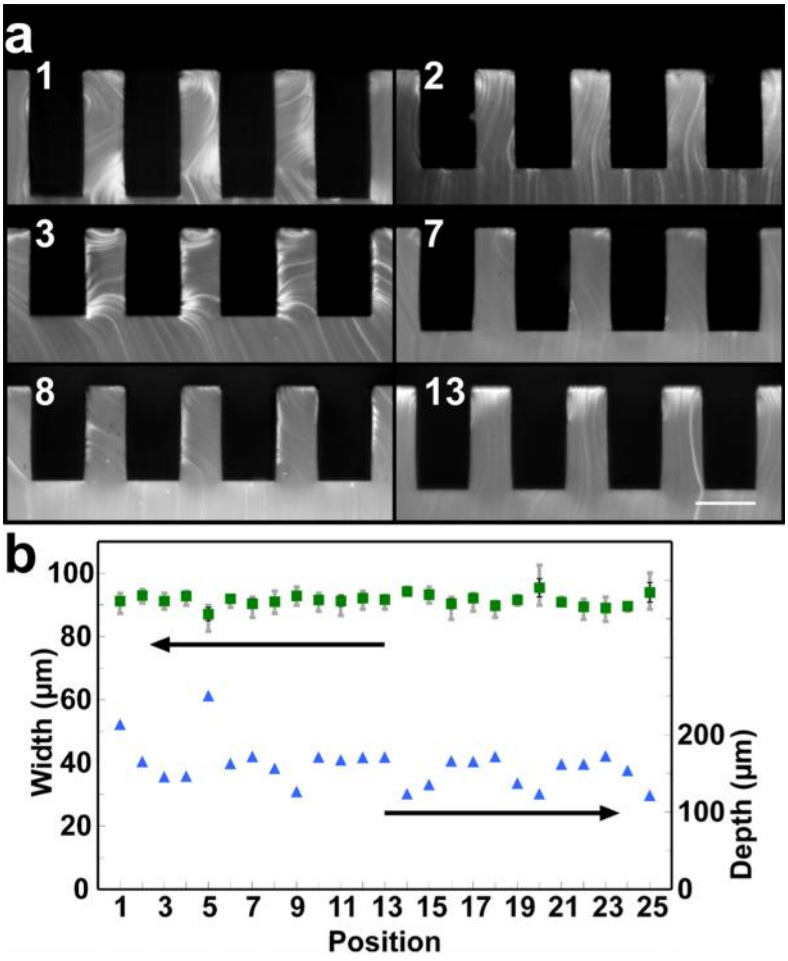

Figure 2-12: PDMS chips with microchannels that are replicas of SU8 ridges produced by a 4 min exposure of a 160 μm layer of SU8 (average thickness) to UV-light through 82 μm wide transparent strips with 78 μm separations on the test photomask. (a) Micrographs of cross-sections of microchannels in PDMS chips cast from 6 representative regions of the wafer with different locations within the 5×5 test pattern array, as indicated by numbers, corresponding to the highlighted squares in Fig. **2-3**b. The micrographs are taken with a 10x objective under darkfield illumination. Scale bar 100 μm. (b) The width of a microchannel averaged over its depth (green squares) and microchannel depth (blue triangles) for all 25 position within the 5×5 test pattern array (cf. Fig. **2-3**b). Black error bars show standard deviations of the widths; grey error bars show ranges of widths measured.

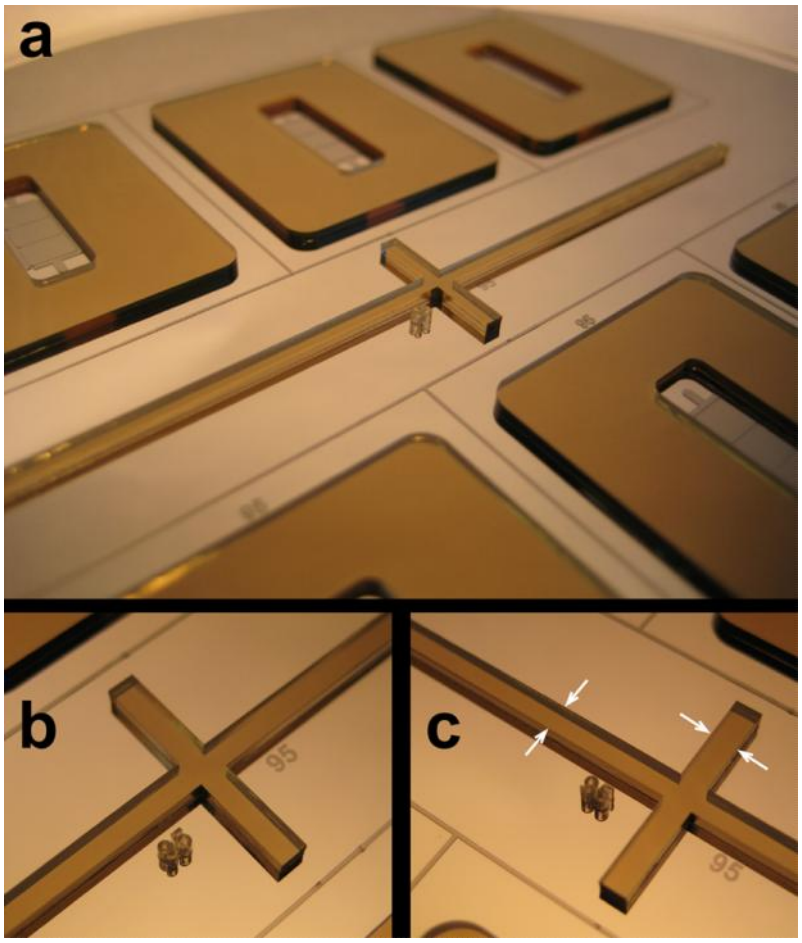

Figure 2-13: Photographs of a wafer with ~1 mm tall SU8 relief produced using the LED UV-light source. The wafer also has ~40 μm tall SU8 features. Panels b and c are photographs of fragments of the relief in panel a taken from different angles with greater magnifications. Distances between the juxtaposed white arrows are 1.5 mm.

Chapter 2.1, in full, has been submitted for publication as “A low-cost low-maintenance ultraviolet lithography light source based on light-emitting diodes”, Erickstad, Michael; Gutierrez, Edgar; and Groisman, Alex. The dissertation author is first author and a leading contributor to this paper.

Chapter 2.2, in full, has been submitted for publication as “The supplementary information to: A low-cost low-maintenance ultraviolet lithography light source based on light-emitting diodes”, Erickstad, Michael; Gutierrez, Edgar; and Groisman, Alex. The dissertation author is first author and a leading contributor to this paper.

Chapter 3: A Microfluidic System for Studying The Behavior of Zebrafish under Acute Hypoxia

Abstract

Oxygen is essential for metabolism of vertebrate animals and is a vital component of their natural habitats. Hypoxic conditions in tissue, when oxygen levels are lower than normal, change a variety of cellular processes, and hypoxic environments can have physiological and behavioral effects on the whole animal. Larval zebrafish respond to oxygen deprivation with a characteristic set of physiological changes and motor behaviors, making them a convenient vertebrate model to study hypoxia responses. However, to date, hypoxia studies in zebrafish are limited by the existing experimental setups, which only impose hypoxia on a scale of minutes to hours. Here, we present a microfluidic system, which makes it possible to expose spatially confined unanesthetized zebrafish larvae to a broad range of hypoxic and normoxic conditions and to switch between different oxygen concentrations in the medium around the larvae on a 2 second timescale. We used the system to observe different behavioral responses of zebrafish larvae to three levels of rapidly imposed hypoxia. Larvae did not change their rate of eye saccades in response to any level of hypoxia, increased their rate of body movements in response to the strongest hypoxia, and increased their rate of pectoral fin beats in

response to all levels of hypoxia. Importantly, the behavior of the larvae changed within 15 seconds of the changes in the oxygen content of the medium. The proposed experimental system can be used to study the behavior of zebrafish larvae exposed to other water-dissolved gasses or to different temporal patterns of oxygen concentration. The system can also be adapted for use with other aquatic animals.

Introduction

The metabolism of most vertebrate cells involves oxygen as the oxidizing agent, making the oxygen concentration, $[O_2]$, an important factor of their environment. Changes in $[O_2]$, especially hypoxic conditions ($[O_2]$ lower than normal), lead to changes in a variety of cellular processes[1], including neural activity[2, 3], angiogenesis[4], tumorigenesis[4], and cell death[2, 3, 5]. In a human body, normal physiological levels of $[O_2]$ (normoxic conditions) are tissue-dependent and are usually considered to be in a range of $[O_2]$ = 2-9%[4], where $[O_2] \approx 20.8\%$ corresponds an aqueous medium at equilibrium with atmospheric air at standard temperature and pressure (normoxic atmosphere with pO_2 of 21 kPa). Whereas normoxic $[O_2]$ in a human body is substantially lower than 20.8%, reduced pO_2 in the atmosphere (environmental hypoxia) leads to reduced $[O_2]$ in tissues[6]. Significant reduction of pO_2 in the atmosphere, such as $pO_2 < 16$ kPa at altitudes >2 km, usually requires acclimation, and the hypoxic atmosphere

with pO_2 < 10 kPa at altitudes >5.5 km makes these altitudes generally uninhabitable for humans[6]. In aquatic environments, dissolved oxygen content usually decreases with the depth and temperature. Aquatic hypoxia is often defined as <30% aeration ([O_2] < 6% or <2.5 mg/L)[7]. Depletion of O_2 is a common cause of fish kills, and many species of fish have various hypoxia avoidance behaviors.[7] While progress has been made in understanding effects of hypoxia on molecular and cellular levels, it has proven to be difficult to connect them with behavioral responses to environmental hypoxia in animals[8-10].

Zebrafish is widely used as a vertebrate model organism to study the development, genetics, circulation, and disease[11-15], as well as behavioral and circuit neuroscience[16-18]. Zebrafish can tolerate reduced [O_2], and prolonged exposure to hypoxia at early larval stages has even been reported to benefit zebrafish by increasing their survival at later stages[19]. Nonetheless, in response to oxygen deprivation, zebrafish undergo various physiological changes and develop certain compensatory and avoidance behaviors [19-21]. Embryonic zebrafish respond to hypoxia by entering a state of suspended animation and reducing the heart rate and cell-cycle progression, until normoxia is restored.[21] Larval zebrafish respond to hypoxia with a characteristic set of motor behaviors: increased pectoral fin and body movements, gill and operculum movement, and buccal pumping.[22] The robust responses of larval zebrafish to oxygen

deprivation make it a good model system for studies on the effects of hypoxia on vertebrate behavior and neural activity.

Studies of zebrafish in hypoxic media have used commercially available environmental chambers[20, 21] and perfusion chambers, which were bubbled with N_2 or N_2/air mixtures to impose hypoxia[19, 22-24]. Whereas these experimental setups enabled maintaining desired levels of O_2 in the medium, switching from normoxia and hypoxia took many minutes [21-24] . These long transition times would make it difficult to evaluate the time of response of zebrafish to hypoxia and clearly distinguish between responses to acute and prolonged hypoxia. In addition, the quantification of specific motor responses to hypoxia, e.g., pectoral fin beats, often requires imaging at a relatively high resolution, which is generally complicated, when zebrafish are freely swimming.

Microfluidic and microwell devices have been used in experiments on zebrafish embryos and larvae for several years now. Those included experiments on development[25-28], toxicology and drug screening assays [25-30], and measurement of the rate of respiration of individual embryos[31]. Microfluidics has also been used to partially immobilize and image zebrafish embryos. [27, 28] A recently introduced microfluidic device facilitates drug treatment of anesthetized zebrafish larvae and enables their precise positioning for improved imaging[32]. Microfluidic chips made of polydimethylsiloxane (PDMS) have a high O_2-permeability, making it

possible to control [33-35] and rapidly change[35] [O_2] in microchannels, generate O_2 gradients [36, 37], and culture bacteria [35, 38] and eukaryotic cells[38, 39] at different [O_2]. Microfluidic devices have also been used to study the responses of the nematode worm *C. elegans* to spatial gradients and temporal changes of [O_2][37, 40].

In this paper, we describe an experimental system with a computer-controlled gas mixer and a PDMS microfluidic chip that makes it possible to spatially confine and partially immobilize an unanesthetized zebrafish larva in a dedicated imaging region and change the O_2 content of the medium around the larva on an ~2 sec time scale. We used the system to study three types of motor responses of 7 days post fertilization (dpf) larvae to three different levels of acute hypoxia. We detected a significant motor response to a relatively weak hypoxia with [O_2] = 6.6% (~2.8 mg/L) and found the larvae to respond to changes in environmental [O_2] within <15 sec.

3.1: Experimental

Microfluidic device

The microfluidic device is made of a microfabricated PDMS chip sealed against a #2 microscope cover glass. The PDMS chip is cast using a silicon wafer with a lithographically fabricated three-step SU8 micro-relief (heights of 120, 265, and 550 μm) as the master mold. The microchannel

network of the device has three main elements: a fish channel, which is connected to a dedicated fish-loading inlet, and two mirror-symmetric gas exchangers, each with its own liquid-medium inlet (medium in 1 and 2 in Fig.1) and a single liquid-filled serpentine channel. The device has a single dedicated liquid-medium outlet (medium out in Fig. 3-1). The fish channel is ~550 μm deep and includes a ~3.5 mm long, ~700 μm wide imaging region, which is designed to match the dimensions of 5-7 days past fertilization (dpf) zebrafish larvae. The fish channel tapers down from the fish-loading inlet towards the imaging region, facilitating the loading of zebrafish larvae. The imaging region is connected to the outlet through two parallel ~200 μm wide channels, forming a barrier that is open for flow, but impassable for the fish (Fig. 3-1). The movements of a fish in the imaging region are limited by the PDMS walls surrounding it from three sides (the two side walls and the barrier) and by the hydrodynamic drag, which is caused by the flow towards the outlet and pushes the fish against the barrier.

After a zebrafish larva is loaded to the imaging region, the fish-loading inlet is blocked, and the flow of liquid medium through the device is mainly from the medium inlet of one of the gas exchangers through its serpentine channel and the imaging region towards the outlet. This flow through the gas exchanger continuously supplies an aqueous medium with controlled [O_2] to the imaging region and also provides hydrodynamic drag

to partially immobilize the zebrafish larva. (The flow through the serpentine channel of the other gas exchanger is much weaker and is directed towards its inlet; see below.)

The gas exchangers are based on a design from our previous work.[41] The liquid-filled serpentine channel in each gas exchanger is ~120 μm deep and ~120 μm wide, has a total length of 113 mm, and is flanked on both sides by gas channels ventilated with a mixture of N_2 and air with controlled [O_2] (or with pure N_2). The gas channels are ~265 μm deep and ~250 μm wide, and the PDMS walls between the liquid-filled channel and the gas channels are ~115 μm wide on either side (Fig. 3-5). Due to the high oxygen permeability of the PDMS side walls, as the medium advances along the serpentine channel, its O_2 content gradually equilibrates with that of the N_2/air mixture ventilated through the two flanking gas channels. The two gas exchangers have different [O_2] in their gas channels, and a change of [O_2] in the medium around the zebrafish larva is achieved by changing which gas exchanger supplies medium to the imaging region.

To model the operation of a gas exchanger, we performed numerical simulations in Comsol, assuming O_2 solubility in PDMS at 0.25 (as a fraction of [O_2] in the gas phase, corresponding to 10.4 mM/atm at room temperature), O_2 solubility in water at 1.3 mM/atm, O_2 diffusivity in PDMS, D_p = 1000 μm^2/s, and O_2 diffusivity in water, D_w = 2000 μm^2/s. The

simulations indicated that, with pure N_2 in the gas channels ($[O_2] = 0$) and air outside the device ($[O_2] = 20.8\%$), the average $[O_2]$ in an aqueous solution in the serpentine channel reaches ~0.15% in a saturated state, when there is no flow (Fig. 3-5). (Here and below $[O_2]$ in the gas phase is the fraction of O_2 in the gas mixture such that when an aqueous solution is in equilibrium with a gas mixture at 1 atm, they have the same values of $[O_2]$.) The value of $[O_2]$ in the saturated state is greater than zero because of the incomplete occlusion of the liquid-filled channel by the gas channels, leading to some diffusive flux of O_2 from the atmosphere towards the liquid-filled channel. For a hypoxic gas mixture with $[O_2] > 0$ in the gas channel, the difference between the saturated level of $[O_2]$ in an aqueous solution and $[O_2]$ in the gas mixture is smaller than 0.15% and can be approximately found as $\Delta[O_2] = 0.15 \cdot (1 - [O_2]/20.8\%)$. The numerical simulations also indicated that when an aqueous solution with $[O_2]$ different from that in the gas mixture is fed into a serpentine channel, the equilibration of $[O_2]$ in the solution with $[O_2]$ in the gas mixture occurs as an exponential decay with a characteristic time of 0.87 sec in the Lagrangian reference frame moving with the average velocity of the solution (Fig. 3-5). We note that, whereas $[O_2]$ in an initially aerated solution decreases as the solution advances along the serpentine channel of an exchanger ventilated with a hypoxic gas mixture, neither $[O_2]$ in the

solution at a given position along the channel nor the O_2 content of the PDMS at a given position near the channel changes in time.

In addition, our numerical simulations indicated that when the O_2 content of the gas channels of an exchanger is abruptly changed, it takes a characteristic time of ~13 sec for [O_2] in the liquid-filled channel (with no flow in it) to reach a new steady state. This transition time is substantially longer than the equilibration time of 0.87 sec discussed above, because after the O_2 content of the gas channels is switched, not only [O_2] in the liquid-filled channel but also the O_2 content of PDMS have to change, before a new state of equilibrium is reached. The PDMS around the channels of the gas exchanger is a substantially larger reservoir of O_2 than the liquid-filled channel. Specifically, according to our simulations, when the gas mixture is switched from [O_2] = 20.8% to 0, the amount of O_2 to be evacuated from the PDMS is >100 times greater than that from the serpentine channel filled with an aqueous solution. Therefore, to achieve rapid switching of [O_2] in the imaging region, it was essential to have two gas exchangers, each with the O_2 content of PDMS around its channels mainly set by [O_2] of a continuously supplied gas mixture and, hence, changing relatively little as a result of the switching (Fig. 3-5).

The inlets of the liquid-filled channels in the two gas exchanges are connected to reservoirs (modified 4 oz plastic jars) with the same aqueous medium suitable for zebrafish larvae. The headspaces of the reservoirs

feeding the medium inlets 1 and 2 are connected to the common ports of two identical 3-way solenoid valves, A and B, respectively (Fig. 3-6). The normally closed port of valve A and the normally open port of valve B are connected to a source of compressed air with a pressure of 11 kPa. The normally open port of valve A and the normally closed port of valve B are open to the atmosphere. Both solenoid valves are powered through the same line, such that at any given moment, one reservoir is pressurized and the other reservoir is vented to the atmosphere (Fig. 3-6). Consequently, the medium inlets of the two gas exchangers are pressurized one at a time. The pressurized medium inlet and the gas exchanger it belongs to are called active, and the non-pressurized medium inlet and exchanger are called passive. When the power supplied to the two solenoid valves is switched, the roles of the two exchangers (and inlets) switch as well (passive becomes active and vice versa), and $[O_2]$ in the medium fed to the imaging region changes.

The levels of the medium in the two inlet reservoirs as well as in the reservoir connected to the outlet are all set to be the same, resulting in identical pressures at the outlet and at the passive inlet. The pressure at the T-junction connecting the liquid-filled channels of the two exchangers (Fig. 3-1) is somewhat higher than the pressure at the passive inlet, causing a backflow through the liquid-filled channel of the passive exchanger towards its inlet. The mean rate of this backflow (as measured

by tracking fluorescent particles in the serpentine channels of the active and passive exchangers) is only ~5% of the rate of the flow from the serpentine channel of the active exchanger towards the outlet because of a high hydrodynamic resistance of the serpentine channel (as compared to the hydrodynamic resistance from the T-junction to the outlet). The backflow ensures that the stream of the medium entering the imaging region is entirely from the active exchanger.

The two different N_2/air mixtures are continuously fed to the gas exchangers through the gas inlets A and B (with all gas outlets open to the atmosphere). The two mixtures are generated using a computer-controlled two-channel gas mixer, whose design is described in detail elsewhere[36]. Briefly, each channel of the mixer has a dedicated miniature 3-way solenoid valve with a fluidic resistor (capillary) connected to its common port downstream from the valve and a mixer tubing segment connected downstream from the resistor. The normally closed and normally open ports of the valve are connected to sources of compressed air and compressed N_2 with the same pressure. The valve switches on and off periodically, and the proportion of air in the mixture is controlled by the duty cycle of the switching, making it possible to create gas mixtures with $[O_2]$ from 0 to 20.8%.

The output of each channel of the mixer is divided to supply >0.2 mL/s to gas inlet A or B and >0.1 mL/s to an assembly of two miniature

solenoid valves (Fig. 3-1 and Fig. 3-6). The assembly has two outlets, one vented to the atmosphere and one connected to gas inlet C of the device. The valve assembly operates in such a way that there is a steady flow of gas from both channels of the mixer towards it, but the gas mixture fed to gas inlet C (gas in C in Fig. 3-1) is always identical to the gas mixture fed to the active gas exchanger. Gas inlet C is connected to a gas channel skirting around the fish channel. Unlike gas channels A and B, the content of gas channel C switches every time the passive and active exchangers switch their roles. Gas channel C facilitates the change in the O_2 content of the channel walls around the imaging region after switching and also shields the imaging region from outside gas contamination on longer time scales.

All of the solenoid valves are driven by a computer-controlled relay board using a home-made, standalone Matlab code as an interface (Fig. 3-6). All experiments involving larvae are conducted with E3 embryo media for zebrafish (Cold Spring Harbor Protocols, 2011). An oxygen-sensitive fluorescent dye, Ruthenium tris(2,2'-dipyridyl) dichloride hexahydrate (RTDP) was purchased from Sigma-Aldrich and dissolved at ~50 ppm (by mass) in Dulbecco's phosphate buffered saline (Gibco). The fluorescence microscopy setup used to measure the intensity of fluorescence of RTDP solutions in microchannels is described in detail elsewhere[35, 36]. The zebrafish in the imaging region were imaged with a 4×

objective and a Sony 900 XCD-SX900 digital camera, with a 1.8×1.35 mm field of view of the video microscopy setup.

Animal Specimens

Zebrafish embryos were obtained from natural spawnings of AB wild types. All experiments have been approved by the Institutional Animal Care and Use Committee of The Salk Institute for Biological Studies (Animal Use Protocol: 09-066).

3.2: Results

Measurements of oxygen concentration

The fluorescence of RTDP is quenched in the presence of oxygen in a manner modeled by the Stern-Volmer equation[42]:

$$I_0 / I = 1 + K_q[\mathrm{O}_2] \qquad (3\text{-}1)$$

where K_q is the quenching coefficient of RTDP, I_0 is the intensity of fluorescence of the dye at anoxic conditions, and I is the fluorescence intensity at given [O_2]. The value of K_q is temperature-dependent and is calculated using the equation $K_q = (I_0 / I_{air} - 1)/0.208$ by measuring fluorescence intensities when the solution is saturated with air ([O_2] = 20.8%), I_{air}, and with pure N_2, I_0.

To find the value of K_q, we first measured the intensity of fluorescence of the RTDP solution near the end of a serpentine channel of a gas exchanger, which had its gas channel ventilated with air, and took it as I_{air}. Next, the gas fed to the gas channel was changed to N_2, and the fluorescence in the serpentine channel was measured as a function of time. (Both gases fed to the device were bubbled through water in a sealed bottle to saturate them with water vapor, thus reducing the evaporation from the serpentine channel.) The fluorescence increased with a characteristic time scale of ~17 sec (~40 sec for 9/10 of the transition; data not shown), in reasonably good agreement with our numerical simulations. After ~2 min, when the fluorescence reached a steady state, indicating a near-complete exchange of the O_2 content of the PDMS around the channels of the gas exchanger, the flow through the serpentine channel was stopped, and the fluorescence was measured as a function of time again. The stopping of the flow led to a more complete equilibration of the O_2 content in the serpentine channel with that in the gas channel, resulting in a further reduction in $[O_2]$ in the RTDP solution and further increase in its fluorescence. The new steady state fluorescence intensity, as measured at ~5 sec after the flow was stopped, was taken as a tentative value of I_0. (There was an additional very slow increase in the fluorescence with time which was most likely due to residual evaporation of water from the channel.) The value of K_q calculated from I_{air} and I_0 was 2.27. This value

was then corrected for the fact that, according to our numerical simulations, the steady state fluorescence intensity under pure N_2 corresponded to $[O_2]$ of 0.15% rather than zero, resulting in K_q = 2.30, in good agreement with previous reports[35, 36].

The microfluidic device did not allow enforcing O_2-free conditions in the imaging region of the fish channel (due to the diffusive influx of the atmospheric O_2 through its roof). Therefore, the evaluation of $[O_2]$ from the measured intensity of fluorescence in the imaging region, I, was based on the calculated value of K_q and on the intensity of fluorescence of the RTDP solution saturated with air, I_{air}, as the reference point,

$$[O_2] = \frac{(I_0 / I - 1)}{K_q} = \frac{(1 + 0.208 K_q) I_{air} / I - 1}{K_q} \qquad (3\text{-}2)$$

The value of I in the imaging region was measured as a function of time under the same conditions as in our experiments on zebrafish larvae (see below). Specifically, one gas exchanger was fed with air and the other was fed with a hypoxic air/N_2 mixture. The exchangers were switched with a 100 sec period, such that the active exchanger was the aerated exchanger for 50 sec and then the hypoxic exchanger for 50 sec (Fig. 3-2). The mean flow velocity in the liquid-filled serpentine channel of an active exchanger was estimated as v = 52 mm/s by measuring the maximal flow velocity with fluorescent tracer particles and applying the equations for a laminar flow in a square (120×120 μm) channel. Given the channel length L = 113

mm, this flow velocity corresponded to a mean residence time $t = L / v = 2.2$ sec in the channel. The volumetric flow rate through the outlet was measured at Q = 0.74 µL/s. Given the imaging region volume of 1.3 µL, the medium in the imaging region was expected to be exchanged within 1.8 sec.

The measurements of fluorescence of RTDP in the imaging region were done near its downstream end at the channel mid-plane (~275 µm from the bottom) using a 20x/0.75 objective, with data points taken once a second. First, we used pure N_2 as the hypoxic gas mixture. After the active gas exchanger was switched from the one ventilated with air to the one ventilated with N_2, [O_2] in the imaging region dropped from 20.8% to ~1.8% (Fig. 3-2). The transition was 9/10 complete within ~2 sec, which was consistent with the estimated medium exchange time of 1.8 sec. For the residence time of 2.2 sec, the value $\ln(20.8/1.8) = 2.44$ corresponds to 0.90 sec as a characteristic time of equilibration of [O_2] in serpentine channel with [O_2] in the gas channel. This equilibration time is very close to the value of 0.87 sec obtained from our numerical simulations for the equilibration time in the Lagrangian reference frame moving with the mean flow velocity of liquid in the serpentine channel.

Notably, before [O_2] leveled off at 1.8%, it transiently dipped to ~1%, which was most likely because before the switching, when the exchanger ventilated with N_2 was passive, the medium in its liquid-filled channel was

flowing (backwards) at ~20 times lower speed. This low flow speed led to ~20 times increased residence time and substantially reduced [O_2] (expected to be close to the saturated level of ~0.15%). The test was repeated with hypoxic air/N_2 mixtures with [O_2] = 2 and 5%, producing similar results. The transition time from [O_2] = 20.8% to hypoxia was the same (~2 sec), the transient dips in [O_2] were consistently observed, and the steady-state hypoxic levels of [O_2] in the imaging region were ~1.7 and 1.6% above [O_2] in the hypoxic gas mixtures, at ~3.7 and 6.6%, respectively.

Hypoxia-induced behavioral responses of zebrafish

In the behavioral experiments with zebrafish, unanesthetized 7 dpf larvae were loaded into the fish channel inlet (head first) using a plastic pipette. After a larva reached the barrier at the end of the imaging region, the fish channel inlet was plugged, and the animal was pushed against the barrier by the hydrodynamic drag of the flow from a gas exchanger ventilated with air. (Zebrafish larvae could be removed from and returned to the imaging region for repeated analyses of an individual larva.) An experimental trial consisted of three 50 sec exposures to a hypoxic medium with 50 sec exposures to an aerated medium in between (100 sec per cycle). The behavior of the larva during the trial and the 50 sec interval immediately before the trial was digitally recorded and analyzed.

Experiments were performed on five larvae (n = 5), with each larva exposed to at least two complete trials with $[O_2]$ = 1.8% (strong hypoxia). In addition, two larvae (n = 2) were each exposed to one complete trial with $[O_2]$ = 3.7% (medium hypoxia), and four larvae (n = 4) were each exposed to one complete trial with $[O_2]$ = 6.4% (weak hypoxia) and at least one complete control trial with air fed to both gas exchangers. Behavioral responses were manually scored by analyzing the digital recordings and quantified as mean rates within 10 sec intervals. The mean rates were then binned by the time point in the trial. Out of a total of 33 attempted trials, 24 (73%) were complete, with the other 9 trials, including 6 trials on one individual larva, ending prematurely, because the larvae (which were agitated by hypoxia) escaped from the imaging region. On average, the escapes occurred at 145 sec from the beginning of the trial. The data from all complete trials and from incomplete trials before the escape moments were pooled together by the type of the trial ($[O_2]$ during the hypoxic intervals), and average values of the 10 sec bins were calculated. The values of SEM were calculated based on the number of data points in each bin (from both complete and incomplete trials). In the complete trials (and incomplete trials prior to the larva escapes), the larvae had their heads and pectoral fins in the field of view >99% of the time.

The first behavioral response analyzed was the pectoral fin beats, a well-established compensatory behavior associated with hypoxia [22] (Fig.

3-3). As expected, the strength of the response (increased frequency of the beats) correlated with the strength of the hypoxia (Fig. 3-3 and 3-4a). Notably, however, the response was significant even when hypoxia was weak ($[O_2]$ = 6.6%). The rates of the pectoral fin beats had a tendency to increase during the entire 50 sec hypoxic segments, with no clear signs of saturation (Fig. 3-3). Importantly, for strong hypoxia, an increase in the frequency of the pectoral fin beats was significant as soon as 15 sec after $[O_2]$ in the imaging chamber was reduced (Fig. 3-3). Moreover, after the medium in the imaging region became aerated, following a 50 sec segment of strong or medium hypoxia, the pectoral fin beat rate significantly decreased within 15 sec as well. In order to detect the early response to acute hypoxia and the delay in the recovery from hypoxia-induced behavior, it was essential to be able to switch between hypoxic and aerated media sufficiently quickly (within 2 sec in our setup). For strong hypoxia, the recovery from the hypoxia-induced behavior was slower than for medium hypoxia, resulting in significantly elevated average frequency of pectoral fin beats even during the last 30 sec of the two 50 sec intervals with aerated medium in the chamber between the 50 sec exposures to hypoxia (Fig. 3-4a).

Two other behavioral responses analyzed were eye saccades and large body movements of the larvae. We found that the rate of eye saccades was not significantly influenced by hypoxia (Fig. 3-4b). In contrast, the

rate of body movements significantly increased when larvae were exposed to strong hypoxia (Fig. 3-4c). These large body movements resemble the previously reported erratic twitching movements of zebrafish exposed to a similar level of hypoxia, with $[O_2] \approx 2\%$ (0.8mg/L)[24]. However, the hypoxia-induced body movements were relatively rare events, with their frequencies much lower than the frequencies of pectoral fin beats at the same hypoxic conditions, leading to large stochastic variability.

Discussion and Conclusions

The microfluidic device used in this study was designed to meet two essential goals: controlled rapid changes of $[O_2]$ in the medium around zebrafish larvae and observation and quantification of behavioral responses of the larvae to the changes of $[O_2]$. Fast changes of $[O_2]$ in ~10 μm deep liquid-filled micro-channels have been previously achieved in a two-layer microfluidic device by switching the O_2 content in gas-ventilated channels separated from the liquid-filled channels by an ~50 μm thick layer of PDMS[35]. In that device, $[O_2]$ in the micro-channels changed quickly (on an ~1 sec scale) because of rapid diffusion of O_2 across the shallow liquid-filled channels and thin PDMS layer. However, an approach relying on a passive diffusion of O_2 would be unsuitable for imposing fast changes in $[O_2]$ around a zebrafish, which is a relatively large organism even at its larval stage. Indeed, given the larva's diameter, $L \approx 0.5$ mm, the

minimal characteristic time of O_2 exchange by diffusion in the medium around it, $t = L^2/(2D_w)$, is ~60 sec. (A reduction of [O_2] from 20.8 to 3% would then take >120 sec.) This slow O_2 exchange by diffusion also sets a physical limitation on the temporal resolution in the experimental setups where larvae are placed in an open reservoir and [O_2] in the reservoir is changed by changing the composition of the atmosphere above it[20, 21].

Therefore, to achieve a fast change of [O_2] in the medium around a zebrafish larva, it was essential to rely upon active perfusion of the imaging region by two alternate media with different [O_2]. To satisfy this minimal requirement, unlike our previous device[41], the microfluidic device used in the study had two separate gas exchangers. The equilibration of [O_2] in the liquid-filled serpentine channels of the exchangers with [O_2] in the gas channels was facilitated by a large length of the exchangers (113 mm), the presence of the gas channels on both sides of the liquid-filled channels, and the small width (115 μm) of the partitions between the gas and liquid-filled channels. The equilibration was incomplete, with [O_2] only dropping to ~1.8% when the gas channels were ventilated with N_2 (with a complete equilibration resulting in [O_2] = 0.15%, according to our numerical simulations). Nevertheless, our experiments revealed a significant behavioral response (increased rate of pectoral fin beats) of zebrafish larvae to hypoxia with [O_2] as high as 6.6% (2.8 mg/L), such that an environment with [O_2] = 1.8% (nearly 4 times lower) could be

considered strongly hypoxic. In future designs, the strength of hypoxia can be further increased by increasing the length of the exchangers.

In the present device, stronger hypoxia in the imaging region could be achieved by reducing the flow rate (and thus allowing more time for the $[O_2]$ equilibration). Nevertheless, a reduction of the flow rate has an unwanted effect of a less aggressive perfusion of the imaging region, thus exacerbating its contamination by $[O_2]$ that leaches out of the PDMS walls (which get saturated with air, when the imaging region is perfused with aerated medium). In addition, a reduction of the flow rate through a serpentine channel would lead to a proportional increase in the switching time (currently at ~2 sec). Last, but not least, high flow rate is important for the partial immobilization of the zebrafish larvae, forcing them to stay in the imaging region despite an increased rate of pectoral fin beats and body movements under hypoxic conditions. This partial immobilization is essential for consistent recording of the behavior of the larvae during the experimental trials.

Whereas the basic design of the imaging region is somewhat similar to that in a recent microfluidic device for high-resolution imaging of anesthetized zebrafish larvae[32], our experiments were performed on unanesthetized larvae and were specifically aimed at recording the pectoral fin beats and other motor responses of the larvae to hypoxia. Therefore, the dimensions of the imaging region in our device had to allow

body movements and pectoral fin beats, while preventing the larvae from escaping the imaging region as a result of the hypoxia-induced movements. To make the larvae stay within the imaging region during the 310 sec hypoxia trials, the length and, especially, the depth and width of the imaging region had to be iteratively optimized, with ~10 design iterations made. This optimization resulted in the successful completion of ~73% of the trials.

The key new functionality of the experimental setup, its ability to switch the O_2 content of the medium around a larva on a ~2 sec time scale, made it possible to study behavioral responses of the larvae to acute hypoxia with greatly improved temporal resolution. (In fact, the transition from hypoxic to normoxic medium conditions occurred even faster, with [O_2] increasing from <2% to ~13% on a scale of 1 sec; Fig. 3-2) As a result, we have been able to put a limit of <15 sec on the delay between the onset of hypoxia and the start of a behavioral response to it (increased rate of pectoral fin beats), an improvement of at least an order of magnitude as compared to response times of multiple minutes in previous studies[21-24]. The fast [O_2] switching also made it possible to establish a significant delay between the restoration of an aerated medium around a larva and cessation of a hypoxia-induced behavior. In the trials with strong hypoxia ([O_2] = 1.8%), the frequency of the pectoral fin beats was significantly elevated even after 20 sec past the time point when the medium became

fully aerated (Fig. 3-4a). The short switching time also allowed limiting the exposure of the larvae to hypoxia to 50 sec at a time, thus making it possible to avoid potential damage caused by prolonged exposure to hypoxia, to perform multiple trials on individual larvae, and to retrieve larvae alive and well from the device after series of trials. The proposed experimental setup with the computer-controlled gas mixer also greatly facilitated experimental trials with adjustable levels of hypoxia. Using this capability, we were able to observe a significant behavioral response to relatively weak hypoxia, with $[O_2]$ = 6.6% (~2.8 mg/mL). The response of the larvae to this weak hypoxia might have been enhanced by the short transition time (~2 sec) from normoxia to the hypoxia, leaving very little time for adaptation.

The proposed experimental setup can be used to test the influence of various pharmacological treatments and genetic modifications upon behavioral responses of zebrafish larvae to different levels of hypoxia. The setup can also potentially be adapted for the visualization of hypoxia responses on the level of neural circuits and individual neurons. Whereas the hypoxia trials with a simple temporal pattern of sequentially applied low and high $[O_2]$ have been informative, the experimental setup can readily generate more complex temporal patterns. For example, gradual time ramps of $[O_2]$ or intermittent strong and weak hypoxia can be used to study the cumulative effects of long-term hypoxia and adaptation to

reduced [O_2]. The experimental setup could also be used to expose zebrafish larvae to changes in the concentration of other dissolved gases, such as CO_2, NO, and N_2O. With some modifications in the dimensions of the fish channel, the experimental setup could be adapted to accommodate zebrafish of other ages or other aquatic model organisms.

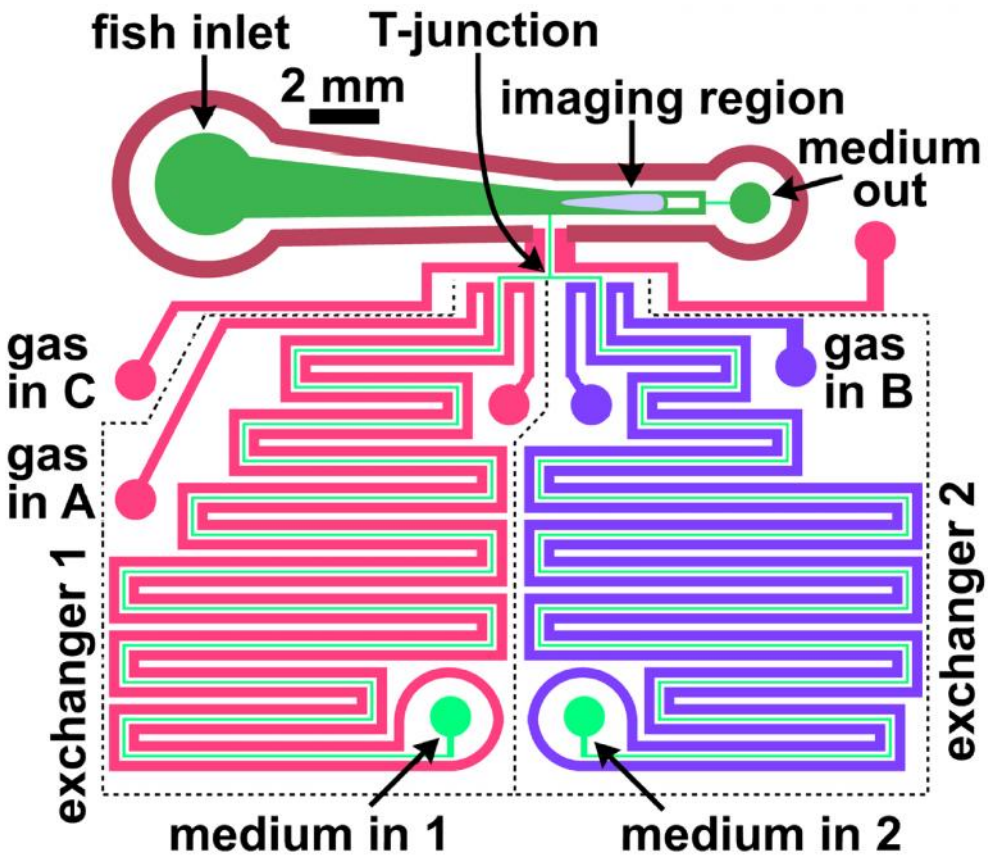

Figure 3-1: Diagram of channels in the microfluidic device. Gas inlets A, B, and C are labeled as gas in A, B, and C. Medium inlets 1 and 2 are labeled as medium in 1 and 2. Channels shown in light green (liquid-filled serpentine channels and a channel connecting the imaging region of the fish channel to the outlet) are 120 µm deep. Channels shown in pink (gas channels in gas exchanger 1 and gas channels connected to gas inlet C) and lavender (gas channels in gas exchanger 2) are ~265 µm deep. Channels shown in dark red (gas channels connected to gas inlet C) and green (the fish channel) are ~550 µm deep.

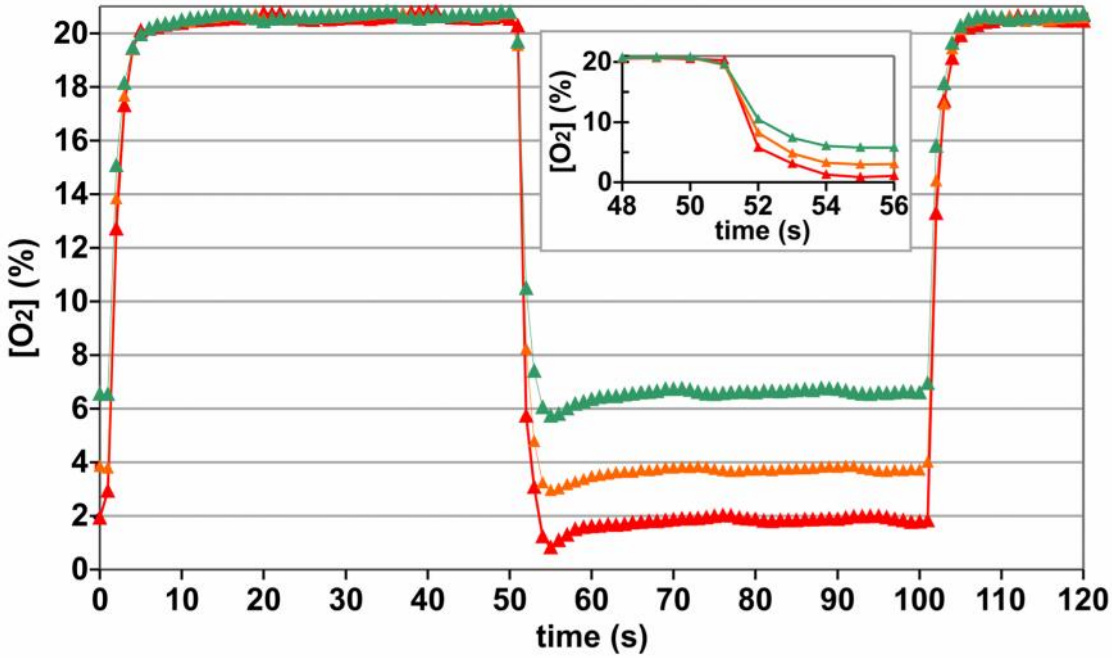

Figure 3-2: Oxygen concentration, $[O_2]$, at the downstream end of the imaging region as a function of time during experiments in which the active gas exchanger was switched between an exchanger ventilated with air ($[O_2]$ = 20.8%) and an exchanger ventilated with a hypoxic air/N_2 mixture with $[O_2]$ = 0 (red triangles), 2% (orange triangles), and 5% (green triangles). The switching from air to hypoxic air/N_2 mixtures was at ~50 sec; the switching from hypoxic mixtures to air was at ~0 and ~100 sec. *Inset*: close-up of the time interval from 48 to 58 sec, showing that transitions from aerated to hypoxic environments occur within ~2 sec.

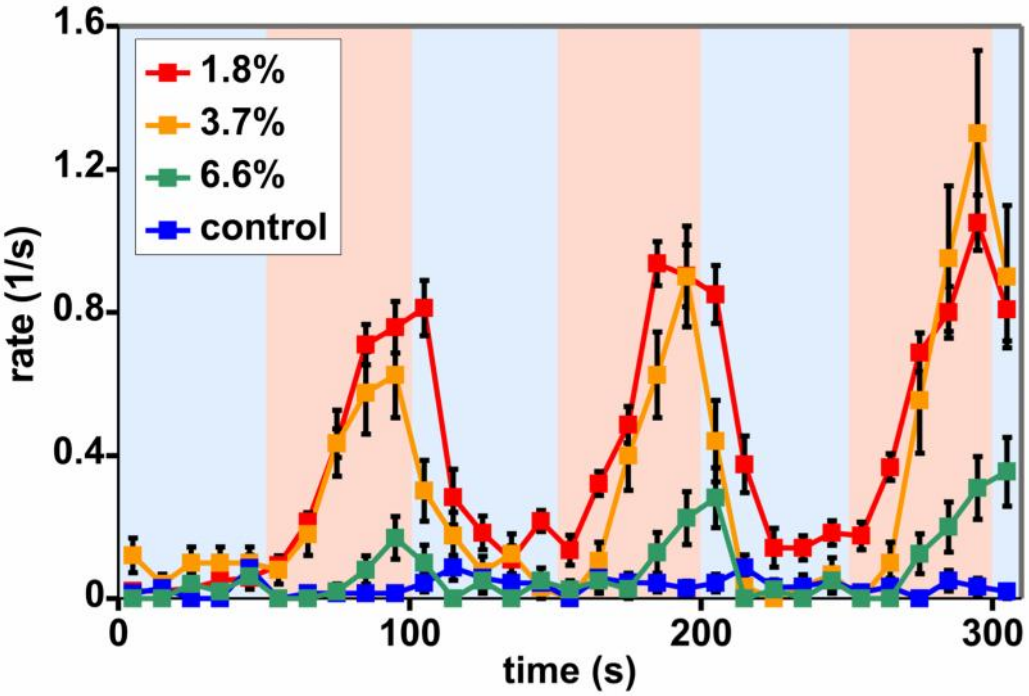

Figure 3-3: Rates of pectoral fin beats of zebrafish larvae during experimental trials as functions of time. In each trial, a zebrafish larva, which was initially in an aerated medium (until 50 sec), had three 50 sec exposures to a hypoxic medium (segments with red background) with two 50 sec exposures to an aerated medium in between (segments with blue background). Each data point is an average over a 10 sec interval and over multiple trials. Data for trials with hypoxic media with [O_2] = 1.8, 3.7, and 6.6% are shown in red, orange and green, respectively, representing 12, 2, and 4 complete trials, on 5, 2, and 4 larvae, respectively. Control (shown in blue) represents 6 complete trials on 4 larvae, in which both gas exchangers were ventilated with air, such that the zebrafish was exposed to aerated medium throughout the trial. Error bars are SEM based on the number of trials.

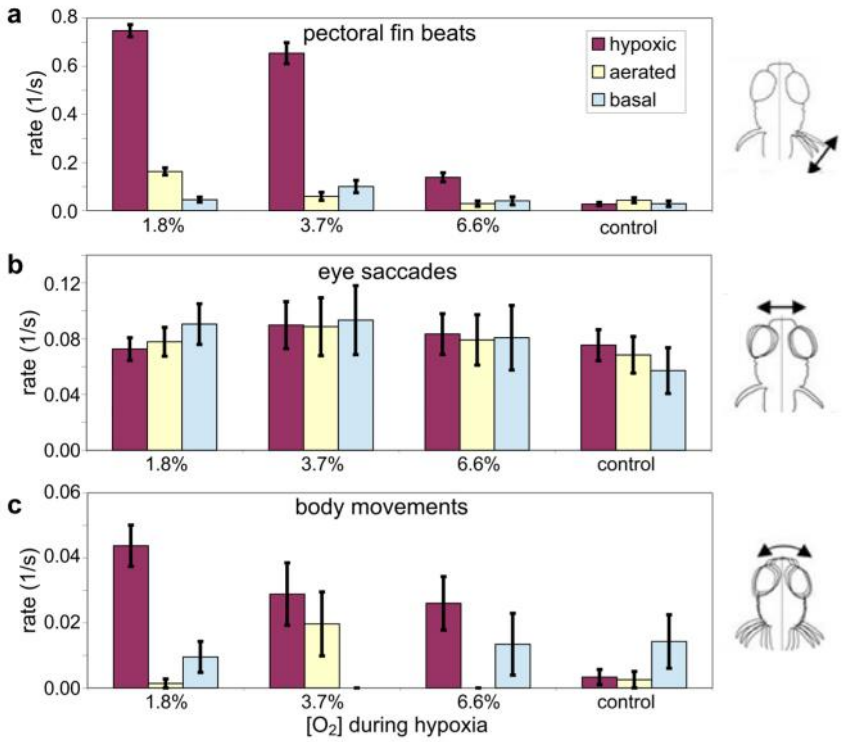

Figure 3-4: Bar charts of the rates of various zebrafish behaviors during different phases of the experimental trials with periodically switched [O_2] (cf. Fig. 3-3): (a) pectoral fin beats, (b) eye saccades, and (c) large body movements. Note that the maximal recorded rates of eye saccades (<0.1/s) and large body movements (<0.05/s) are both substantially lower than the maximal rate of pectoral fin beats (>0.7/s). During each trial, a zebrafish larva, which was initially in an aerated medium, had three 50 sec exposures to a hypoxic medium with two 50 sec exposures to an aerated medium in between. The bars are grouped by [O_2] of the hypoxic medium in the trial. Control represents trials with both gas exchangers ventilated with air, such that the zebrafish was exposed to aerated medium throughout the trial. The groups of bars for [O_2] = 1.8, 3.7, and 6.6% represent results of trials on 5 larvae, and the control bars represent results obtained from 4 larvae. The total numbers of complete trials are 12, 2, 4, and 6 for 1.8%, 3.7%, 6.6%, and control, respectively. The red bars (hypoxic) are averages over the last 30 seconds of each of the three 50 sec hypoxic exposures. The yellow bars (aerated) are averages over the last 30 seconds of each of the two 50 sec exposures to aerated medium between the exposures to hypoxic media. The light blue bars (basal) are averages over the last 30 seconds in aerated medium before the first exposure to hypoxia. Error bars are SEM based on the number of trials.

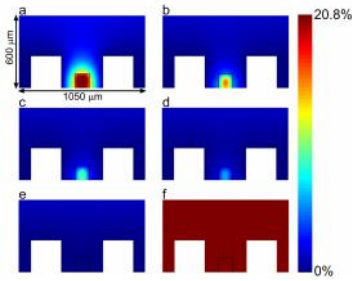

Figure 3-5: Comsol simulations of [O_2] profiles at 1.05 mm wide cross-sections of the PDMS chip, corresponding to one period of the gas exchanger channel network. The bottom 0.6 mm of the 6 mm tall computational domain (corresponding to the 6 mm thickness of the PDMS chip) is shown. The computational domain includes a single 120×120 µm liquid-filled channel, with boundaries highlighted by black lines at the bottom center, and also accounts for two 250×265 µm gas channels, which are represented by while rectangles protruding into the computational domain at the bottom left and bottom right. The boundary conditions are insulation at the bottom (corresponding to the cover glass) and on the sides (corresponding to a periodic [O_2] profile in an exchanger with many folds in the channels) and [O_2] = 20.8% at the top of the domain (top surface of the PDMS chip). The boundary conditions at the walls of the gas channels (rectangles at the bottom right and bottom left) are [O_2] = 0 for gas channels ventilated with N_2 and [O_2] = 20.8% for gas channels ventilated with air. The simulations use 1000 µm^2/s and 2000 µm^2/s for the diffusion coefficients of O_2 in PDMS and the liquid-filled channel and 10.4 and 1.3 mM/atm for the respective solubilities of O_2. (a) – (d) show [O_2] profiles at consecutive locations along the liquid-filled channel perfused at mean flow velocity of 52 mm/s with water, which is initially fully aerated, with [O_2] = 20.8%. The simulations account for the laminar profile of flow velocity in the channel (with zero velocity at the walls and maximal velocity at the center). (a) shows the [O_2] profile at 1 mm from the entrance, with mean [O_2] = 20.3%. As water moves along the channel, the effective mean value of [O_2] decays to 11.8% in (b), 7.2% in (c) and 4.4% in (d). The effective mean value of [O_2] is calculated as an average across the channel weighted with the local flow velocity, thus accounting for contributions of different streamlines into the total volumetric flux. (e) and (f) are cross-channel distribution with no flow in the channel and the gas channels ventilated with N_2 and air respectively. It is worth noting that the amount of O_2 removed from the PDMS and liquid-filled channel between (a), where the liquid-filled channel has [O_2] = 20.8%, and (e), where the liquid-filled channel has [O_2] = 0.15%, is much smaller than the difference in the amount of O_2 between (f) and (e), especially if one accounts for ~8 times higher solubility of O_2 in PDMS as compared to water.

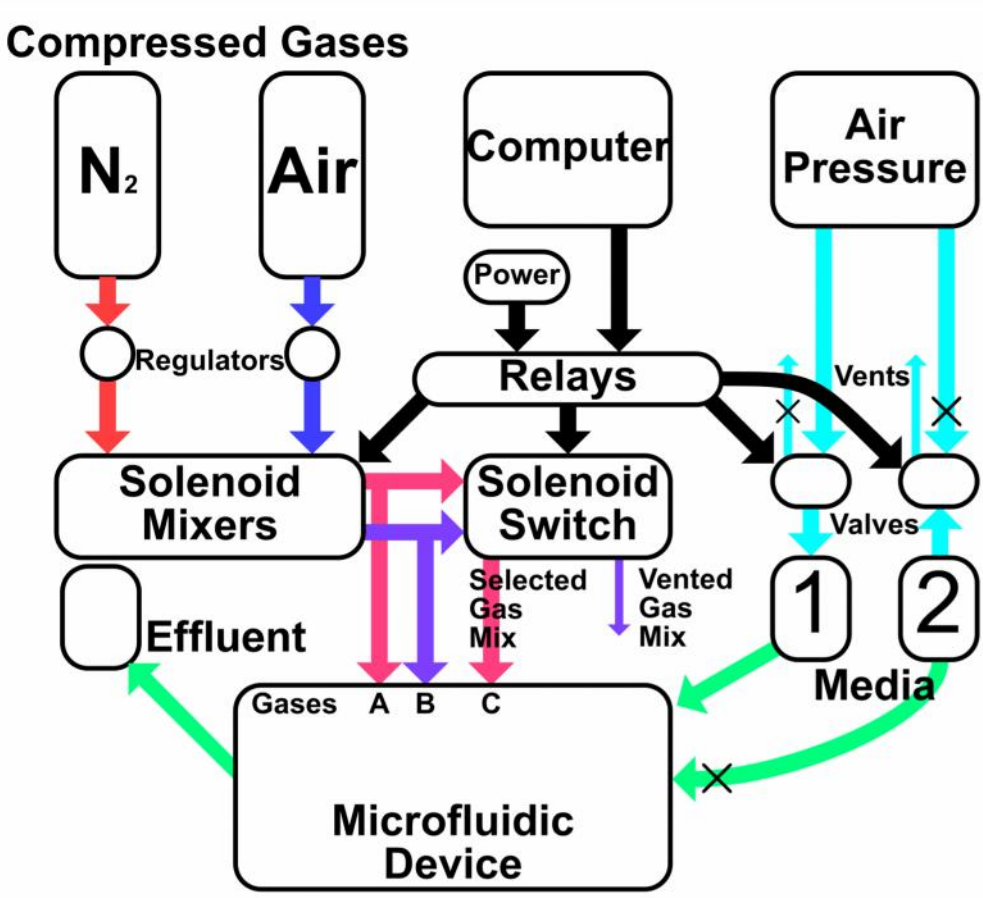

Figure 3-6: Schematic diagram of the microfluidic experimental system with arrows representing flows of N_2 and air gasses (red and blue), mixed gasses fed to exchanger 1 (pink) and 2 (purple), air pressure (light blue), media (light green), and electrical power and signals (black). The system is shown with exchanger 1 active and exchanger 2 passive (fast flow of the medium through gas exchanger 1 towards the imaging region and slow backflow through gas exchanger 2). In this state a solenoid valve switch (the assembly of two solenoid valves) vents gas mixture B and feeds gas mixture A (selected gas mix) into gas inlet C (the auxiliary channel inlet). As a result, the gas mixture supplied to gas inlet C (and the auxiliary gas channel) is the same as the gas mixture supplied to the active exchanger (exchanger 1, port A of the microfluidic device).

Chapter 3, in full, is in preparation for submission for publication as “A microfluidic system for studying the behavior of zebrafish under Acute Hypoxia”, Erickstad, Michael; Hale, Laura A.; Chalasani, Sreekanth H.; Groisman, Alex. The dissertation author is a co-first author and a leading contributor to this paper.

Chapter 4: A Natural Wave Device for Studying Chemotaxis and Memory in Dictyostelium discoideum

4.1: Microfluidic Device and Experimental Setup

Abstract

Dictyostelium discoideum (*Dicty*) is often called the social amoeba. A *Dicty* population responds to starvation by initialing a developmental process in which single cells aggregate to form a multicellular structure. In this process, traveling waves of the chemoattractant cAMP emanate from an aggregation center and are relayed by the surrounding cells. *Dicty* cells migrate towards the aggregation center using these waves as a homing beacon to direct their movements. As a wave passes, a single cell experiences both a 'forward' gradient (towards the wave source) as the wave rises and a 'backward' gradient (away from the wave source) as the wave falls. The mechanism that allows the cells to maintain a net motion towards the wave source is not well understood. To study this process, we have devised and constructed a microfluidic experimental system which sweeps bell shaped concentration waves of cAMP over a *Dicty* population. Our apparatus provides the opportunity to select the properties of the cAMP waves such as period, concentration, sweep velocity, etc. We present simulations, calculations, and tests which determined the optimal

operation of the system. We also present a method for simulating steady state 3-dimensional diffusion in a focused flow by using a time dependent 2-dimensional model. We compare these results to the results of dye experiments.

Introduction

Cellular migration is of essential importance in many biological processes including embryogenesis, wound healing, and tumor dissemination[1-5]. Many of the chemical mechanisms of cellular migration are conserved across a wide range of cell types[6-7]. Many prior studies have investigated chemotaxis in stationary gradients[8-9]. However, *in vivo* cues often vary in time[10-11] and chemotaxis in dynamic environments is not well understood.

The aggregation process of the social amoeba *Dictyostelium discoideum* (*Dicty*) is a prime example of chemotaxis in dynamic gradients. Upon starvation, populations of *Dicty* aggregate to form a multicellular structure for survival[12]. Their aggregation is coordinated by the controlled release and degradation (at the individual cell level) of the chemoattractant cyclic AMP (cAMP). Each cell emits cAMP as an excitatory response to the detection of an increase in cAMP, resulting in the formation of traveling waves of cAMP concentration. Cells migrate toward the source of the waves within their population.

Dicty cells are highly sensitive to stationary gradients of cAMP, preferentially traveling in the direction up the gradient. In nature, they successfully maintain motion traveling consistently toward the source of the waves (into the oncoming waves). They do this despite the fact that they spend an equal amount of time in the chemical gradient on the front of the wave (which when stationary would guide them toward the source of the waves) and the back of the wave (which when stationary would guide them away from the source of the waves). This apparent paradox is referred to as the back of the wave problem [13].

Studies probing the mechanisms by which *Dicty* cells are able to maintain persistent directed motion in the presence of cAMP waves have been limited due to the lack of a system that can generate controlled traveling waves of chemoattractant.

The goal of the system presented here is to mimic a "natural wave" of cAMP which will sweep over *Dicty* cells in a viewing area allowing the experimentalist to record the chemotactic response of the *Dictyostelium discoideum* cells to the chemoattractant wave stimulus.

The system was designed to avoid producing sensory and/or motility biases, other than the cAMP wave, which would influence cell motion along the axis of wave travel. This was accomplished by sweeping waves of cAMP in a direction orthogonal to the flow direction. Also, the flow velocity was

tuned such that the shear was sufficiently low not to significantly influence cell motion (or disrupt natural chemotactic responses).

It is thought that the Dicty cells' chemotactic response is proportional to the logarithmic gradient of the cAMP around the cell scaled by the length of the cell, $\frac{\Delta C_{cell}}{\overline{C}_{cell}} \cong \frac{\nabla C * l_{cell}}{\overline{C}} = \frac{\partial C}{\partial X} \cdot \frac{l_{cell}}{\overline{C}} = l_{cell} * \left(\frac{\partial}{\partial x} \right) \ln(C)$. As such, the presented system was designed to produce concentration profiles with logarithmic gradients of magnitudes satisfactory to invoke a chemotactic response. Moreover, the system produces waves which are similar (in: profile, magnitude, velocity, and period) to those which naturally occur in *Dicty* populations[14-15]. However, the system allows the user to control the profile, magnitude, velocity, and period of the waves.

Chip Design

The chip has five ports: an outlet used both during operation and during cell loading; a Dicty cell inlet used for loading cells and plugged during normal use; and three inlet ports named Buffer+, Buffer- and cAMP. Each inlet port connects to a fluid resistor which then leads its flow to the top of a ~6.9 mm (this is the length of the rectangular portion) long 2.2 mm wide observation channel (cf. Fig. 4-1).

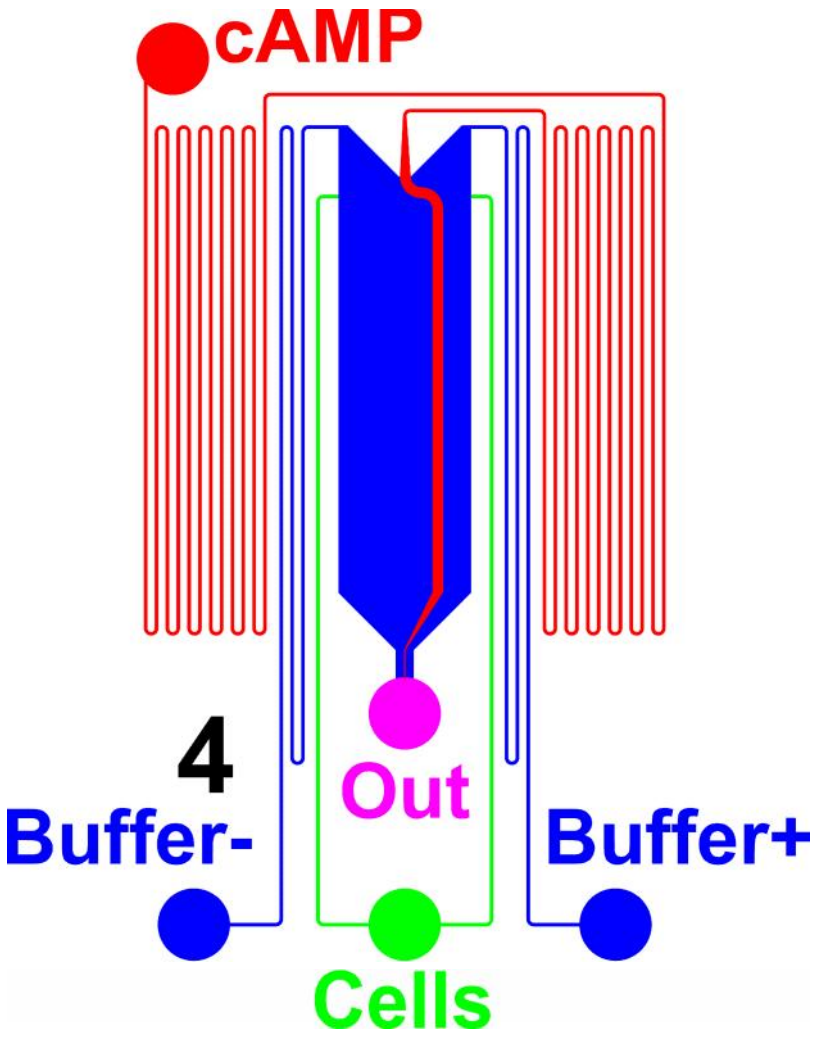

Figure 4-1: Color coded cartoon of the Dicty Wave Chip, with cAMP inlet (red) buffer inlets (blue), outlet (purple), and Dicty Cell loading port (green). In the large observing channel, the cAMP flow is represented in red. This figure depicts the flow pattern corresponding to $Q_{B-} > Q_{B+}$.

Concentration Profile

During normal operation (wave sweeping), the three flows from the inlets (Buffer+, Buffer- and cAMP) merge at the top of the observation channel (at a Y-type junction [16]) before flowing down to the outlet port.

The cAMP flow is sandwiched between the flows from the Buffer+ and Buffer- ports. This forms a cAMP concentration profile across the observation channel. The cAMP concentration profile is initially a square shaped plateau. As the three flow streams move down the observation channel towards the outlet, the cAMP in the cAMP flow stream diffuses into the adjacent buffer flow streams. During this time, the "unnatural" square chemical concentration profile initially formed at the confluence "softens" via diffusion into a more natural bell shaped concentration profile which becomes ever wider and softer with time.

Because increased time of flight after confluence results in a softer and broader bell profile, the user can select how broad of a chemical profile to use on the cells by simply observing cells at a specific distance from the confluence.

A fluorescent tracer dye Alexa 594 (which has a diffusion constant close to that of cAMP) was used during experiments on cells as a marker to track the diffusion and position of the cAMP profile.

Quasi 3-D Comsol Diffusion Simulation

The process of cAMP diffusion within the rectangular cross section of the observation channel of the chip was simulated in a 2-dimensional time dependent Comsol (COMSOL Inc. 10850 Wilshire Boulevard, Suite 800, Los Angeles, CA 90024, USA) simulation as follows. In the first step,

the flow velocity profile was calculated by solving the Poisson equation (time independent) over the channel cross section with a zero value boundary condition (Dirichlet B.C.) imposed at the channel walls to impose a no-slip boundary condition. A sufficiently large generative term was chosen for the Poisson equation and the solution was normalized by its maximal value to give a velocity distribution ranging from zero at the walls to one at the center of the channel.

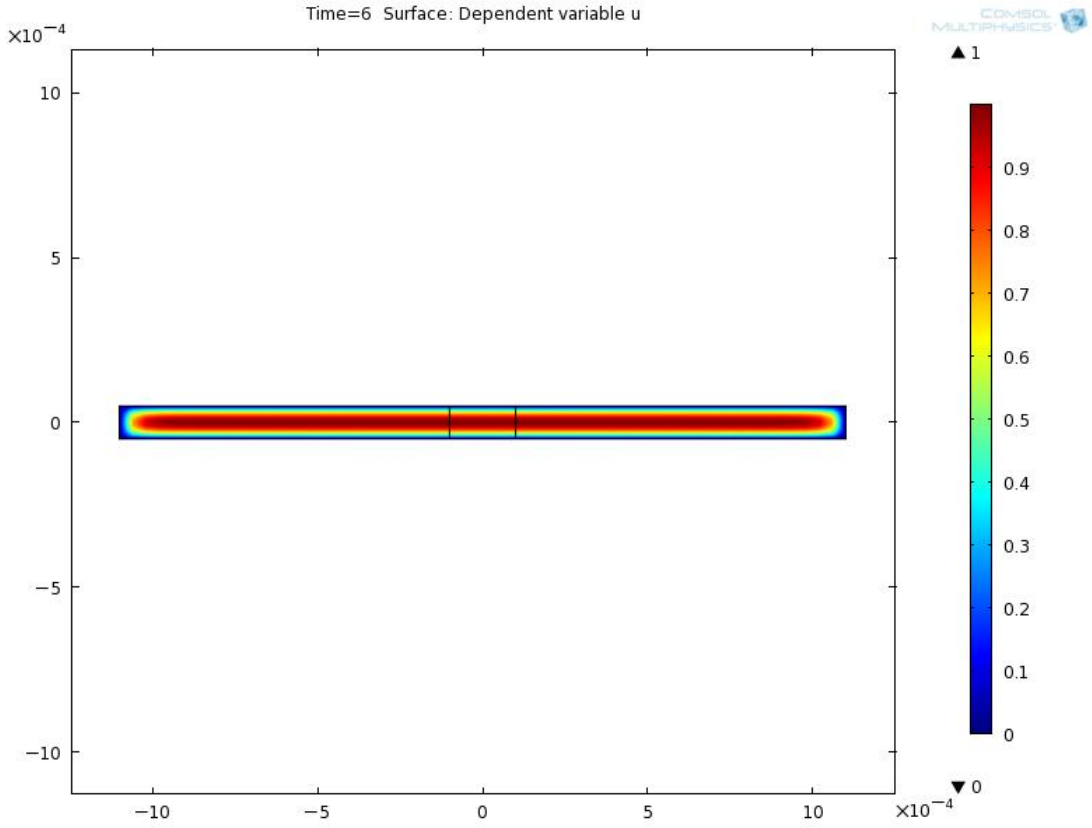

Figure 4-2: Calculated solution of Poisson's equation in 2 dimensions. This represents a flow velocity field moving along the y-axis of the chip (down the observation channel).

Next, the diffusion of the cAMP was simulated using a general form PDE with coefficients selected such that the equation was of the form

$$v\frac{\partial C}{\partial t} = D\nabla^2 C \tag{4-1}$$

where v is the normalized velocity solved for previously. This equation is similar to the diffusion equation with the key difference of the factor of v multiplying the time derivative. Rescaling the diffusion rate by velocity allows the 2-dimensional time dependent simulation to actually solve for the steady state 3-dimensional chemical profile in the form of successive cross sectional slices of the observation channel. The solution of each time step represents a position downstream (in the y-direction) instead of a time as given by $y_{slice} = t \circ v_{\max}$ where v_{max} is the maximum velocity of the flow. The substitution of y/v_{max} in place of t gives

$$v_{\max} v\frac{\partial C}{\partial y} = D\nabla^2 C \tag{4-2}$$

where v is unitless and ranges from 0 to 1. Rescaling the diffusion rate by velocity allows the slower moving fluid elements to undergo more diffusion as they travel an equivalent simulated step distance downstream in accordance with their increased residence times within each simulated step.

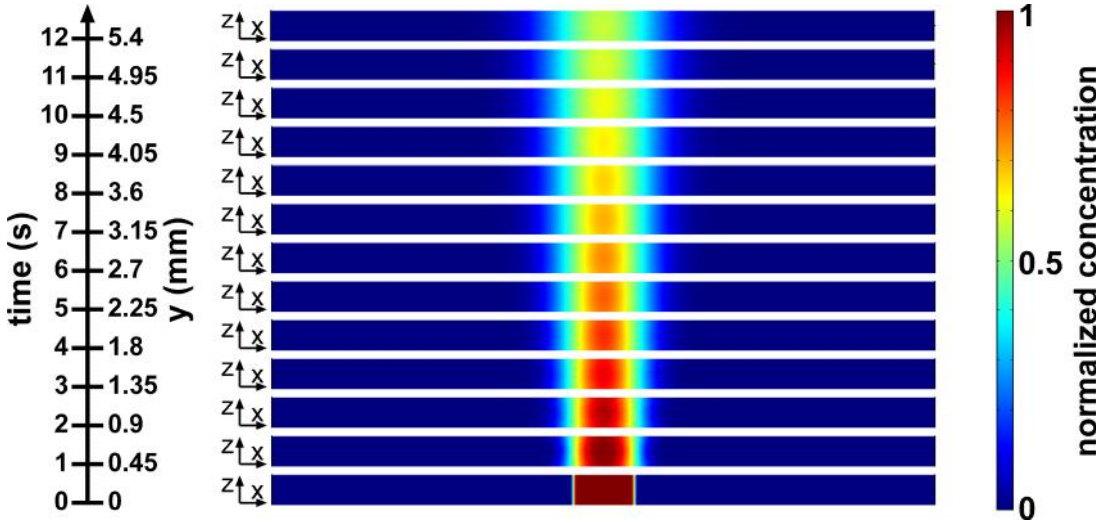

Figure 4-3: Diffusion of a chemical species simulated in pseudo 3-D using Comsol. Each subpanel represents the cAMP concentration for a cross-sectional slice of the flow across the observation channel at a different time post confluence i.e. position downstream from the confluence (the y axis assumes 450 µm/s max flow speed). The distribution is initially a 200 µm wide plateau in a 2200 µm wide 100 µm deep channel.

The integral of the product of the concentration multiplied by the flow velocity over the 2 dimensional cross section of the channel had a constant value from position to position (time-stop to time-stop), meaning that there was a conservation of chemical flux across successive cross sections consistent with a steady state solution. Of course, this method does not account for diffusion in the upstream and downstream direction (y-direction). However, transport due to diffusion in the upstream direction is weak compared to convective transport.

Using eq. 4-2, the magnitude of the diffusive flux in the downstream direction is approximated by

$$J_{Diff\_y} = D\frac{\partial C}{\partial y} = \frac{D^2\nabla_{x,z}^2 C}{V} \tag{4-3}$$

where $V=vv_{max}$ is the velocity of the fluid. Meanwhile the convective flux in the downstream direction is given by

$$J_{Conv\_y} = CV \tag{4-4}$$

Using the substitution $\nabla \to \frac{1}{L}$ to approximate the derivatives gives the ratio of the fluxes as

$$\frac{J_{conv\_y}}{J_{Diff\_y}} \approx \frac{V^2L^2}{D^2} = Pe^2 \tag{4-5}$$

where Pe is the Péclet number. The Péclet number is a unitless number that compares the strength of convective transport to that of diffusive transport. It makes sense that the Péclet number is squared because the upstream diffusion is driven by the broadening of the profile and the rate of broadening of the profile is controlled by the rate of diffusion relative to convection. Thus, the Péclet number is applied twice (once in calculating the strength of y-axis diffusion and once in comparing that diffusion to convection).

The Péclet number is low near the no slip boundaries. However, in this narrow region, diffusion perpendicular to the boundaries should dominate over diffusion along the boundaries.

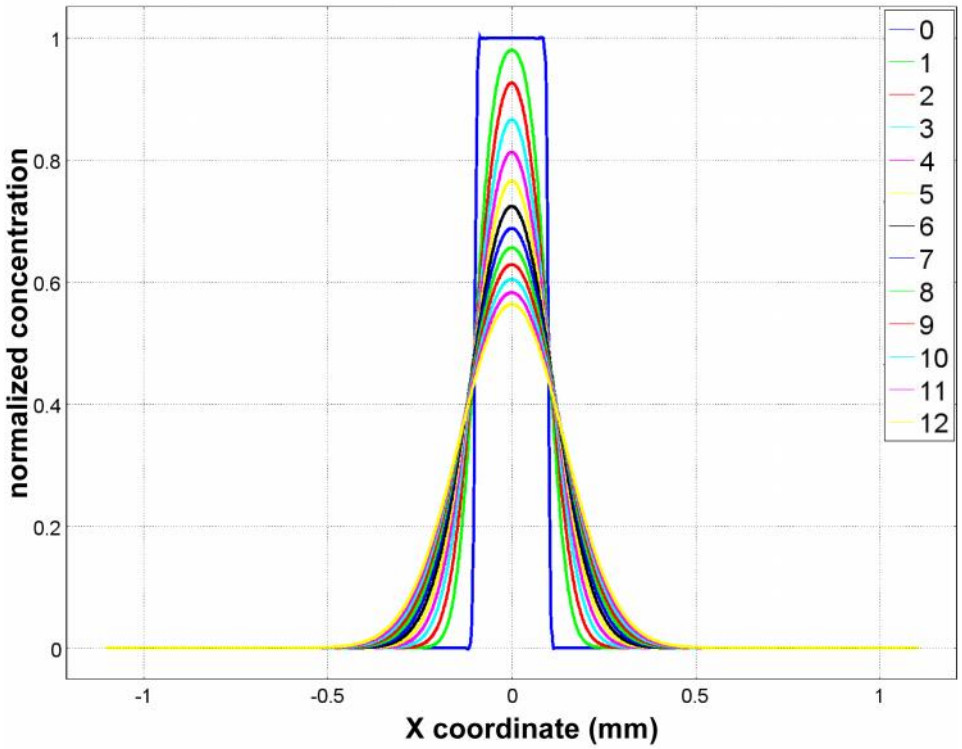

Figure 4-4: Simulated concentration vs. x position across the observation channel near the floor (2 µm above the glass) at various y positions (positions downstream from the confluence of the cAMP and buffer streams) as measured in seconds at the max flow velocity ranging from 0 to 12 seconds.

Sweep Process

The sweep motion of the wave is performed by changing the ratio of the volumetric flow entering the chip from Buffer+ (Q_{B+}) and Buffer- (Q_{B-}) while holding the total volumetric flow rate (Q_{tot}) constant. When the volumetric flow rates of the two buffers are unequal the (laminar) flow will redistribute across the observation channel in accordance with

conservation of volume. The position of the peak of the cAMP wave X_{wave} is approximately given by

$$X_{\text{wave}} \approx W \frac{Q_{\text{B-}} + \frac{1}{2} Q_{\text{cAMP}}}{Q_{\text{B-}} + Q_{\text{B+}} + Q_{\text{cAMP}}} \tag{4-1}$$

where W is the width of the channel $Q_{\text{B-}}$, Q_{cAMP}, and $Q_{\text{B+}}$ are the volumetric flows from Buffer- cAMP and Buffer + and

$$Q_{\text{tot}} = Q_{\text{B-}} + Q_{\text{B+}} + Q_{\text{cAMP}} \tag{4-2}$$

When, for instance, $Q_{\text{B-}}$ (the Buffer current entering from the Buffer- port on the left) is greater than $Q_{\text{B+}}$ (that from Buffer+ on the right) the flow in the observation channel redistributes such that the cAMP flow will be shifted toward the "right" (positive x) side of the observation channel. The converse is true when $Q_{\text{B-}}$ is less than $Q_{\text{B+}}$.

The system sweeps the chemical concentration profile across the channel by starting with $Q_{\text{B+}}$ low and $Q_{\text{B-}}$ high, and then gradually (smoothly) increasing $Q_{\text{B+}}$ while simultaneously decreasing $Q_{\text{B-}}$ at an equal rate. As a result, the cAMP streamlines (the center of the cAMP profile) smoothly shift in time and eventually the entire wave profile is drawn across the *Dicty* cell population under observation.

In experiments on cells, the ideal position of the window of observation was chosen such that the cAMP wave profile has evolved to

have a natural profile. The window also excluded regions of the observation channels which were too close to (approximately within a "wave length" of) the walls, ensuring that the cells in the observation window experienced the entirety of each wave profile as it moved past. The window was ~2.5-3 mm downstream of the confluence with the max flow velocity at ~467 μm/s.

The cycle by which the cAMP wave repeatedly sweeps across the observation channel is as follows:

(1) Initially ($t=t_0$), cAMP is flowing, meanwhile, the pressure at the Buffer+ port (P_{B+}) is "low" and that for Buffer- (P_{B-}) is "high". As a result, the cAMP flow streamlines shifted to the right side of the observation channel before leading down to the outlet. From the start P_{B-} (the pressure at the Buffer- port) is ramped down at a near constant rate while P_{B+} (that of Buffer+) is ramped up at an equal an opposite rate, causing the cAMP flow streamlines to gradually shift leftward at a near constant rate. (In the work presented here, the flow rate down the channel was fast when compared with the sweep rates used (> 24 times faster than the sweep rate). Thus, the cAMP stream remained oriented nearly in parallel with the channel walls.) After a time (t_{sweep}), the cAMP streamlines have been swept across the observation channel, and the buffer pressures have

switched such that the pressure P_{B+} is "high" ($P_{B+}(t_{sweep})=P_{B-}(t_0)$) and the pressure P_{B-} is "low" ($P_{B-}(t_{sweep})=P_{B+}(t_0)$).

(2) At this time ($t=t_{sweep}$), the cAMP flow is halted for ~10 seconds (t_{purge}) and slowly backflows toward the cAMP inlet while the remaining cAMP in the observation channel is purged from the observation channel by the buffer flows. The cAMP flow is stopped by lowering the pressure at the cAMP inlet (P_{cAMP}) to a pressure below that of the outlet resulting in a backflow in the cAMP line.

(3) P_{B+} and P_{B-} are reset (to P_{B+} low and P_{B-} high) to their initial values while the cAMP line is still backflowing. (~20 seconds are allocated to this process to ensure a completer reset.)

(4) The cAMP flow is restored (P_{cAMP} is restored to its previous value) and the sweep cycle begins again.

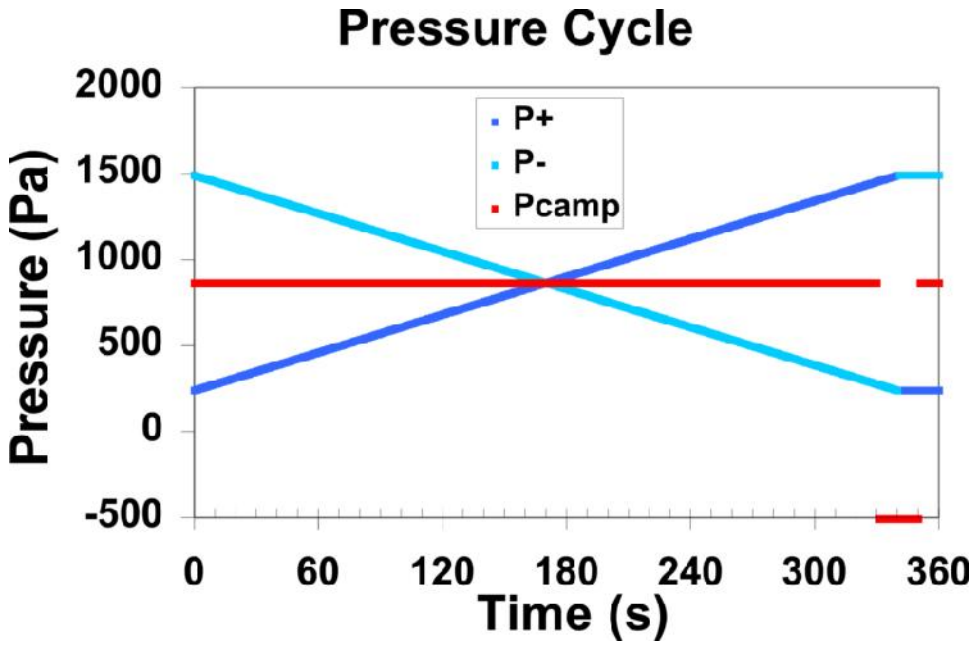

Figure 4-5: Cartoon of ideal pressures (P_{B+}, P_{B-}, and P_{cAMP}) during each wave sweep cycle.

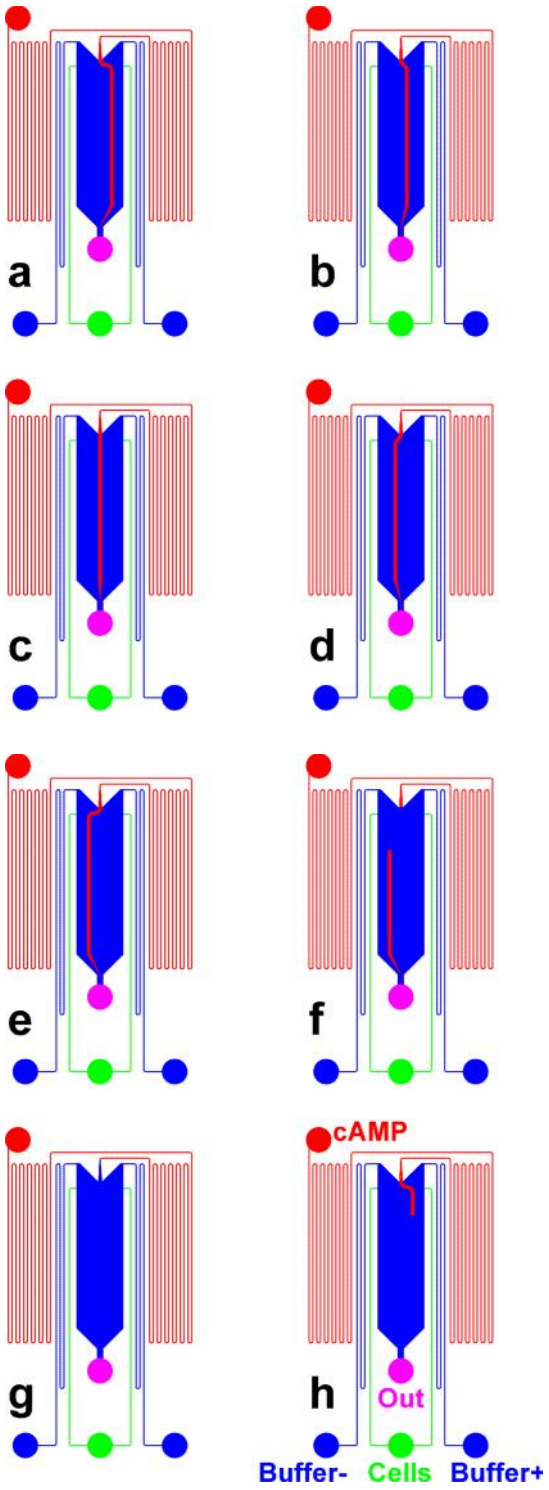

Figure 4-6: The wave sweep cycle. a-e) Cartoons of chip depicting the pressure ramp step (Q_{B+} increasing Q_{B-} decreasing). (f) Cartoon of chip depicting cAMP purge step. (g) Cartoon of chip depicting buffer pressure reset step. (h) Cartoon of chip during cAMP flow restoration

3-D Comsol Flow Simulation

The flow redistribution across the observation channel as a result of unequal Q_B's in 3 dimensions was simulated for multiple Q_B value pairings which occur during a sweep using a series of 3-dimesional steady state Comsol simulations.

The Control System

The reservoirs consist of industrial grade ~357.5 mL syringes with custom machined aluminum plugs. Each cap has 3 ports, 2 for capillaries (of different lengths in order to achieve a large range of time constants) and one for a vent. Each plug also has a relief around its circumference for an O-ring that forms a seal against the inner wall of the syringe (the seal is enhanced using Dow Corning Vacuum Grease). Each machined aluminum plug has two bottom tapped mounting cites that securely hold the plug against the stock plastic syringe lid (modified with trough holes for the three ports and two mounting screws) using two socket cap screws with washers such that the plug is held in place on the syringe via the threading of the plastic lid.

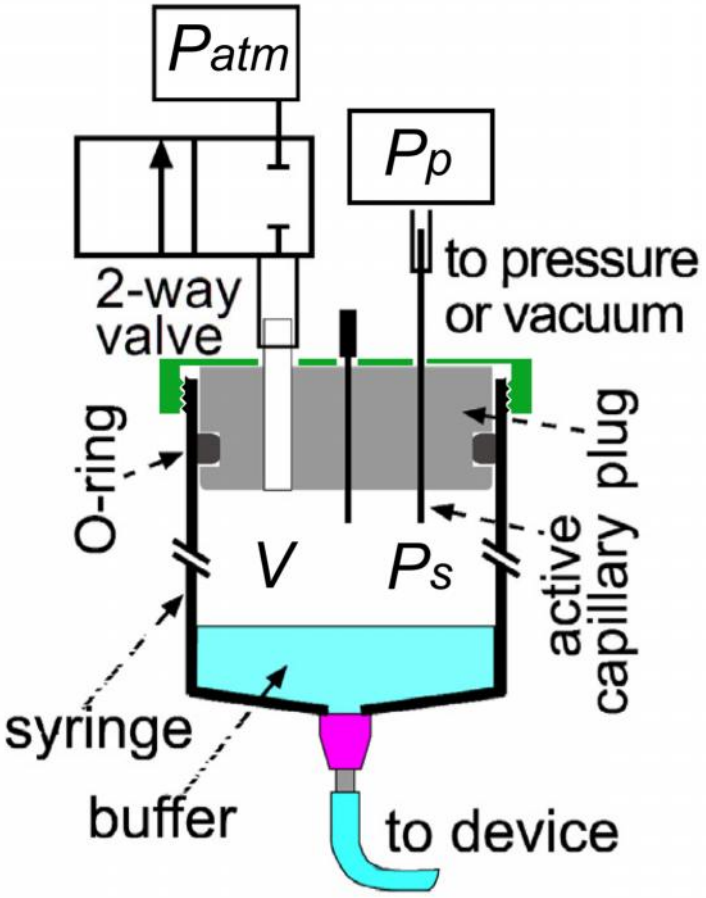

Figure 4-7: Schematic of syringe-reservoir used to control buffer flow rates.

Changes in buffer inlet pressures (P_{B+} and P_{B-}) during the pressure ramp step are imposed pneumatically. The Buffer+ reservoir is perpetually connected to a regulated supply of compressed air via a ~10 cm long thin capillary (ID = 76 µm). As a result a stream of air constantly enters the headspace (estimated at ~320 mL) of the reservoir causing the pressure inside to increase when the headspace is otherwise sealed from the

atmosphere. Conversely, the Buffer- reservoir is connected to a regulated vacuum supply via a nearly identical capillary. As a result gas is constantly drawn out of the headspace of the Buffer- reservoir.

Both reservoirs are connected to solenoid valves that vent the headspace of the syringes to the atmosphere during the pressure reset step in order to restore the pneumatic pressure in both reservoirs to atmospheric pressure (~101 kPa). The solenoid valves receive their power from a standard DC converter in series with a relay board (for computer control). The relay board receives TTL control signals from the parallel port connector of a laptop computer (IBM Thinkpad T-42) running a homemade standalone Matlab code. The cAMP reservoir is placed ~51 mm below the outlet fluid level such that it slowly backflows when it is not pneumatically pressurized (with ~1.4 kPa) into a forward flow state. The cAMP reservoir headspace connects to a solenoid valve that connects it to a regulated supply of compressed air when the solenoid valve is in the unpowered state. This solenoid is controlled by the relay board and opens the cAMP headspace to atmospheric pressure when it is powered (during the cAMP purge and pressure reset steps). The Buffer+ and Buffer- fluid levels are placed at heights of ~25 mm and ~152 mm above the outlet reservoir fluid level. Thus, directly after venting, Q_{B+} is low and Q_{B-} is high, due to hydrostatic pressure.

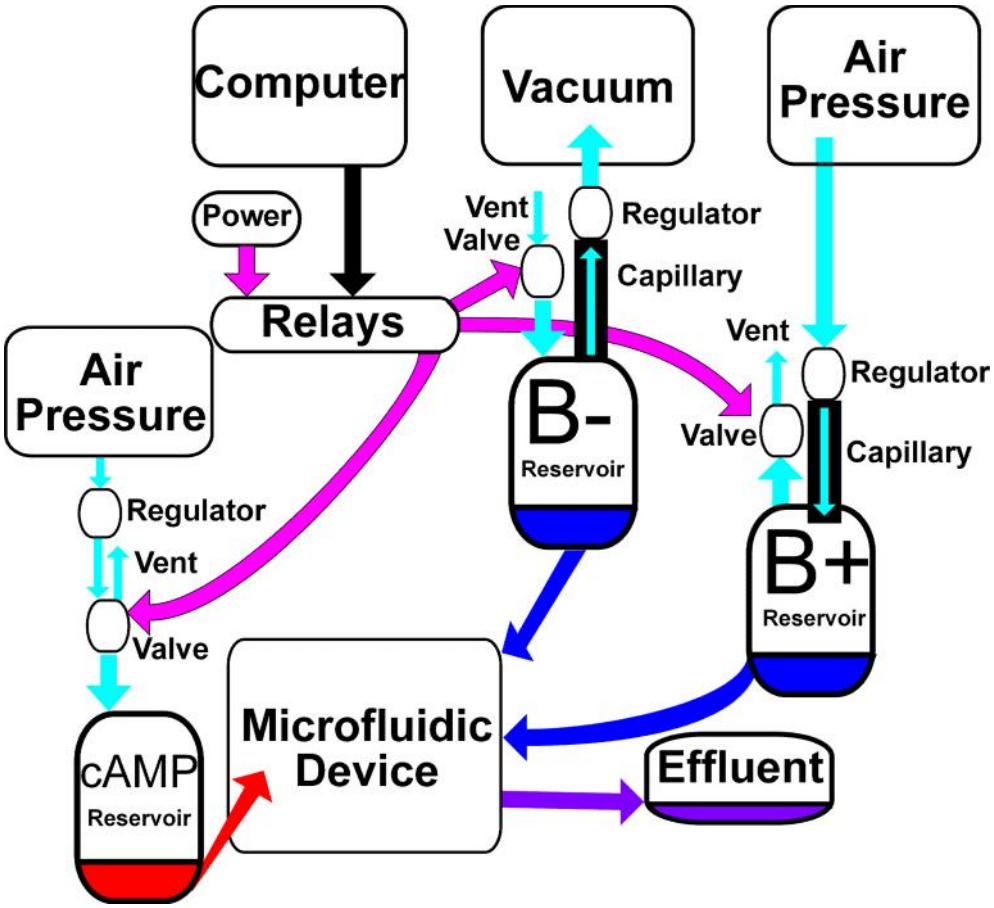

Figure 4-8: Block diagram of the Dicty Wave Control System including the microfluidic device. Solenoid valves are labeled as valves. Air flows are represented by light blue arrows, Buffer by blue arrows, cAMP by red, effluent by purple, and power electricity by pink. Note that the vertical position of the fluid levels in the reservoirs is accurate to the operation of the system (although not to scale). Also, note that the gas flows depicted entering and exiting the solenoid valves are not perpetual, but instead vary during wave the sweep cycle.

4.2: Calibration and Validation of the Apparatus

Calibration of the Syringes

The rate of buffer pressurization was characterized as a function of applied pressure (or vacuum) by observing the total water column rise over a 360 second interval at several pressure settings for the Buffer+ syringe reservoir and several vacuum pressure settings for the Buffer- syringe reservoir. Each reservoir's liquid outlet was connected to a long piece of transparent tubing with an ID of 1/16" ~1.6 mm. This diameter was chosen to minimize volume loss resulting from capillary rise while simultaneously having a large enough diameter to avoid excessive hydrodynamic resistance and drag at the three phase contact point. Each tube was mounted vertically along the markings of a meter stick. The reservoirs were filled to a marked fill line (~20 ml) with water and 0.05% Tween-20 (by mass). The Tween detergent was used to reduce surface tension in the measuring tube. To get the most accurate results, during each run the 360 second timer was not started until the water column had already risen or fallen by 2 cm from its initial resting position, preventing artifacts due to (relaxation) transients.

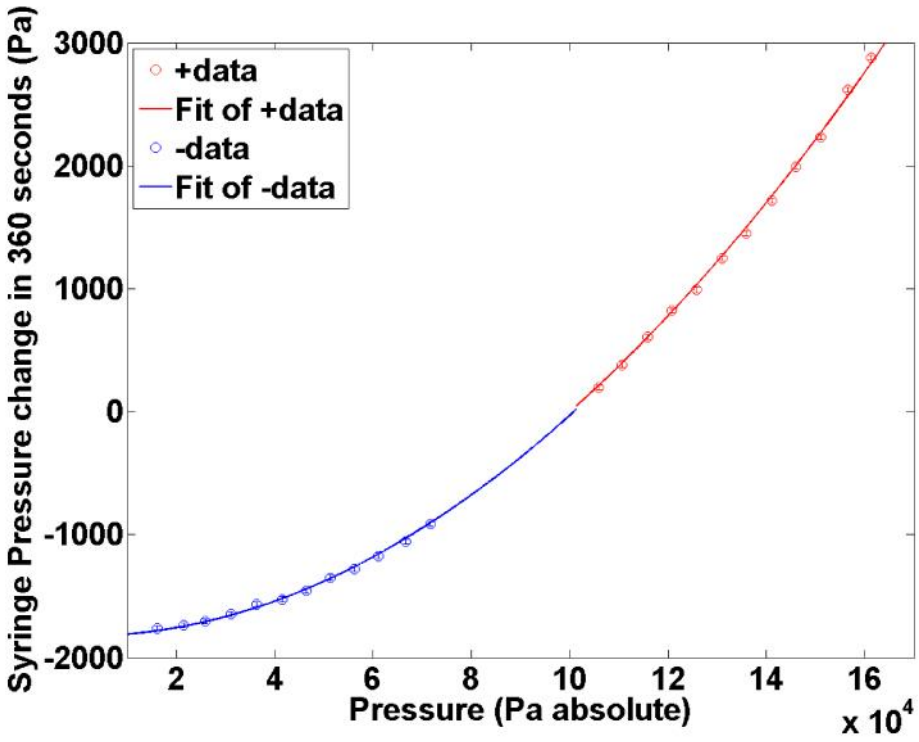

Figure 4-9: Calibration curve for reservoir pressurization

The calibration data was fitted, accounting for changes in the volume of the headspace (due to the fluid volume entering the Buffer- syringe reservoir or exiting Buffer+ syringe reservoir from or into the water column tube) as is described in the following sections.

Derivation of Volumetric Flow Rate through a capillary for a compressible gas

Assuming low Reynolds number, our flow is governed by the Stokes equation

$$\eta(\nabla \cdot \nabla)\vec{V} = \nabla P \tag{4-3}$$

where η is dynamic viscosity $\vec{V}$ is the velocity field vector and P is the pressure. Assuming local incompressibility, we can solve for the velocity field for a cylindrical tube to get

$$\vec{V} = V_{max}\left(1-(r/a)^2\right)\hat{z} \tag{4-4}$$

where a is the radius of the tube, r is the radial cylindrical coordinate, and V_{max} is given by

$$V_{max} = -\frac{a^2}{4\eta}\frac{dP}{dz} \tag{4-5}$$

Integrating the flow velocity field on a circular surface going across the cylinder gives the total volumetric flow rate (Q) through any given cross-section (of constant z) of the cylinder

$$Q(z) = \frac{\pi a^4}{8\eta}\frac{dP(z)}{dz} = \frac{L}{R}\frac{dP}{dz} \tag{4-6}$$

where R is the hydrodynamic resistance one would use for the cylinder under circumstances of incompressible flow. However, this flow is compressible. To account for global compressibility, adding considerations of conservation of number (mass) and the natural gas law yields

$$\frac{P_pQ_p}{kT} = \frac{P_sQ_s}{kT} = \frac{P(z)Q(z)}{kT} = \frac{dN}{dt} = F \tag{4-7}$$

where F (number flux) independent of z and the subscripts p and s denote conditions at the pressure regulator and syringe ends of the capillary

respectively. (Adiabatic cooling is assumed to have a negligible effect.) Plugging in the expression for Q gives

$$F = -\frac{\pi a^2}{8\eta} P \frac{dP}{dz} \tag{4-8}$$

After integration along the z-axis this becomes

$$LF = -\frac{\pi a^2}{8\eta} \frac{P_p^2 - P_s^2}{2} \tag{4-9}$$

which simplifies to

$$Q_s = \frac{P_p{}^2 - P_s{}^2}{2RP_s} = \frac{dN_s}{dt} \cdot \frac{kT}{P_s} \tag{4-10}$$

Pressurization of Reservoir Head-space

The theoretical expression for the pressurization curve of our reservoirs is derived as follows.

The process of increasing the pressure of the gas in the buffer headspaces via a slow influx of gas through a capillary is conceptually analogous to the charging or discharging of a capacitor through a resistor (in an R-C circuit). However, they are not mathematically identical due to the nonlinear (non-Ohmic) *Q-P* curve (*I-V curve*) of compressible fluids flowing in a capillary.

This derivation is done neglecting changes in volume and treating temperature as a constant. However, the case of changing headspace volume will be later.

In this case, the ideal gas law

$$P_s V_s = N_s kT \tag{4-11}$$

states that the pressure will vary as a result of the addition or removal of gas particles form the volume. Taking the derivative with respect to time yield

$$V_s \frac{dP_s}{dt} = kt \frac{dN_s}{dt} \tag{4-12}$$

The previously derived flow rate of gas through a capillary is given by

$$Q_s = \frac{P_p{}^2 - P_s{}^2}{2\mathrm{R}P_s} = \frac{dN_s}{dt} \cdot \frac{kT}{P_s} \tag{4-13}$$

rearranging and combining these yields

$$\frac{dP_s}{dt} = \frac{kt}{V_s} \frac{dN_s}{dt} = \frac{P_p{}^2 - P_s{}^2}{2\mathrm{R}V_s} \tag{4-14}$$

This can be directly integrated from initial condition to final (current) conditions as

$$\int \frac{dP_s}{P_p^2 - P_s^2} = \int \frac{dt}{2V_s R} \tag{4-15}$$

to get the expression for the pressure in the syringe as a function of time

$$P_s(t) = P_p \tanh\left(\frac{P_p}{2RV_s}(t - t_0) + Atanh\left(\frac{P_s(t_0)}{P_p}\right)\right) \quad (4\text{-}16)$$

Note that, for values of P_p below $P_s(t_0)$ the inverse hyperbolic tangent function gives a complex value. However, the imaginary component of this complex value is $-i\frac{\pi}{2}$ for all values of $\frac{P_s(t_0)}{P_p} > 1$, meanwhile, $\tanh(x + -i\pi/2) = \coth(x)$. This makes sense when one considers the fact that all of the pressures are absolute (positive), yet if a "vacuum" (pressure less than the initial pressure) is applied, the curve must have a negative slope.

Just as in a capacitor filling curve, the filling curve for gasses is initially linear and stays approximately linear for a brief time relative to the time constant of the filling curve. ($\tau_p = \frac{2RV_s}{P_p}$ gives the relevant timescale of the process.) Due to this initial linearity each syringe can be vented to atmosphere periodically, with a short period, such that the pressure in its headspace as a function of time is a saw tooth wave train with nearly linear ramps.

Taylor Expansion of Pressurization Curve

Considering that the pressures are applied over relatively short times before venting in order to achieve nearly linear filling rates, it is

natural to take interest in the tailor expansion of the filling curve. There is a trick which makes it easy to directly derive the Taylor expansion to however many terms are needed from the equations of state, instead of Taylor expanding the derivative of the previously derived solution (eq. 4-16). The general expression for the Taylor expansion of the rate of pressurization to second order in time is

$$\frac{dP_s}{dt}(\Delta t) \approx \left(\frac{dP_s}{dt}\right)_0 + \Delta t\left(\frac{d^2P_s}{dt^2}\right)_0 + \Delta t^2\left(\frac{d^3P_s}{dt^3}\right)_0 \qquad (4\text{-}17)$$

Using the expression $\frac{dP_s}{dt} = \frac{P_p{}^2 - P_s{}^2}{2\mathrm{R}V_s}$ immediately yields the first term of the expansion. Next the following trick is applied.

Consider a function $f = f(h(t))$ which has the property that $f = \frac{dh}{dt}$.

In this case, the chain rule states that $\frac{df}{dt} = \frac{df}{dh}\frac{dh}{dt}$. Combining these, gives $\frac{df}{dt} = \frac{df}{dh} f$, which is not explicitly dependent on time and defines $\frac{df}{dt}$ without using time derivatives.

This trick can be applied multiple times to get expressions for the coefficients of successively higher and higher order terms of the Taylor expansion as follows. First, the second derivative ($\frac{d^2P_s}{dt^2}$) is solved by taking $h = P_s$ and $f = \frac{dP_s}{dt}$. Then, this result is applied to get the third

derivative term by taking $h = \frac{dP_s}{dt}$ and $f = \frac{d^2P_s}{dt^2}$. With the inclusion of these coefficients the expansion takes on a useful form

$$\frac{dP_s}{dt} \approx \left(\frac{dP_s}{dt}\right)_0 \left[1 + \Delta t\left(\frac{-P_{so}}{RV_s}\right) + \Delta t^2 \frac{3P_{so}^{\ 2} - P_p^{\ 2}}{(2\mathrm{R}V_s)^2}\right] \quad (4\text{-}18)$$

where $\left(\frac{dP_s}{dt}\right)_0 = \frac{P_p^{\ 2} - P_{so}^{\ 2}}{2\mathrm{R}V_s}$. Note that $^2{}_s = \frac{2\mathrm{R}V_s}{P_{so}}$ presents itself as a natural time constant for this expression. This form of the expansion is convenient because the second term in the expansion gives a quick estimate of the fraction by which the pressurization rate will deviate from the initial pressurization rate as a function of time.

Pressurization Curve for Calibration

We now consider the form of the pressurization curve given the conditions in which we made our calibration measurements. Expressly, we consider conditions in which the volume of the headspace is not a constant, but varies because the liquid in the syringe is free to flow from the syringe into a vertically oriented line of tubing.

The following derivation assumes that the water column in the vertically oriented piece of tubing rises such that the hydrostatic pressure cancels the pneumatic pressure in the headspace of the syringe (and that it

is near equilibrium during the process). Under this assumption, the volume of the headspace of the syringe is given by

$$V_s(t) = V_{so}(1 + \gamma \Delta P_s(t)) \tag{4-19}$$

where $\gamma = \frac{1}{V_{so}} \frac{\pi r^2}{\rho g}$, r is the radius of the tube, g is gravitational acceleration on the earths surface, and ρ is the density of the liquid. The natural gas law and the chain rule give

$$\frac{dP_s}{dt} = \frac{\partial P_s}{\partial N_s} \frac{\partial N_s}{\partial t} + \frac{\partial P_s}{\partial V_s} \frac{\partial V_s}{\partial t} \tag{4-20}$$

As previously derived the number flux is given by

$$\frac{\partial N_s}{\partial t} = \frac{1}{kT} \frac{P_p^{\,2} - P_s^{\,2}}{2\mathrm{R}} \tag{4-21}$$

applying the new definition of V_s (eq. 4-19) gives

$$\frac{\partial V_s}{\partial t} = V_{so} \gamma \frac{dP_s}{dt} \tag{4-22}$$

Plugging equations 4-22 and 4-21 into eq. 4-20 results in

$$\frac{dP_s}{dt} = \frac{P_p^{\,2} - P_s^{\,2}}{2\mathrm{RV}_s} - \frac{P_s}{V_s} V_{so} \gamma \frac{dp_s}{dt} \tag{4-23}$$

which simplifies to

$$\frac{dP_s}{dt} = \frac{P_p^{\,2} - P_s^{\,2}}{2\mathrm{RV}_s \left(1 + P_s \gamma \frac{V_{so}}{V_s}\right)} = \frac{P_p^{\,2} - P_s^{\,2}}{2\mathrm{R}(V_s + P_s \gamma V_{so})} \tag{4-24}$$

applying the definition of V_s (eq. 4-19) again to gives

$$\frac{dP_s}{dt} = \frac{P_p{}^2 - P_s{}^2}{2\mathrm{RV}_{so}\left(1+\left(P_s + \Delta P_s\right)\gamma\right)} = \frac{P_p{}^2 - P_s{}^2}{2\mathrm{RV}_{so}\left(1+\left(2\mathrm{P}_s - P_{so}\right)\gamma\right)} \tag{4-25}$$

Using the aforementioned method for finding the coefficients of a Taylor expansion, the filling curve is approximated to first order in time as

$$\frac{dP_s}{dt} \approx \left(\frac{dP_s}{dt}\right)_0 \left\{1 + -\Delta t\left[\frac{P_{so}}{RV_{so}\left(1+P_{so}\gamma\right)} + \frac{\gamma\left(P_p{}^2 - P_{so}{}^2\right)}{RV_{so}\left(1+P_{so}\gamma\right)^2}\right]\right\} \tag{4-26}$$

where $\left(\frac{dP_s}{dt}\right)_0 = \frac{P_p{}^2 - P_{so}{}^2}{2\mathrm{RV}_{so}\left(1+P_{so}\gamma\right)}$. In order to fit the calibration data the Taylor expansion is integrated in Δt to give an expression in terms of ΔP_s, which is calculated by the change in hydrostatic pressure indicated by the water column over a time Δt. The value of RV for the Buffer+ and Buffer- reservoir syringes were found to be ~$9.27\text{x}10^8$ Pas and $9.21\text{x}10^8$ Pas by Matlab fit in decent agreement with what we expect from theory.

Verification of Functionality

The functionality of the system was verified using fluorescein as a tracer dye to determine the cAMP profile and tracer beads to determine the maximum flow velocity under the same settings as used for cell experiments.

The flow velocity in the observation channel was calculated using 1.9 µm diameter dragon green beads (Bangs Laboratories, Inc. 9025

Technology Drive, Fishers, IN 46038-2886). The maximum velocity in the flow profile was estimated by taking micrographs with sufficiently long exposure time that the moving beads appear as streaks. (In such experiments, the exposure time must also be short enough that the streaks fit into the field of view.) The maximum velocity V_M is given by $V_M = \frac{l}{\Delta t}$ where l is the length of the streak and Δt is the exposure time. For the standard pressure settings, V_M was found to be ~467μm/s. Because of the channel's extreme aspect ratio, the flow in the channel is well approximated by the solution for flow between parallel plates. In this case, the mean velocity (V_{avg}) is approximately 2/3 of the maximal velocity. This gives V_{avg} ~ 311 μm/s.

To measure an estimate of the cAMP profile across the observation channel, ~10 ppm fluorescein in KN2 buffer was used as a tracer dye. Micrographs where taken at four slightly overlapping fields of view spanning the observation channel (window) (in the x direction) using a 10X objective on a Carl Zeiss spinning disc confocal microscope. The focal plane used in these micrographs was established by loading cells into the chip and moving the focal position such that the cells were in focus for each field of view. The micrograph images were stitched together and analyzed using a homemade Matlab code. After taking micrographs at 10 second intervals over the course of multiple sweeps, the 2 buffer inlets were

clamped in order to flood the channel with fluorescein dye from the cAMP inlet. These micrographs of fluorescein dye completely flooding the channel were used to establish the fluorescence intensity corresponding to the dye at its original (maximal) concentration (I_M). Within the dataset, images where the dye was absent (between sweeps) were identified and used to calculate the background (I_B). The concentration of the diffusing dye in space and time was calculated by the equation

$$\frac{C(x,y,t)}{C_o} = \frac{I(x,y,t) - I_B(x,y)}{I_M(x,y) - I_B(x,y)} \tag{4-27}$$

where $I(x,y,t)$ is the intensity over the stitched field of view at a given time t and C_o is the original concentration of the fluorescein tracer dye. Because the field of view was limited to ~600 µm and the mean velocity was ~300 µm/s, the amount of change of profile within the entire field of view was limited. Therefore, it was safe to average the concentration data along the y-axis in order to reduce noise, arriving at the fractional concentration of the diffusing species as a function of time and x position ($f(x,t)$) as given by

$$f(x,t) = \int \frac{C(x,y,t)}{C_o} dy \tag{4-28}$$

where $f(x,t)$ represents the chemical concentration profile of the wave and varies from 0 to 1, where 1 represents the maximum concentration of the diffusing species (the concentration at the inlet). It was safe to assume that the profile of cAMP concentration in the chip was represented by $f(x,t)$

because cAMP and fluorescein have similar diffusion constants owing to their similar molecular weights. This data was used to produce kymographs representing the wave sweep process cf. Fig. 4-10.

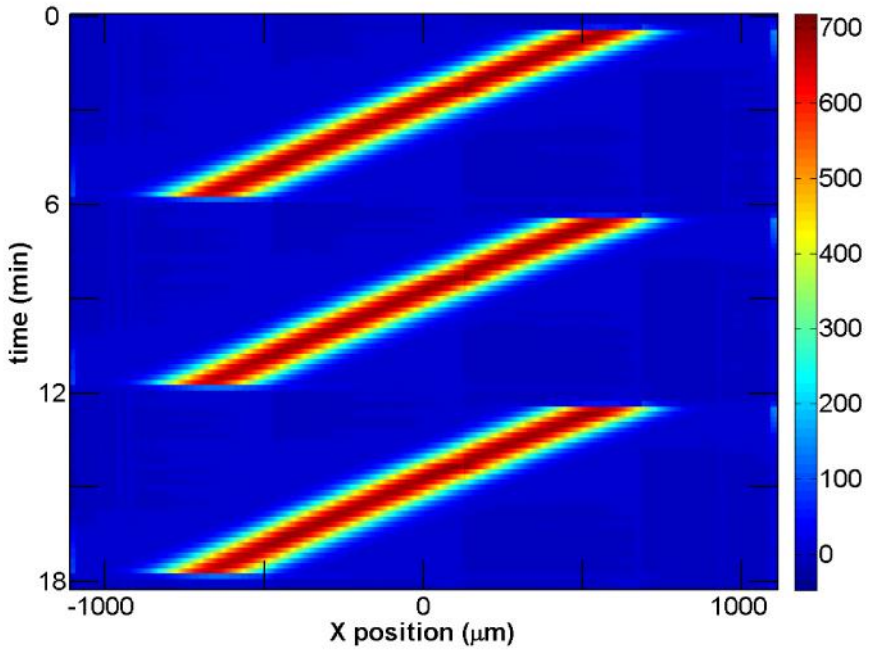

Figure 4-10: Kymograph for 3 wave sweeps with a 6 minute period (~320 seconds for the sweep and ~40 seconds for the resetting process) The color bar scale represents the concentration of cAMP predicted by the tracer dye intensity in units of nM where the concentration of the cAMP buffer flow at the inlet is 1000nM (as in the case of experiments on cells).

4.3: Cell Results and Conclusions

Ultimately, the system was used by experimentalist Monica Skoge to collect large amounts of data on cells chemotaxing in waves of cAMP concentration. Data was taken for a number of wave periods ranging from

6 to 20 minutes with the pressurization rates (and thus the wave sweep velocity) varied inversely to the pressure ramp-up period (t_{sweep}) (the delay for cAMP flow restoration is grouped into this value).

Cell movements were tracked and binned in time relative to the time at which the peak of the wave passed over them (as verified by tracer dye). For waves sweeping in the negative x-direction the cells are anticipated to chemotax in the positive x-direction. Chemotactic Index (*CI*) is a measure of chemotaxis given by dividing net displacement in the chemotactic direction (the x-direction) by the total distance traveled over a period of time. If the cells move purely in the positive x-direction, they will have a *CI* of 1. If the cells move purely in the negative x-direction, they will have a *CI* of -1. If the cells move at completer random, they will have a *CI* of 0. The chemotaxis data is shown in Fig. 4-11.

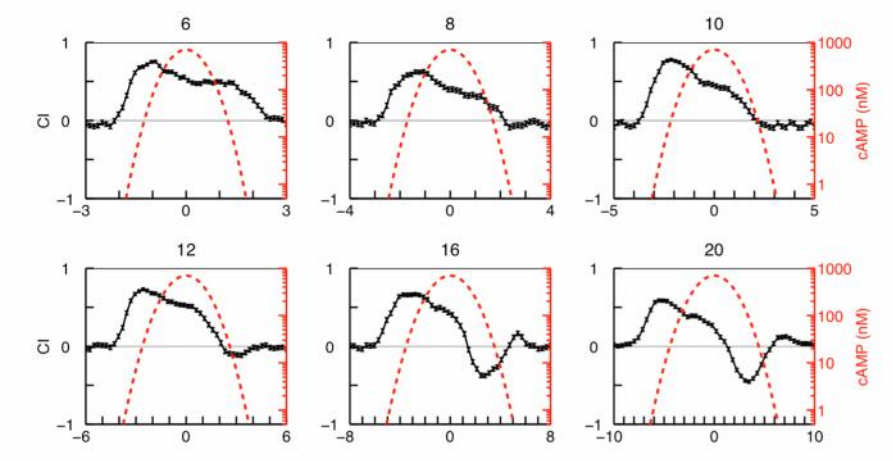

Figure 4-11: Chemotactic index versus time relative to the peak of the wave for various wave periods. The second axis shown in red is the concentration of the wave experienced by cells at the given time position relative to the peak of the wave.

The data shows that there are large amounts of cell reversal for wave periods longer than 12 minutes. This data lends new insights into the nature of eukaryotic chemotaxis and is discussed in further detail in the subsequently mentioned manuscript.

Chapter 4, in full, includes information and materials from the paper submitted for publication as “Cellular memory in eukaryotic chemotaxis”, Skoge, Monica; Yue, Haicen; Erickstad, Michael; Bae, Albert; Levine, Herbert; Groisman, Alex; Loomis, William F.; Rappel, Wouter-Jan. The dissertation author is a coauthor and a leading contributor to the microfluidics aspects of this paper.

REFERENCES

Chapter 1

1. G. M. Whitesides, *Nature*, 2006, **442**, 368-373.

2. C. Rivet, H. Lee, A. Hirsch, S. Hamilton and H. Lu, *Chemical Engineering Science*, 2011, **66**, 1490-1507.

3. C. D. Chin, T. Laksanasopin, Y. K. Cheung, D. Steinmiller, V. Linder, H. Parsa, J. Wang, H. Moore, R. Rouse and G. Umviligihozo, *Nature medicine*, 2011, **17**, 1015-1019.

4. H. Bruus, *Theoretical microfluidics*, Oxford University Press, 2008.

5. H. C. Berg, *Random walks in biology*, Princeton University Press, 1993.

6. M. A. Unger, H.-P. Chou, T. Thorsen, A. Scherer and S. R. Quake, *Science*, 2000, **288**, 113-116.

7. A. G. Emslie, F. T. Bonner and L. G. Peck, *Journal of Applied Physics*, 2004, **29**, 858-862.

8. B. Herman, *Fluorescence microscopy*, BIOS Scientific Publishers, 1998.

Chapter 2

1. P. Herman, B. P. Maliwal, H.-J. Lin and J. R. Lakowicz, Journal of Microscopy, 2001, 203, 176-181.

2. I. T. Young, Y. Garini, H. R. C. Dietrich, W. van Oel and G. L. Lung, LEDs for fluorescence microscopy, 2004.

3. H. R. Petty, Microscopy research and technique, 2007, 70, 687-709.

4. M. D. Huntington and T. W. Odom, Small, 2011, 7, 3144.

5. J. Kim, S. Paik, F. Herrault and M. G. Allen, presented in part at the Proc. Solid-State Sensors and Actuators Workshop, Hilton Head, June, 2012.

6. M. C. Breadmore and R. M. Guijt, Journal of Chromatography A, 2008, 1213, 3.

7. I. Moreno, M. Avendaño-Alejo and R. I. Tzonchev, Applied Optics, 2006, 45, 2265.

8. E. F. Reznikova, J. Mohr and H. Hein, Microsystem technologies, 2005, 11, 282-291.

Chapter 3

1. G. L. Semenza, *Current opinion in cell biology*, 2001, **13**, 167-171.

2. K. J. Banasiak and G. G. Haddad, *Brain research*, 1998, **797**, 295-304.

3. J. A. Dempsey, S. C. Veasey, B. J. Morgan and C. P. O'Donnell, *Physiological reviews*, 2010, **90**, 47-112.

4. A. Mohyeldin, T. Garzon-Muvdi and A. Quinones-Hinojosa, *Cell stem cell*, 2010, **7**, 150-161.

5. P. Carmeliet, Y. Dor, J.-M. Herbert, D. Fukumura, K. Brusselmans, M. Dewerchin, M. Neeman, F. Bono, R. Abramovitch and P. Maxwell, *Nature*, 1998, **394**, 485-490.

6. A. J. Peacock, *BMJ: British Medical Journal*, 1998, **317**, 1063.

7. D. L. Breitburg, D. W. Hondorp, L. A. Davias and R. J. Diaz, *Annual Review of Marine Science*, 2009, **1**, 329-349.

8. G. L. Semenza, *Hydroxylation of HIF-1: Oxygen Sensing at the Molecular Level*, 2004.

9. K. W. Freeman, B. E. Welm, R. D. Gangula, J. M. Rosen, M. Ittmann, N. M. Greenberg and D. M. Spencer, *Cancer research*, 2003, **63**, 8256-8263.

10. A. J. Chang and C. I. Bargmann, *Proceedings of the National Academy of Sciences*, 2008, **105**, 7321-7326.

11. K. Dooley and L. I. Zon, *Current opinion in genetics & development*, 2000, **10**, 252-256.

12. N. D. Lawson and B. M. Weinstein, *Nature Reviews Genetics*, 2002, **3**, 674-682.

13. G. J. Lieschke and P. D. Currie, *Nature Reviews Genetics*, 2007, **8**, 353-367.

14. O. Pourquie, *Science*, 2003, **301**, 328-330.

15. D. Y. R. Stainier, *Nature Reviews Genetics*, 2001, **2**, 39-48.

16. R. J. Egan, C. L. Bergner, P. C. Hart, J. M. Cachat, P. R. Canavello, M. F. Elegante, S. I. Elkhayat, B. K. Bartels, A. K. Tien and D. H. Tien, *Behavioural brain research*, 2009, **205**, 38-44.

17. R. W. Friedrich, G. A. Jacobson and P. Zhu, *Current Biology*, 2010, **20**, R371-R381.

18. R. Spence, G. Gerlach, C. Lawrence and C. Smith, *Biological Reviews*, 2008, **83**, 13-34.

19. R. Kopp, I. Bauer, A. Ramalingam, M. Egg and T. Schwerte, *PloS one*, 2014, **9**, e89099.

20. B. A. Mendelsohn, B. L. Kassebaum and J. D. Gitlin, *Developmental Dynamics*, 2008, **237**, 1780-1788.

21. P. A. Padilla and M. B. Roth, *Proceedings of the National Academy of Sciences*, 2001, **98**, 7331-7335.

22. M. G. Jonz and C. A. Nurse, *Journal of Experimental Biology*, 2005, **208**, 1537-1549.

23. D. V. Almeida, A. Bianchini and L. F. Marins, *General and comparative endocrinology*, 2013, **194**, 102-109.

24. X. Yu and Y. V. Li, *International journal of physiology, pathophysiology and pharmacology*, 2012, **3**, 88.

25. A. Funfak, A. Brosing, M. Brand and J. M. Kohler, *Lab on a Chip*, 2007, **7**, 1132-1138.

26. E. M. Wielhouwer, S. Ali, A. Al-Afandi, M. T. Blom, M. B. O. Riekerink, C. Poelma, J. Westerweel, J. Oonk, E. X. Vrouwe and W. Buesink, *Lab on a Chip*, 2011, **11**, 1815-1824.

27. D. Choudhury, D. van Noort, C. Iliescu, B. Zheng, K.-L. Poon, S. Korzh, V. Korzh and H. Yu, *Lab on a Chip*, 2012, **12**, 892-900.

28. J. Akagi, K. Khoshmanesh, B. Evans, C. J. Hall, K. E. Crosier, J. M. Cooper, P. S. Crosier and D. Wlodkowic, *PloS one*, 2012, **7**, e36630.

29. F. Yang, Z. Chen, J. Pan, X. Li, J. Feng and H. Yang, *Biomicrofluidics*, 2011, **5**, 024115.

30. C. Zheng, H. Zhou, X. Liu, Y. Pang, B. Zhang and Y. Huang, *Chemical Communications*, 2014, **50**, 981-984.

31. S.-H. Huang, K.-S. Huang, C.-H. Yu and H.-Y. Gong, *Biomicrofluidics*, 2013, **7**, 064107.

32. L. L. Bischel, B. R. Mader, J. M. Green, A. Huttenlocher and D. J. Beebe, *Lab on a Chip*, 2013, **13**, 1732-1736.

33. J. W. Allen and S. N. Bhatia, *Biotechnology and bioengineering*, 2003, **82**, 253-262.

34. A. P. Vollmer, R. F. Probstein, R. Gilbert and T. Thorsen, *Lab on a Chip*, 2005, **5**, 1059-1066.

35. M. Polinkovsky, E. Gutierrez, A. Levchenko and A. Groisman, *Lab on a Chip*, 2009, **9**, 1073-1084.

36. M. Adler, M. Polinkovsky, E. Gutierrez and A. Groisman, *Lab on a Chip*, 2010, **10**, 388-391.

37. J. M. Gray, D. S. Karow, H. Lu, A. J. Chang, J. S. Chang, R. E. Ellis, M. A. Marletta and C. I. Bargmann, *Nature*, 2004, **430**, 317-322.

38. R. H. W. Lam, M.-C. Kim and T. Thorsen, *Analytical chemistry*, 2009, **81**, 5918-5924.

39. J. F. Lo, E. Sinkala and D. T. Eddington, *Lab on a Chip*, 2010, **10**, 2394-2401.

40. M. Zimmer, J. M. Gray, N. Pokala, A. J. Chang, D. S. Karow, M. A. Marletta, M. L. Hudson, D. B. Morton, N. Chronis and C. I. Bargmann, *Neuron*, 2009, **61**, 865-879.

41. E. A. Lemke, Y. Gambin, V. Vandelinder, E. M. Brustad, H.-W. Liu, P. G. Schultz, A. Groisman and A. A. Deniz, *Journal of the American Chemical Society*, 2009, **131**, 13610-13612.

42. O. S. Wolfbeis, L. J. Weis, M. J. P. Leiner and W. E. Ziegler, *Analytical chemistry*, 1988, **60**, 2028-2030.

Chapter 4

1. A. J. Ridley, M. A. Schwartz, K. Burridge, R. A. Firtel, M. H. Ginsberg, G. Borisy, J. T. Parsons and A. R. Horwitz, *Science*, 2003, **302**, 1704-1709.

2. D. Dormann and C. J. Weijer, *Current opinion in genetics & development*, 2003, **13**, 358-364.

3. M. Tessier-Lavigne and C. S. Goodman, *Science*, 1996, **274**, 1123-1133.

4. M. Baggiolini, *Nature*, 1998, **392**, 565-568.

5. E. T. Roussos, J. S. Condeelis and A. Patsialou, *Nature Reviews Cancer*, 2011, **11**, 573-587.

6. P. N. Devreotes and S. H. Zigmond, *Annual review of cell biology*, 1988, **4**, 649-686.

7. T. Jin, X. Xu and D. Hereld, *Cytokine*, 2008, **44**, 1-8.

8. P. J. M. Van Haastert and P. N. Devreotes, *Nature reviews Molecular cell biology*, 2004, **5**, 626-634.

9. K. F. Swaney, C.-H. Huang and P. N. Devreotes, *Annual review of biophysics*, 2010, **39**, 265-289.

10. T. Lammermann, P. V. Afonso, B. R. Angermann, J. M. Wang, W. Kastenmuller, C. A. Parent and R. N. Germain, *Nature*, 2013.

11. P. Niethammer, C. Grabher, A. T. Look and T. J. Mitchison, *Nature*, 2009, **459**, 996-999.

12. W. Loomis, *The development of Dictyostelium discoideum*, Elsevier, 2012.

13. R. E. Goldstein, *Physical review letters*, 1996, **77**, 775.

14. P. N. Devreotes, M. J. Potel and S. A. MacKay, *Developmental Biology*, 1983, **96**, 405.

15. M. Postma and P. J. M. van Haastert, in *Chemotaxis*, Springer, 2009, pp. 473-488.

16. Y. Kim, K. Pekkan, W. C. Messner and P. R. LeDuc, *Journal of the American Chemical Society*, 2010, **132**, 1339-1347.